(200)
R290
no.80-1229

(200)
R290
no.80-1229

U.S. Geological Survey
[Reports-Open file Series]

UNITED STATES DEPARTMENT OF THE INTERIOR
GEOLOGICAL SURVEY

USGS LIBRARY-RESTON
3 1818 00074267 4

Long-term Highwall Stability in the Northwestern Powder River Basin, Wyoming and Montana

by

William K. Smith

U.S. GEOLOGICAL SURVEY
RESTON, VA.
DEC 02 1980
LIBRARY

Open-File Report 80-1229

1980

This report is preliminary and has not been reviewed for conformity with U.S. Geological Geological Survey editorial standards and stratigraphic nomenclature. Any use of trade names is for descriptive purposes only and does not imply endorsement by the U.S. Geological Survey.

315655

ACKNOWLEDGMENTS

Completion of this study would have been impossible without the cooperation of many persons and organizations. I would like to thank Peter Kiewit Sons' Company and their subsidiaries, Decker Coal Company and Big Horn Coal Company, for access to their properties and information provided in the early stages of this study, and Padlock Ranch, Inc., Dayton, Wyoming, for access to the Hidden Water mine. I also thank Bruce Ringen, U.S. Geological Survey, Cheyenne, Wyoming, for bringing the slide at the Hidden Water mine to my attention.

I would also like to thank John F. Abel, Jr., of the Colorado School of Mines for his helpful suggestions and William Z. Savage of the Geological Survey for helping with the finite element analysis and teaching me the basics of tensor analysis. This report has been submitted as a dissertation in partial fulfillment of the requirements for the degree of Doctor of Philosophy to the Department of Mining and Geological Engineering of the University of Arizona. I thank my advisor, Dr. C. E. Glass, and the other members of my committee, Drs. J. K. Daemen and W. C. Peters, for their advice, suggestions, encouragement, and unending patience.

TABLE OF CONTENTS

	Page
LIST OF ILLUSTRATIONS	vi
LIST OF TABLES	ix
ABSTRACT	x
INTRODUCTION	1
Statement of the Problem	1
Description of Field Study Site	2
Units, Terminology, Symbols, and Conventions	5
REGIONAL SETTING AND GEOLOGY	8
Physiography and Topography	8
Stratigraphy	9
Structural and Historical Geology	10
Fracture Patterns	13
Stress History of the Fort Union and Wasatch Formations	18
PHYSICAL PROPERTIES	22
Analysis of Triaxial Tests	22
Methods	22
Results	24
Effect of Confining Pressure on Young's Modulus	31
STABILITY ANALYSIS	35
Limiting Equilibrium	35
Finite Element Analysis	36
Convergence of Solutions	39
Rheology and Yield Criteria	40
Factor of Safety	44
HIDDEN WATER MINE SLIDE	48
Aerial Photographic Interpretation of Slide Area	48
Slide Monitoring	48
Stability Analysis of the Hidden Water Mine Slide	56
Spencer Analysis	59

TABLE OF CONTENTS--Continued

Page

Finite Element Analysis 62
Suitability of Analytical Methods 82

TIME-DEPENDENT BEHAVIOR 84

Previous Work 85
Extension of the Nelson-Thompson Hypothesis 87
Relationship Between Residual Factor and Time to Failure . . 90

CONCLUSIONS AND RECOMMENDATIONS FOR FURTHER RESEARCH 93

APPENDIX 96

Derivation of the Factor of Safety for the Drucker-Prager Yield Criterion 96
Derivation of the Residual Factor for the Drucker-Prager Yield Criterion 101
Derivation of the Residual Factor in Terms of the Factors of Safety 102

REFERENCES 103

LIST OF ILLUSTRATIONS

Page

Figure

1. Index map showing study area in the Powder River Basin and adjacent physiographic features 3

2. Photograph of the landslide at Hidden Water mine 4

3. Generalized cross section of the Powder River Basin 12

4. Schmidt diagram for all joints (less bedding plane fractures) observed in the northwestern Powder River Basin 14

5. Schmidt diagram for joints in outcrops (less bedding plane fractures), northwestern Powder River Basin 15

6. Schmidt diagram for joints in coal and overburden (less bedding plane fractures), Decker mine, Montana 16

7. Schmidt diagram for joints in coal and overburden (less bedding plane fractures), Decker, Big Horn, Welch, and abandoned mines 17

8. Hypothetical sequence of loading and deformational history in the western Powder River Basin 21

9. Results of triaxial tests on shale #1, Decker mine, Montana 26

10. Results of triaxial tests on shale #3A, Decker mine, Montana 27

11. Results of triaxial tests on siltstone #3B, Decker mine, Montana 28

12. Results of triaxial tests on limey siltstone #3D, Decker mine, Montana 29

13. Results of triaxial tests on coal #4 and #4A, Decker mine, Montana 30

LIST OF ILLUSTRATIONS--Continued

Page

Figure

14. Young's modulus as a function of confining pressure for triaxial tests 32

15. Idealized stress-strain curve for an elastic-plastic material 41

16. Graph for determining the Drucker-Prager material constants α and k from triaxial tests 43

17. Drucker-Prager yield criterion in principal stress space 45

18. Air photograph of Hidden Water mine taken in 1954 49

19. Air photograph of Hidden Water mine taken in 1967 50

20. Air photograph of Hidden Water mine taken in 1974 51

21. Air photograph of Hidden Water mine taken in 1975 52

22. Map of part of Hidden Water mine showing layout of survey net 54

23. Cross section through Hidden Water mine landslide 57

24. Idealized slope at Hidden Water mine used for Spencer stability analysis 60

25. Finite element grid used in stability analysis of Hidden Water mine landslide, showing boundary conditions 63

26. Results of linear elastic finite element analysis of Hidden Water mine landslide, peak strengths 65

27. Results of elastic-plastic finite element analysis of Hidden Water mine landslide, peak strengths 66

28. Results of linear elastic finite element analysis of Hidden Water mine landslide, residual strengths 67

29. Results of elastic-plastic finite element analysis of Hidden Water mine landslide, residual strengths 68

LIST OF ILLUSTRATIONS--Continued

Page

Figure

30. Principal stress trajectories, elastic 70

31. Principal stress trajectories, elastic-plastic analysis, peak strengths 71

32. Principal stress trajectories, elastic-plastic analysis, residual strengths 72

33. Expected shear failure trajectories, elastic analysis . . . 73

34. Expected shear failure trajectories, elastic-plastic analysis, peak strengths 74

35. Expected shear failure trajectories, elastic-plastic analysis, residual strengths 75

36. Contours of minimum principal stress, elastic analysis . . 76

37. Contours of minimum principal stress, elastic-plastic analysis, peak strengths 77

38. Contours of minimum principal stress, elastic-plastic analysis, residual strengths 78

39. Contours of $\sqrt{J_2}$, elastic analysis 79

40. Contours of $\sqrt{J_2}$, elastic-plastic analysis, peak strengths 80

41. Contours of $\sqrt{J_2}$, elastic-plastic analysis, residual strengths 81

42. Idealized Mohr diagram illustrating the Nelson-Thompson hypothesis and Skempton's residual factor (R) 88

43. Nelson-Thompson hypothesis and Skempton's residual factor using the Drucker-Prager yield criterion 89

44. Relationship between residual factor and time to failure for excavations in overconsolidated clays 91

45. Transformation of axes for derivation of safety factor using Drucker-Prager criterion 97

LIST OF TABLES

Table		Page
1.	Symbols, abbreviations, and conversion factors	6
2.	Generalized stratigraphic column for the northwestern Powder River Basin	11
3.	Physical-property test results for samples from Decker mine, Montana	25
4.	Results of triangulation surveys	55
5.	Material properties used for stability analyses of Hidden Water mine landslide	58
6.	Results of Spencer stability analyses for Hidden Water mine landslide	61
7.	Results of finite element analyses for Hidden Water mine landslide	61

ABSTRACT

Time-dependent behavior of natural and excavated slopes in sedimentary rocks is a subject that is poorly understood at present but that is now an important consideration in the design, operation, and reclamation of energy-extraction facilities, in part because of the environmental considerations mandated by the Surface Mining Control and Reclamation Act of 1977 (Public Law 95-87).

A slide in an abandoned, unreclaimed strip mine northwest of Sheridan, Wyoming, has been analyzed as an example of a long-term slope failure in the region. This slide occurred in early 1975, some 20 years after cessation of mining. This investigation used Spencer's limiting equilibrium method and an elastic-plastic finite element method incorporating the Drucker-Prager yield criterion.

This slide was found to fit the model for time-dependent failure proposed by Nelson and Thompson (1977) in which the time to failure is related to Skempton's residual factor. The Nelson-Thompson hypothesis is extended for use with the three-dimensional Drucker-Prager yield criterion. The residual factor (R) may be computed from the factors of safety with respect to peak (F_p) and residual (F_r) material properties, using either the Mohr-Coulomb or Drucker-Prager criterion, by the relationship

$$R = \frac{F_p - 1}{F_p - F_r} .$$

At the present time, the Spencer limiting equilibrium analysis is a more usable tool for ordinary slope design than the elastic-plastic finite element analysis because of the speed, simplicity, and ease of including the effects of ground water in the Spencer analysis.

INTRODUCTION

Statement of the Problem

The Powder River Basin of Wyoming and Montana contains a sizeable percentage of the known strippable coal reserves in the United States. Development of this resource is proceeding at a rapid pace in order to help meet the nation's energy requirements; however, environmental considerations require careful planning and design of reclamation schemes in order to assure continued protection of the land over the long term. Unfortunately, little is known about the long-term behavior of disturbed coal-bearing units in this region. The Surface Mining Control and Reclamation Act of 1977 (Public Law 95-87) was signed by President Jimmy Carter on August 3, 1977. Compliance with this law requires a better understanding of the long-term behavior of disturbed materials. Section 515 of the Act sets performance standards for environmental protection and makes numerous references to stability or stabilization of highwalls and regraded spoil areas. Section 715.14 of the proposed rules implementing the Act (Federal Register, September 7, 1977, p. 44920-44957) makes reference to "long-term stability" of regraded areas and specifies a minimum static safety factor of 1.5 for plateau outslopes in mountaintop removal operations. Section 715.4, pertaining to certain "special bituminous coal mines" in Wyoming, allows for leaving highwalls around one-half of water impoundments if "it can be demonstrated by the permittee that the pitwall can be stabilized by

terracing or other techniques." Thus a more detailed knowledge of long-term slope behavior is required by both the mine designer and the regulatory agency to assure adequate protection of the environment.

Description of Field Study Site

A landslide that illustrates the problem of long-term highwall behavior is located in an abandoned strip mine near the head of Hidden Water Creek in the NE 1/4 sec. 1, T. 57 N., R. 85 W., in Sheridan County, Wyoming, about 18 km northwest of Sheridan and 9 km northeast of Ranchester (Fig. 1). The mine is one of three in the immediate vicinity that were operated by the Big Horn Coal Company. To avoid confusion with the present Big Horn mine near Acme, Wyoming, a few kilometers to the east, and since the pit floor is the course of Hidden Water Creek, the site will be referred to in this report as the Hidden Water mine. The area was mined from 1946 until 1955, and no attempt was made to reclaim the area. The final highwall was left with a spoil pile sitting on top of it, as shown in Figure 2. Surprisingly, it remained in a relatively stable condition for about 20 years, except for some erosion and minor gullying resulting from slope wash on the steep face of the spoil pile and highwall.

Sometime between October 1, 1974, and June 10, 1975, as evidenced by aerial photographs, a section of the highwall and overlying spoil pile failed. the slide is cusp-shaped, as is typical of failure in many soil materials. the failed zone is about 60 m wide at the crest, and the horizontal distance from the toe of the slide mass to the crest is about 80 m. An overall view of the slide is shown in Figure 2.

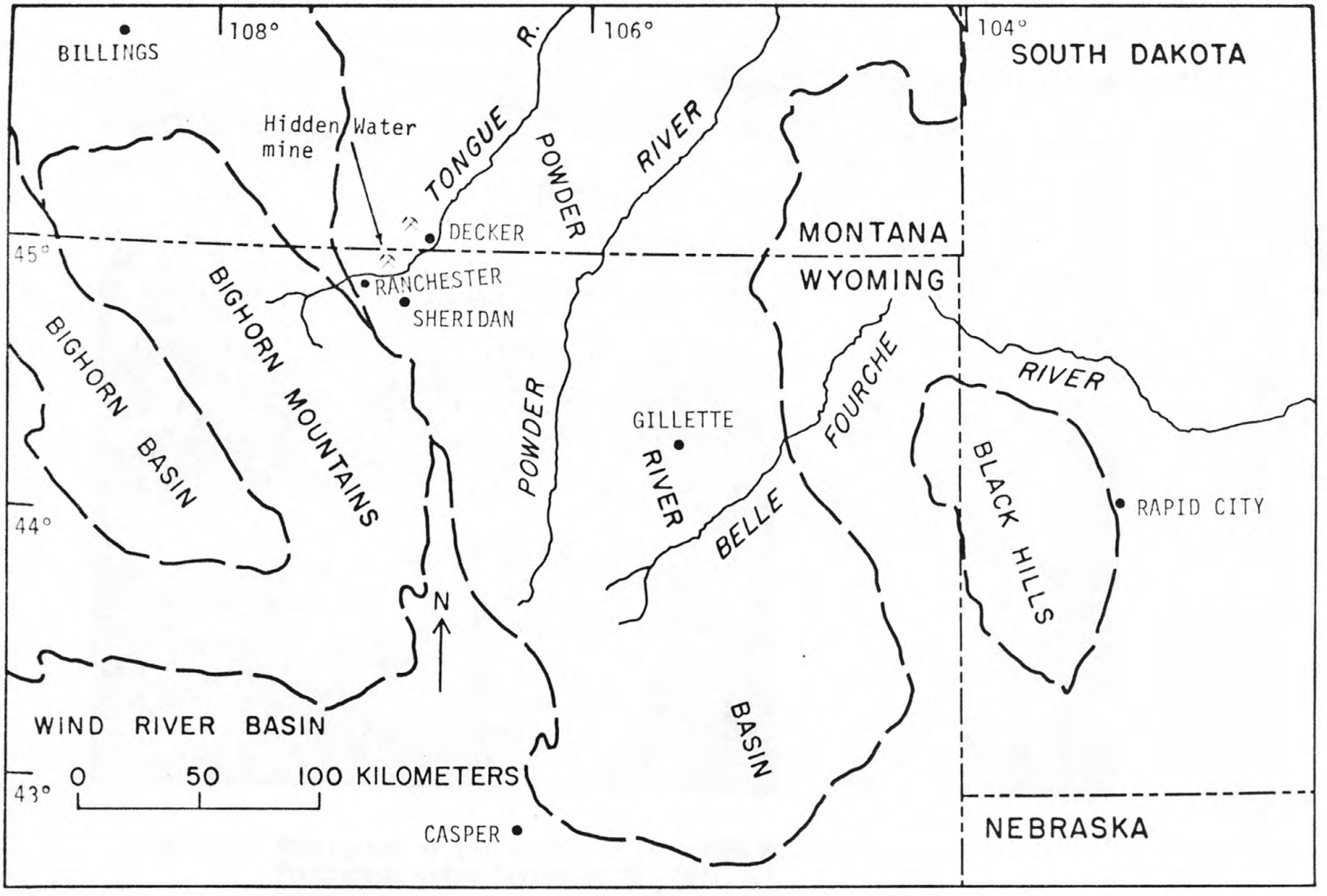

Figure 1. Index map showing study area in the Powder River Basin and adjacent physiographic features.

Figure 2. Photograph of the landslide at Hidden Water mine. Photograph taken September 22, 1977.

The fact that the failure involves the highwall itself, rather than just the spoil pile, is shown by field evidence. The apparent volume of the slide material is greater than that of the void in the spoil pile. Small sections of the slide scarp, where exposed near the top of the highwall, cut back into the highwall. Blocks of coal are abundant in the slide material near the toe; bedding plane fractures in some of these blocks dip back into the slide. An upward vertical component of movement near the toe following a heavy rain in May 1978, while not convincing by itself, lends further support to the idea that the failure involves the base of the slope as well as the highwall.

Fieldwork, including ground surveys, was conducted in 1977 and 1978. Stability analyses were made using both finite element and limit equilibrium methods. Details of these studies will be presented later in this study.

Units, Terminology, Symbols, and Conventions

SI (metric) measurements are used throughout this study with the exception of angular measurements. A list of units, abbreviations, and conversion factors is given in Table 1. The basic unit for pressure or stress in SI is the pascal, and values in this report are given in terms of kilopascals (kPa) or megapascals (MPa) rather than in kilograms per square centimeter. Symbols commonly used in equations in this report are listed and defined in Table 1. Other symbols are defined where used.

Table 1. Symbols, abbreviations, and conversion factors

Symbol	Definition
c	Cohesion
E	Young's modulus
F	Factor of safety
I_1	First invariant of stress
J_2	Second invariant of stress deviation
k	Plasticity constant
n	Strain-hardening parameter
R	Residual factor
s_{ij}	Stress deviation tensor
α	Plasticity constant
δ_{ij}	Kronecker delta
ε	Strain component
ν	Poisson's ratio
σ	Stress component
τ	Shear stress
ϕ	Angle of internal friction
m	meter = 3.281 ft
Pa	Pascal = 1 newton/m^2
km	kilometer = 0.6214 mile
kPa	1000 Pa = 0.1451 lb/$in.^2$
MPa	10^6 Pa = 145.1 lb/$in.^2$
GPa	10^9 Pa = 1.45×10^5 lb/$in.^2$
kg/m^3	kilogram per cubic meter = 0.06243 lb/ft^3
NTIS	National Technical Information Service 5285 Port Royal Road Springfield, VA 22161

Double subscripts are tensor notation; single subscripts are conventional engineering notation.

The terms "consolidation" and "consolidated" have very different meanings to a geologist and to a soils engineer. This can be very confusing in a report such as this where one might speak of "overconsolidated rocks which are poorly consolidated." In this study "consolidated" will be used in the soil mechanics sense; "indurated" will be used for the geologic equivalent.

The convention used here for stresses is that tensile stresses are positive, compressive stresses negative. This is contrary to the usual usage in soil and rock mechanics, but agrees with that used in other fields of engineering and theoretical mechanics.

REGIONAL SETTING AND GEOLOGY

Physiography and Topography

The Powder River Basin is a broad topographic and structural basin on the western edge of the Great Plains physiographic province and in the southwest corner of the Missouri Plateau section (Keefer, 1974, pl. A-1; Fenneman, 1931). The basin is elliptical in plan, elongated in the north-northwest direction, and approximately 400 km long and 175 to 200 km wide. It is bounded on the east by the Black Hills, on the west by the Bighorn Mountains of the Middle Rocky Mountains province, and on the south by the Laramie Mountains of the Southern Rocky Mountains province (Fig. 1). On the southwest it is separated from the Wind River Basin of the Wyoming Basin province by the Casper Arch. To the north the Powder River Basin becomes indistinguishable from the rest of the Missouri Plateau in an area near the Yellowstone River in Montana.

The northern two-thirds of the basin consists generally of open high hills (20-50 percent of the area sloping less than 8 percent and local relief of 150 to 300 m), whereas the southern third is mainly plains and tablelands with moderate relief (90-150 m) (Keefer, 1974, pl. A-2). Elevations in the northwest part of the basin (the area of this study) range from about 1,000 m in the Tongue River valley to about 1,310 m on the northwest side of the Tongue River near the Montana-Wyoming border.

Most of the major streams are well entrenched and flow generally northeastward, whereas the secondary drainages have a northwest-southeast orientation and impart a definite grain to the topography. These directions correspond to the two regional joint sets. The mesas and plateaus are moderately to well dissected; the higher areas are more dissected than the lower areas.

Vegetation consists mainly of various grasses with some sagebrush on the plains, which provides forage for cattle and other stock as well as for the abundant pronghorn antelope, and cover for the rattlesnakes. At higher elevations and on steeper slopes, sparse pine woodland is mixed with the range grasses.

Stratigraphy

Rocks exposed in the Powder River Basin range in age from Cambrian to Eocene, with one small exposure of Oligocene rocks near the center of the basin (McKenna and Love, 1972, p. 6; Keefer, 1974, pl. A-3). Pre-Tertiary rocks, however, crop out only in a very narrow band along the Bighorn Mountain front on the west and in a slightly wider band at the base of the Black Hills on the east. Most of the basin is covered by the Fort Union Formation of Paleocene age and the overlying Wasatch Formation of Eocene age. All of the coal currently mined in the region is from the Fort Union and Wasatch Formations, but coal beds are also known to occur in the Mesaverde (Parkman Sandstone Member) and Lance Formations (Upper Cretaceous). Precambrian igneous and metamorphic rocks are exposed in the central parts of the Bighorn

Mountains and the Black Hills. A generalized regional stratigraphic column is shown in Table 2.

The Precambrian basement rocks are overlain by approximately 5000 m of sedimentary rocks of Paleozoic, Mesozoic, and early Tertiary age. Paleozoic rocks still cover most of the northern part of the Bighorn Mountains, and the Mississippian Madison Limestone presents dramatic exposures as the dip slopes form the eastern flanks of the range. Mesozoic rocks are exposed near the base of the mountains where the edges have been upturned. Relatively flat lying basin-fill deposits of the Fort Union and Wasatch Formations were deposited during, and following, uplift of the Bighorn Mountains and Black Hills in Laramide time.

Structural and Historical Geology

The Powder River Basin is a broad asymmetrical basin whose axis trends north-northwest. The regional eastward dip is much steeper on the west side (50 m/km) than the westward dip on the east side (20 m/km); consequently, the axis runs very near the western margin of the basin. Total structural relief on the Precambrian basement rocks from the crest of the Bighorn Uplift to the deepest part of the basin is of the order of 8,000 m (Rocky Mountain Association of Geologists, 1972, p. 53; Ebaugh, 1977, p. 13). A regional cross section is shown in Figure 3.

Table 2. Generalized stratigraphic column for the northwestern Powder River Basin (from U. S. Geol. Survey and Montana Dept. State Lands, 1977, p.118-120)

Age		Unit	Approximate Thickness(m)	Description
QUATERNARY	Holocene	Alluvium	25	Nonindurated poorly stratified clay, sand, and gravel deposited in stream valleys
QUATERNARY	Pleistocene	Terrace deposits	6	Gravel beds 0.3-2 m thick consisting primarily of sand, chert, quartzite, limestone, granite, dolomite, diabase and metamorphic pebbles and cobbles as much as 30 cm thick. Commonly cap small terraces near the Tongue River
TERTIARY	Eocene	Wasatch Formation	120	Interbedded soft clay, shale siltstone, and sandstone, several thin coal beds, and numerous thin beds of molluscan fossils. Locally contains thick beds of clinker (baked or fused sandstone or shale)
TERTIARY	Paleocene	Fort Union Formation Tongue River Member	490	Interbedded sandstone, siltstone, and shale, numerous thick and thin coal beds, sever thin beds of molluscan fossils, and several zones of abundant silicified wood. Locally contains thick beds of clinker (baked or fused sandstone or shale)
		Lebo Shale Member	380	Dark gray mudstone and claystone, contains abundant ferruginous concretions and a few lenticular beds of light-gray sandstone. Locally contains one or more coal beds
		Tullock Member	170	Light-gray calcareous sandstone, gray sandy and silty shale, and a few thin beds of coal and coaly shale
CRETACEOUS	Upper Cretaceous	Hell Creek or Lance Formation	200	Gray and greenish-gray shale, and light-gray, fine-grained sandstone with traces of coal and coaly shale.
		Fox Hills Sandstone	60	Light to very light gray sandstone and gray to grayish green shale and sandy shale
		Bearpaw Shale	80	Gray to dark-gray bentonitic shale and sandy shale, a few thin beds of light-gray bentonite, and dark-gray argillaceous sandstone
		Parkman Sandstone	190	Light-gray, fine-to-coarse-grained sandstone, gray to dark-gray shale, minor beds of carbonaceous shale, and traces of coal
		Cody Shale	855	Gray, dark-gray, and gray-green shale, minor gray fine-grained glauconitic sandstone, and thin beds of bentonite. Contains the Shannon Sandstone in the upper part, and Niobrarra, Carlisle, and Belle Fourche Shales in lower part
	Lower Cretaceous	Mowry shale	120	Dark-gray siliceous shale containing thin beds of bentonite and thin beds of dark-gray or gray-green argillaceous sandstone and siltstone
		Newcastle Sandstone	15	Gray to gray-brown fine-grained argillaceous sandstone interbedded with a few beds of dark-gray shale. Also called Muddy Sandstone
		Skull Creek Shale	27	Dark-gray shale, bentonitic in part
		Fall River Formation	60	Gray bentonitic shale, gray to dark-gray argillaceous siltstone and very fine-grained sandstone
		Lakota Formation	55	Light-gray, gray-green, and reddish-brown claystone, containing beds of light-gray fine- to coarse-grained sandstone in lower half
JURASSIC		Morrison Formation	45	Maroon, green, and gray claystone, calcareous in part, containing beds of light gray very-fine-grained calcareous sandstone, or sandy limestone, in lower part
JURASSIC		Sundance Formation	65	Gray to gray-green shale, sandy in part, interbedded with light-gray glauconitic calcareous sandstone
JURASSIC		Piper Limestone	12	Brown to dark-brown limestone, oolitic in part
JURASSIC		Underlying Jurassic rocks	70	Green and reddish claystone in upper part, beds of tan dolomite and limestone in middle and orange-red shale interbedded with gypsum and anhydrite in lower part
TRIASSIC		Chugwater Formation	105	Orange red very-fine-grained sandstone, dolomitic in part, interbedded with reddish-brown or orange-red shale and siltstone
PERMIAN		Goose Egg Formation	50	Orange-red sandy shale and very-fine-grained sandstone and pink to white gypsum and anhydrite
PENNSYLVANIAN		Tensleep Sandstone	60	Very-light-gray to pink fine-grained sandstone, dolomitic in part, light-gray to purple dolomite and sandy dolomite, with minor maroon shale
PENNSYLVANIAN		Amsden Formation	37	Light-gray to pink cherty dolomite and reddish limestone in upper 25 m; orange-red fine- to coarse-grained gypsiferous sandstone in lower 13 m
MISSISSIPPIAN		Madison Limestone	245	Light gray and brownish bioclastic dolomite and minor limestone, contains one bed of anhydrite
DEVONIAN		Duperow Formation	21	Light-gray, tan, and pinkish dolomite, and a few thin beds of siltstone and shale
SILURIAN		Interlake Formation	12	Light-gray to tan fragmented dolomite
ORDOVICIAN		Bighorn Dolomite	130	Light-gray to tan sucrose dolomite
ORDOVICIAN		Winnipeg Sandstone	18	Light gray very-fine- to coarse-grained quartzite sandstone
CAMBRIAN		Cambrian rocks undivided	9	Limestone and shale
		Precambrian rocks		

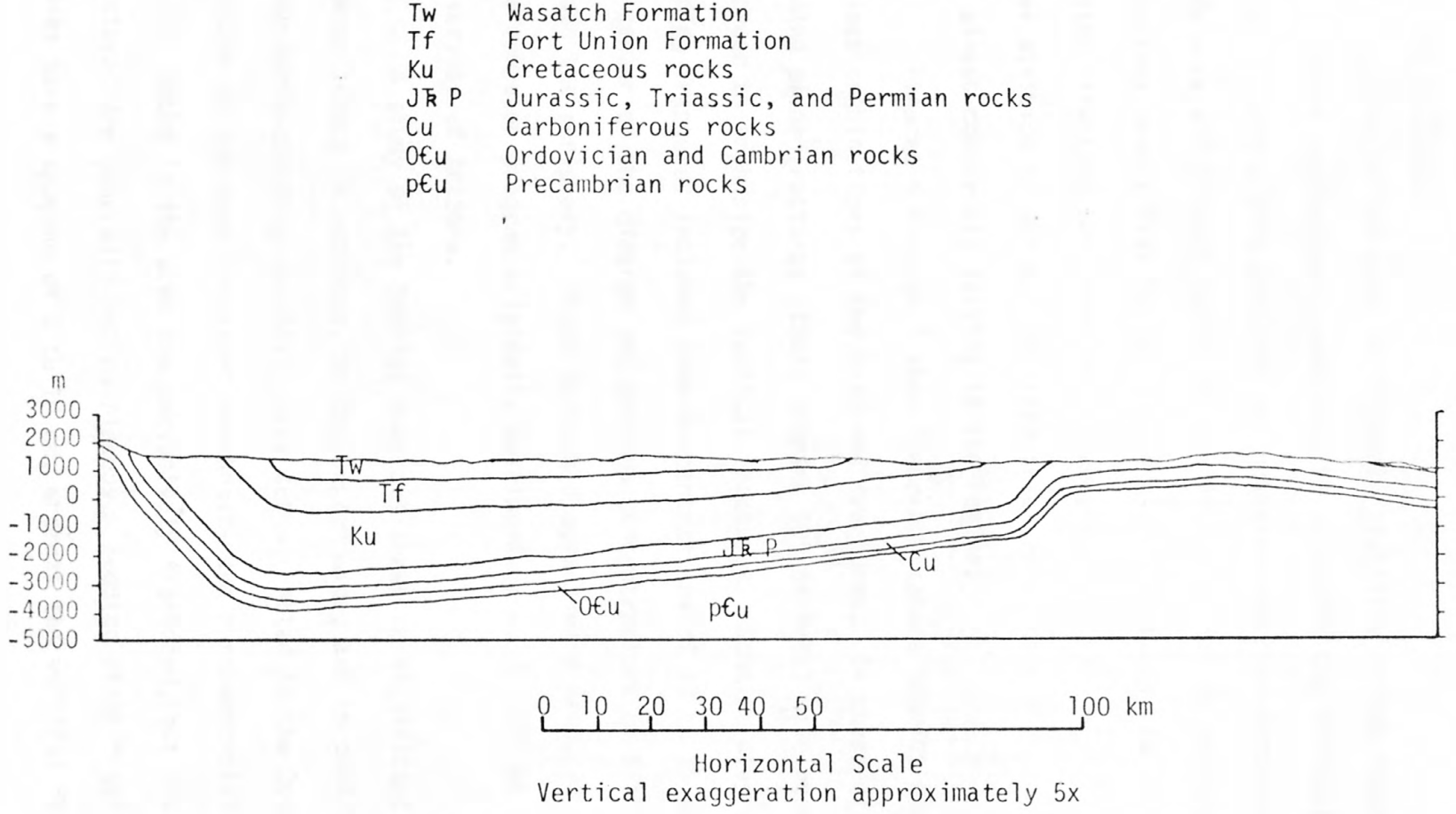

Figure 3. Generalized cross section of the Powder River Basin (modified from Beikman, 1962, Fig. 2).

Fracture Patterns

Early in the study of highwall stability in the Powder River Basin, field measurements were made to determine the regional fracture pattern. Joints were measured at scattered outcrops throughout the study area and in more detail at the Decker mine. In addition to the ubiquitous nearly flat lying bedding plane fractures, two nearly vertical fracture sets were recognized, one striking N. 37° E. and the other striking N. 45° W. Inclined fractures (those dipping 10° and 80°) are almost completely lacking in the region.

Figures 4 through 7 show lower-hemisphere Schmidt diagrams for various combinations of the observed fractures. In these diagrams the bedding plane fractures (those dipping 10° or less) have been eliminated in order to emphasize the vertical fractures. Schmidt diagrams with bedding fractures included show concentrations of 10 to 15 percent at the center of the diagram and maximum concentrations of 5 to 7 percent around the periphery. These Schmidt diagrams were produced with the aid of a computer program originally developed by R. D. Call at The University of Arizona.

A study of the Schmidt diagrams shows no significant differences between joints in outcrops, in the Decker mine, and in coal beds. A minor north-striking vertical joint set was noted in the Decker mine in addition to the more prominent northeast- and northwest-striking sets.

Rocks in the area are pervasively fractured, but individual fractures are generally not continuous. Bedding plane fractures in the shales have a spacing of 2 to 10 cm, whereas the vertical fractures have

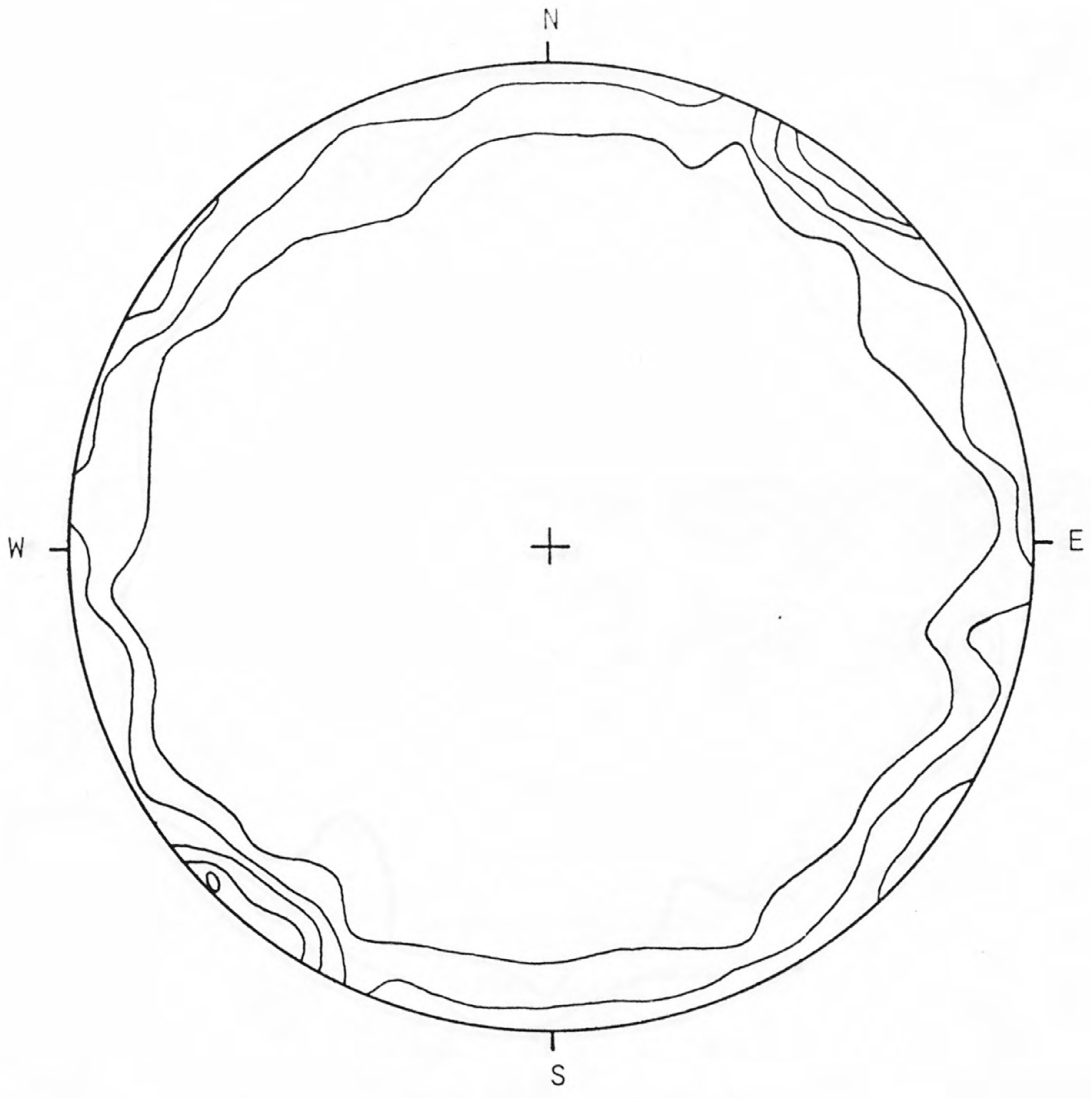

Figure 4. Schmidt diagram for all joints (less bedding plane fractures) observed in the northwestern Powder River Basin.

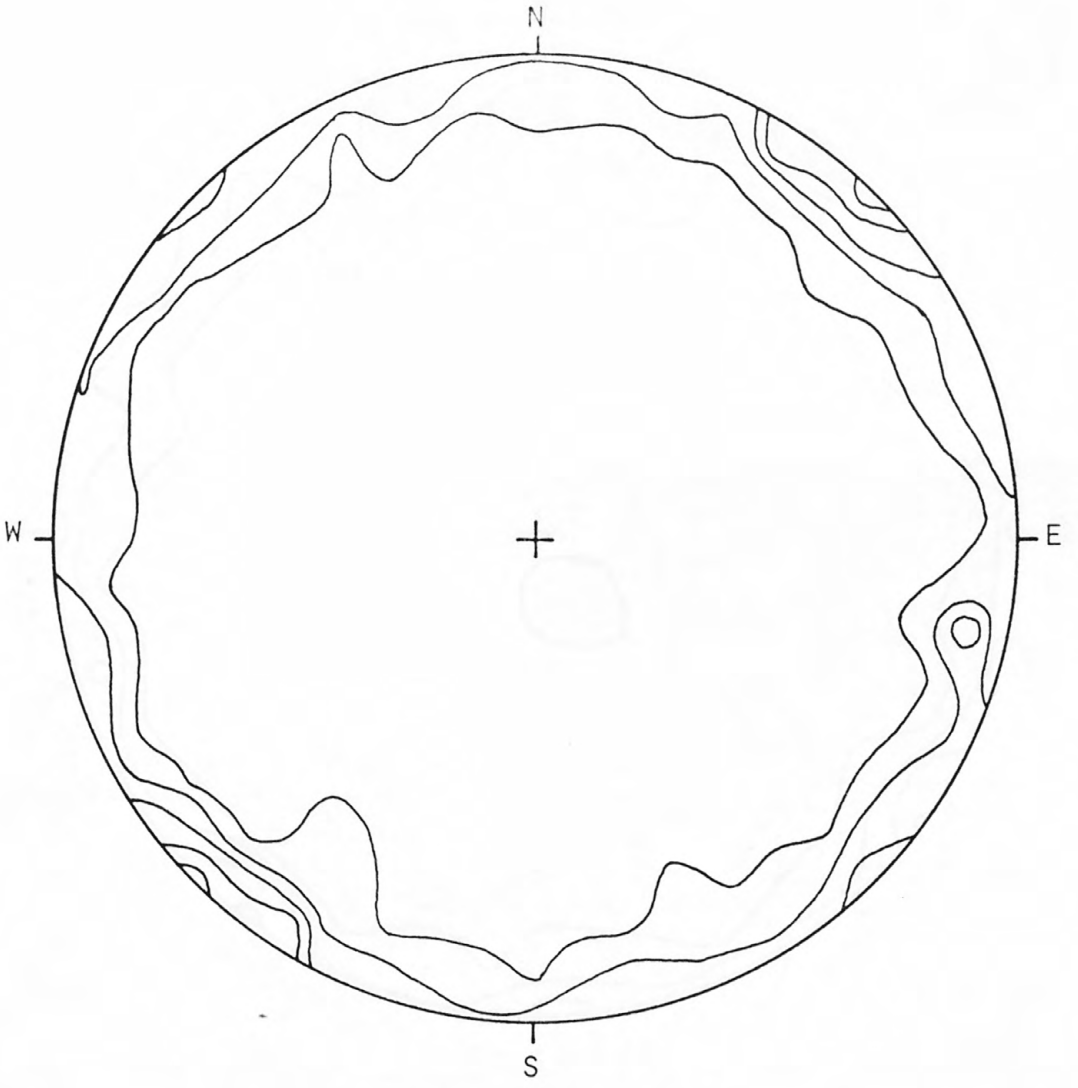

Figure 5. Schmidt diagram for joints in outcrops (less bedding plane fractures), northwestern Powder River Basin.

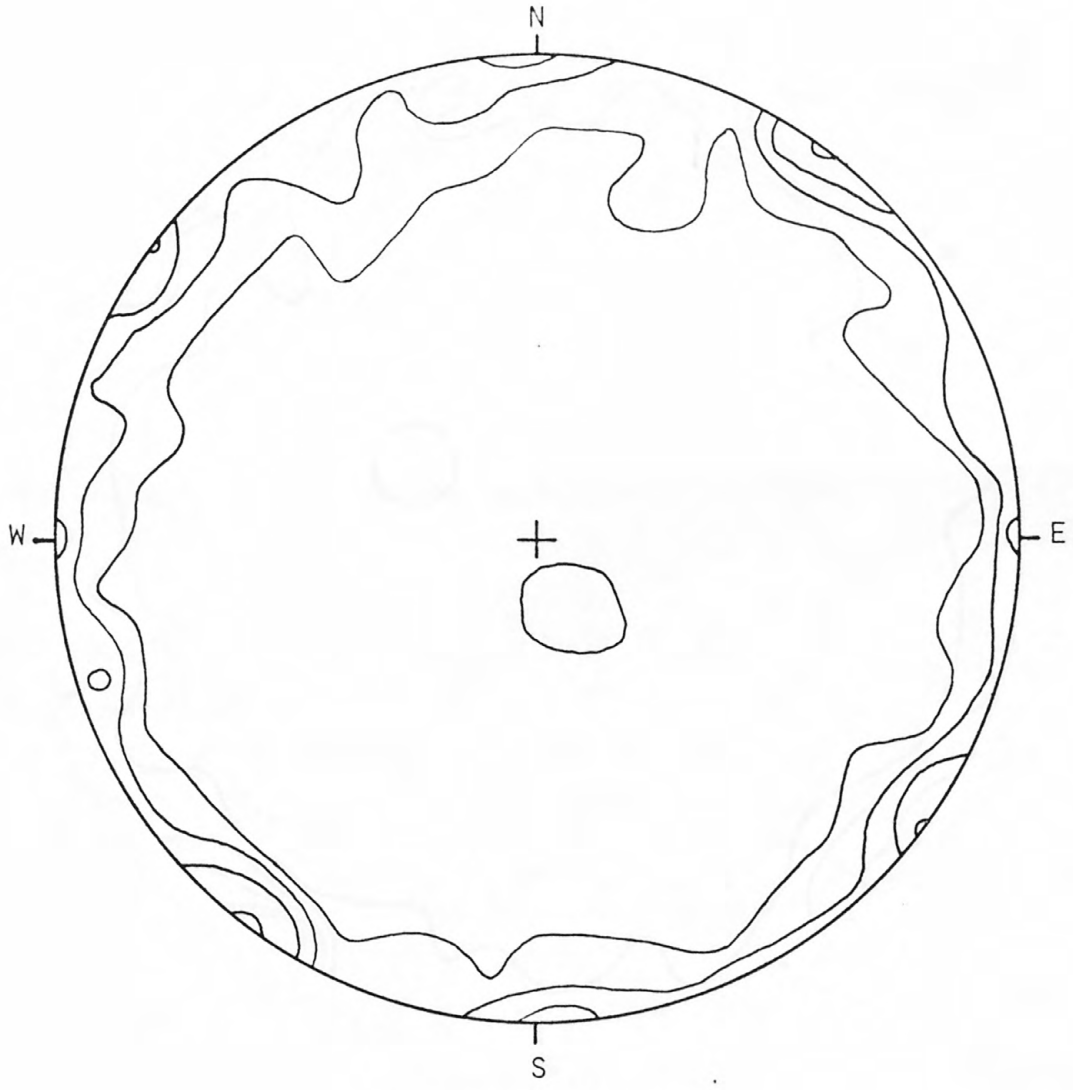

Figure 6. Schmidt diagram for joints in coal and overburden (less bedding plane fractures), Decker mine, Montana.

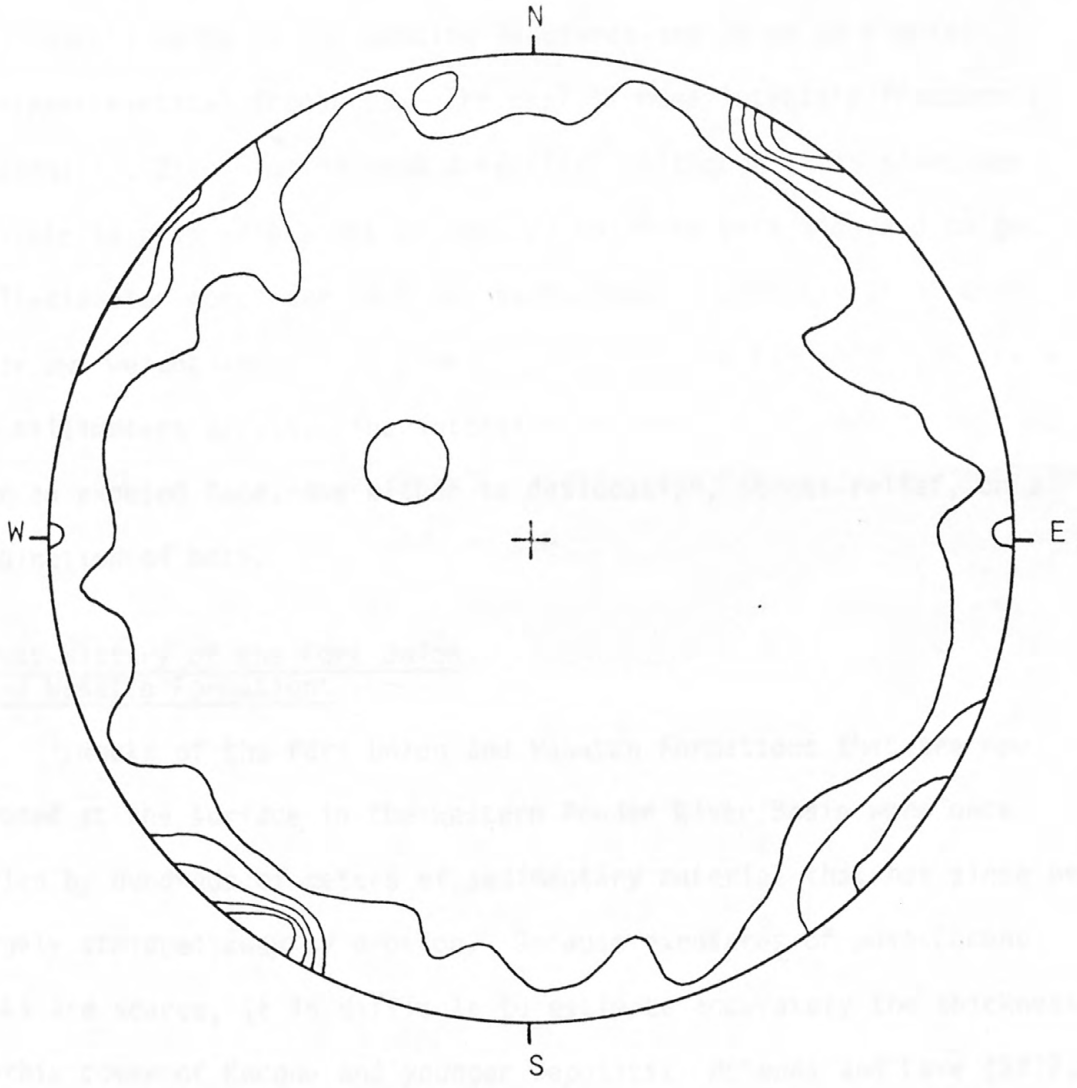

Figure 7. Schmidt diagram for joints in coal (less bedding plane fractures), Decker, Big Horn, Welch, and abandoned mines.

a spacing of 10 to 50 cm. In the more resistant sandstones the spacings are about 10 to 50 cm for bedding fractures and 30 cm to 2 m for prominent vertical fractures. The coal is more intensely fractured; spacings are 2 to 5 cm in each direction. Although it is sometimes possible to pick up a block of coal 20 to 30 cm on a side and to get small-diameter cores for testing, such blocks frequently break under their own weight and can be broken apart with the hands into pieces a few millimeters across. The intensity of fracturing tends to be greater near an exposed face, due either to desiccation, stress-relief, or a combination of both.

Stress History of the Fort Union and Wasatch Formations

Rocks of the Fort Union and Wasatch Formations that are now exposed at the surface in the western Powder River Basin were once buried by hundreds of meters of sedimentary material that has since been largely stripped away by erosion. Because exposures of post-Eocene rocks are scarce, it is difficult to estimate accurately the thickness of this cover of Eocene and younger deposits. McKenna and Love (1972, p. 5, Fig. 2B), however, estimated a thickness of 1200 m of post-Paleocene rocks, based on correlation of Oligocene rocks in the Bighorn Mountains and at Pumpkin Buttes in the middle of the Powder River Basin (80 km southeast of Sheridan). Once this maximum thickness was attained, probably in late Miocene or early Pliocene time, the sediments were eroded in a relatively short interval of late Cenozoic time (McKenna and Love, 1972, p. 9).

From the geologic evidence one can calculate approximate values for the maximum horizontal and vertical stresses. Using the rule of thumb for vertical overburden stress of 22.6 kPa/m (1 lb/in.^{2}/ft of depth) and with 1200 m of maximum overburden, the maximum vertical stress is about 27 MPa. The maximum horizontal stress due to this vertical load can be approximated by the formula (Jaeger and Cook, 1969, p. 356)

$$\sigma_h = \frac{\nu}{1-\nu} \sigma_v \qquad (1)$$

which allows no lateral deformation during application of the vertical load. Using an average Poisson's ratio, ν, of 0.4, equation (1) yields a maximum horizontal stress of about 18 MPa; if ν = 0.25 the maximum horizontal stress is 9 MPa. Depending on the subsequent history of the material, and particularly the strength of grain bonding, typical clayey rocks may have retained a significant portion of this applied stress in the form of recoverable residual stresses.

Horizontal residual stresses may have a significant effect on the stability of natural or excavated slopes and may be manifest through the phenomenon of rebound. Erosion of the 1200 m of overburden has left the Fort Union and Wasatch Formations in a highly overconsolidated state. In highly overconsolidated rocks much greater deformations are experienced after an opening is excavated than in rocks of lesser consolidation states. The rocks can deform laterally only if the lateral confinement of the material is reduced, such as by an eroding stream, a mine, or a highway cut. Once an excavation has been made the horizontal stresses may be relieved, causing bulging of walls and

buckling of floors, and possibly resulting in raised valley rims, as described by Matheson (1972). This stress history is shown diagrammatically in Figure 8. Tensile strains generated by lateral expansion of rock into an excavation might be sufficient to cause fresh fracturing near the slope face. Because such deformation is generally time dependent, fracturing could occur in a progressive manner leading to eventual slope failure.

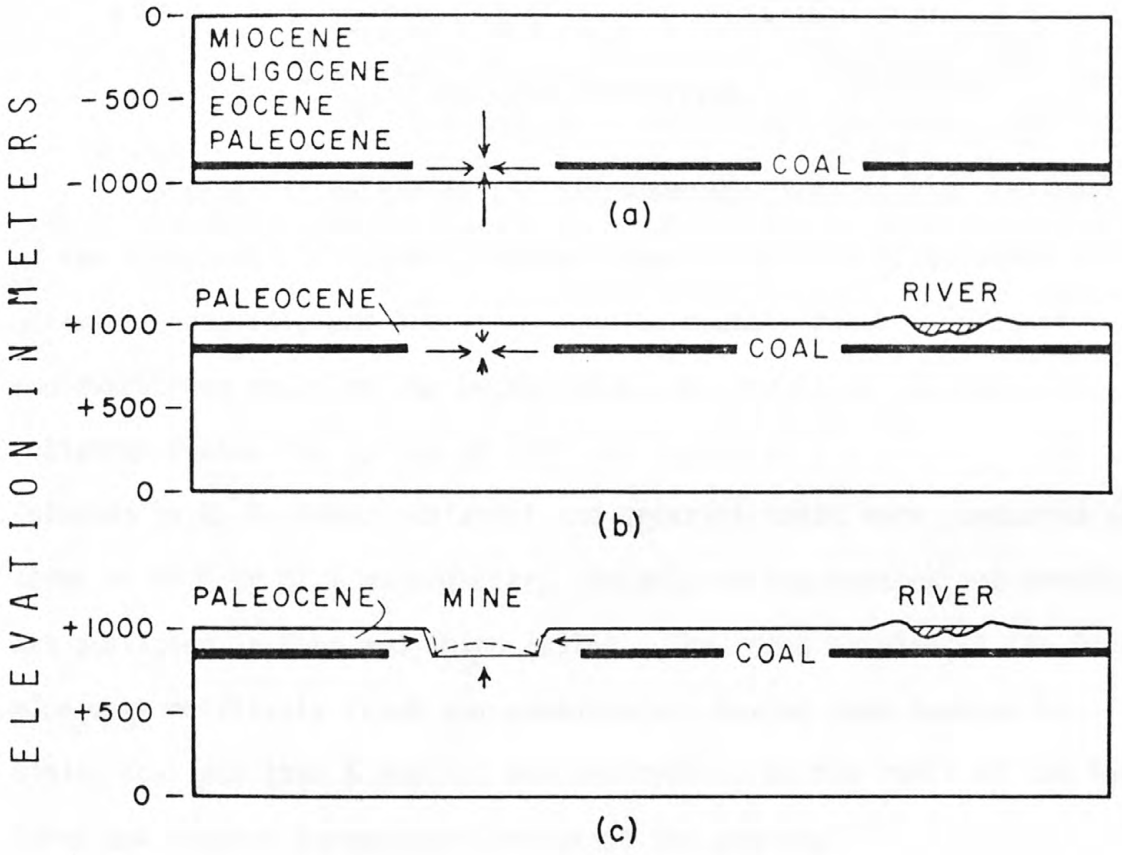

Figure 8. Hypothetical sequence of loading and deformational history in the western Powder River Basin.

Arrows have no scale but represent the relative magnitude of vertical and horizontal stresses at three stages of development. Thickness of coal and rebound deformations are exaggerated. (a) inferred conditions at the time of maximum burial of Fort Union rocks in the western Powder River Basin; (b) inferred conditions after erosion in late Cenozoic time, showing valley rebound; (c) present conditions after start of mining. Estimates for restored section (a) were taken from McKenna and Love (1972, fig. 2B), (from Lee, Smith, and Savage, 1976, p. 28).

PHYSICAL PROPERTIES

In order to determine the geotechnical properties of the rocks of the Fort Union Formation, samples were collected and subjected to uniaxial, triaxial, and Brazilian tension tests. Block samples of coal and overburden rocks at the Decker mine, Montana (Fig. 1), were collected during the spring of 1975 and tested at the University of Colorado by M. P. Fahy. Uniaxial and triaxial tests were conducted on cores of 20.8 or 22.9 mm diameter. Details of the testing and results are published in Fahy and Smith (1976). The rocks sampled at the Decker mine were relatively fresh and unweathered, having been exposed by mining for less than 6 months, and are typical of the rocks of the Fort Union and Wasatch Formations throughout the region.

Analysis of Triaxial Tests

Methods

For analysis of the triaxial compression tests performed by Fahy, peak and residual deviatoric strength values and the confining pressures were analyzed by a computer program, and the results are plotted on p-q diagrams, where

$$p = \frac{\sigma_1 + \sigma_3}{2}, \qquad (2)$$

and

$$q = \frac{\sigma_1 - \sigma_3}{2} . \tag{3}$$

This is equivalent to plotting the tops of the Mohr circles representing the stress conditions for peak and residual strengths on the conventional τ-σ diagrams. These points were subjected to a least squares linear regression analysis to determine the q-intercept, a, and the angle of inclination, α, of the line through the tops of the Mohr circles, called the K_f line (Lambe and Whitman, 1969, p. 141). However, one is really concerned with the envelope that is tangent to the set of Mohr circles. It can be shown that the K_f line

$$q = a + p \tan \alpha \tag{4}$$

is related to the Mohr-Coulomb envelope

$$\tau = c - \sigma \tan \phi \text{ (tension positive)} , \tag{5}$$

by the relationships

$$\sin \phi = \tan \alpha \tag{6}$$

and

$$c = \frac{a}{\cos \alpha} . \tag{7}$$

In the diagrams presented here the K_f line will refer to the peak strength conditions (following Lambe and Whitman, 1969), while K_r will be used for residual strength conditions.

Results

Results of the triaxial tests are listed in Table 3, along with results of other tests, and plotted on graphs of deviator stress vs. confining pressure and on p-q diagrams in Figures 9 through 13. An examination of the data points on the graphs indicates that the true failure envelopes tend to be flatter at higher confining pressures. This effect is more pronounced on the plots of deviator stress vs. confining pressure than on the p-q diagrams. In several cases the linear regression of q on p resulted in slightly higher residual friction angles than peak friction angles, although the projected envelopes do not intersect within the range of the tests because of the lower residual cohesion. This apparent discrepancy might be accounted for by the inherent variability of the data and the resulting uncertainty in the slope of the regression line within 90-percent confidence limits, or, more likely, by the curved nature of the envelopes. The same effect (curved failure envelopes) was also noted by Singh, Henkel, and Sangrey (1973) in testing of overconsolidated, remolded Bearpaw Shale. They pointed out that extrapolation of the data for low normal stresses indicates a cohesion intercept of zero. Unfortunately, no satisfactory method of analysis is readily available that utilizes a curved failure envelope of this type.

Table 3. Physical-property test results for samples from Decker mine, Montana.

[Analyst: M. P. Fahy, University of Colorado]

Rock description	Sample number	Density (g/cm)	Confining pressure (kPa)	Young's modulus (GPa)	Poisson's ratio	Peak compressive strength (MPa)	Residual compressive strength (MPa)	Braz. tens. strength (MPa)	Remarks
SHALE - med gray calcareous, has many thin bituminous laminae along which cores tend to split. Samples 1A left unwrapped at 95% humidity for 2-3 days before testing.	1-1	2.38	0	0.54	--	7.81	0	3.172	
	1-2	2.33	345	0.447	--	9.54	3.75	3.813	
	1-3	2.30	690	0.236	--	6.27	--	0.917	
	1A-4	2.33	0	0.757	0.49	22.80	0	3.716	
	1-5	2.34	1 380	0.215	--	5.83	5.20	3.537	
	1A-6	2.34	2 070	0.351	--	8.23	7.88	1.048	
	1A-7	2.31	2 760	0.336	--	8.25	7.19	0.610	
	1-8	2.33	3 450	0.269	--	6.04	5.85	2.699	
	1-9	2.60	5 170	2.26	--	40.40	--	1.014	
	1-10	2.33	6 900	0.209	--	7.06	5.80	2.220	
	1-11	2.54	10 300	2.41	--	39.40	33.80	0.779[a]	
	1-12	2.39	0	0.244	--			2.331[a]	
			1 720	0.444	--				Cyclic loading
			3 450	0.611	--				
			6 900	0.652	--				
			10 300	0.690	--	10.40			
	1-13	2.36	0	--	0.56[b]	--	--	0.662[a]	
	1-14A	--	--	--	--	--	--	1.786[a]	
	1-15A	--	--	--	--	--	--	0.501[a]	
SHALE - silty, dark gray, some calc. layers. Samples small and crumbly. No cores obtained.	2-1	--	--	--	--	--	--	0.869	
	2-2	--	--	--	--	--	--	0.463	
	2-3	--	--	--	--	--	--	0.166	
	2-4	--	--	--	--	--	--	0.132	
SHALE - med. gray, calcareous, few thin bituminous laminae. Stored unwrapped at 95% humidity.	3A-1	2.28	0	1.29	--	18.10	0	2.551	
	3A-2	2.27	690	1.28	--	19.10	9.10	3.227	
	3A-3	2.33	345	1.88	--	24.40	7.50	2.765	
	3A-4	2.29	1 720	1.29	--	20.60	11.30	3.427	
	3A-5	2.25	3 450	1.60	--	24.70	17.20	2.462	
	3A-6	2.38	1 380	1.28	--	15.30	10.20	2.399	
	3A-7	2.29	2 070	1.67	--	27.20	13.00	2.358	
	3A-8	2.25	2 760	1.50	--	25.60	15.00	2.813	
	3A-9	2.31	5 170	1.90	--	31.40	16.30	2.413	
	3A-10	2.34	6 900	2.12	--	38.10	23.10	2.606	
	3A-11	2.30	10 300	1.95	--	36.60	26.40	1.903	
	3A-12	--	0	1.29	--			1.531	
			1 720	1.84	--				Cyclic loading
			3 450	2.24	--				
			5 170	2.53	--				
			10 300	2.94	--	40.20	28.30		
	3A-13	2.27			0.15			0.924	
	3A-14	2.33	0	1.81	--	19.10	0	1.572	
	3A-15	2.36	0	1.64	0.44	16.30	0	1.241	
	3A-16	--	--	--	--	--	--	0.855[c]	
	3A-17	--	--	--	--	--	--	1.262[c]	
	3A-18	--	--	--	--	--	--	0.779[c]	
	3A-19	--	--	--	--	--	--	0.883[c]	
	3A-20	--	--	--	--	--	--	0.958[c]	
	3A-21	--	--	--	--	--	--	0.841[c]	
SILTSTONE - sandy, white to tan, calcareous, crumbly, poorly cemented. Stored unwrapped at 95% humidity.	3B-1	2.15	--	--	0.57[b]	--	--	--	
	3B-2	2.08	0	0.884	--	7.75	0	0.372	
	3B-3	2.14	0	0.867	0.36	7.25	0	0.400	
	3B-4	2.13	345	0.879	--	8.31	3.15	0.359	
	3B-5	2.04	690	1.00	--	9.35	5.25	0.469	
	3B-6	2.17	1 380	0.775	--	11.00	6.35	0.607	
	3B-7	2.16	2 070	1.55	--	16.70	10.60	0.503	
	3B-8	2.11	2 760	1.71	--	17.50	13.10	0.600	
	3B-9	2.08	3 450	1.98	--	21.60	15.00	0.614	
	3B-10	2.11	5 170	2.16	--	25.00	18.40	0.476	
	3B-11	2.10	6 900	2.26	--	25.00	20.50	0.600	
	3B-12	2.11	10 300	2.27	--	27.50	26.30	0.476	
	3B-13	2.09	0	0.965	--	--	--	0.421[a]	
			1 720	1.91	--	--	--	--	Cyclic loading
			3 450	2.47	--	--	--	--	
			6 900	3.26	--	--	--		
			10 300	4.15	--	28.40	27.50		
	3B-14	2.09	0	0.799	0.40	4.00	0	0.393[a]	Cored ⊥ to bd.
	3B-15	--	--	--	--	--	--	0.494[a]	
	3B-16	--	--	--	--	--	--	0.228[a]	
	3B-17	--	--	--	--	--	--	0.324[a]	
	3B-18	--	--	--	--	--	--	0.379[a]	
SHALE - calcareous, med. gray, grading to brown clayey limestone.	3C-1	2.36	0	--	0.30	--	--	2.165	
	3C-2	2.42	0	1.50	--	17.30	0	2.620	
	3C-3	2.36	0	1.28	--	--	--	1.993	
			1 720	1.55	--	--	--		Cyclic loading
			3 450	1.90	--	--	--		
			6 900	2.50	--	--	--		
			10 300	3.26	--	38.00	34.00		
	3C-4	--	--	--	--	--	--	2.972	
	3C-5	--	--	--	--	--	--	1.517	
	3C-6	--	--	--	--	--	--	2.620	
	3C-7	--	--	--	--	--	--	1.944	
	3C-8	--	--	--	--	--	--	2.786	
	3C-9	--	--	--	--	--	--	1.758	
	3C-10	--	--	--	--	--	--	2.675	
	3C-11	--	--	--	--	--	--	5.000	
	3C-12	--	--	--	--	--	--	2.248	
	3C-13	--	--	--	--	--	--	13.380	
	3C-14	--	--	--	--	--	--	31.500	
	3C-15	--	--	--	--	--	--	12.390	
	3C-16	--	--	--	--	--	--	5.726	
SILTSTONE - sandy, calcareous, gray to brownish gray, very fine grained, dense, hard. Contains about 47% $CaCO_3$ cement.	3D-1	2.82	0	9.98	0.81[b]	--	--	16.160	
			1 720	12.2	--	--	--		Cyclic loading
			3 450	14.1	--	--	--		
			5 170	12.5	--	97.00	48.10		
	3D-2	2.58	0	6.60	--	45.00	0	10.200	
	3D-3	--	--	--	0.47	--	--	8.130	
	3D-4	2.60	1 720	6.02	--	60.00	22.30	7.550	
	3D-5	2.73	3 450	14.1	--	103.00	35.20	12.400	
	3D-6	2.79	6 900	15.3	--	135.00	48.50	4.990	
	3D-7	--	--	--	--	--	--	13.340	
	3D-8	--	--	--	--	--	--	13.400	
	3D-9	--	--	--	--	--	--	11.600	
	3D-10	--	--	--	--	--	--	7.950	
	3D-11	--	--	--	--	--	--	10.900[a]	
	3D-12	--	--	--	--	--	--	14.300[a]	
	3D-13	--	--	--	--	--	--	7.300[a]	
	3D-14	--	--	--	--	--	--	8.730[a]	
COAL - subbituminous, black, blocky. Contains two major cleat planes perpendicular to bd. and to each other, cleat-plane spacing about 5-7.5 cm, exhibits subconchoidal fracture.	4-1	1.31	--	--	0.36	--	--	2.280	
	4-2	1.32	--	--	0.37	--	--	1.730	
	4A-3	1.32	--	--	0.43	--	--	2.490	
	4-4	1.34	0	2.20	--	20.00	0	1.180	
	4-5	1.32	0	2.03	--	25.50	0	1.900	
	4A-6	1.33	0	1.51	--	19.00	0	2.090	
	4A-7	1.33	345	1.74	--	23.10	9.00	1.450	
	4A-8	1.33	690	1.97	--	28.80	10.00	1.090	
	4-9	1.33	1 380	1.68	--	24.40	14.10	2.300	
	4-10	1.31	2 070	1.63	--	28.80	18.40	1.875	
	4-11	1.31	2 760	1.93	--	31.40	20.00	0.669	
	4A-12	1.32	3 450	2.24	--	37.80	19.40	1.155	
	4-13	1.29	5 170	1.75	--	40.00	22.80	1.138	
	4-14	1.32	6 900	2.16	--	35.90	30.00	1.262	
	4A-15	1.32	10 300	2.02	--	33.10	29.70	1.860	
	4A-16	1.31	0	2.17	--	--	--	2.241[a]	
			1 720	2.15	--	--	--		Cyclic loading
			3 450	2.25	--	--	--		
			5 170	2.05	--	--	--		
			6 900	2.05	--	--	--		
			10 300	2.05	--	39.10	37.20		
	4-17	--	--	--	--	--	--	2.475[a]	
	4-18	--	--	--	--	--	--	1.282[a]	

[a] Loaded at an oblique angle to bedding.

[b] Poisson's ratio greater than 0.5 means that sample dilated during testing.

[c] Loaded parallel to bedding. Other Brazilian test specimens loaded perpendicular to bedding.

Figure 9. Results of triaxial tests on shale #1, Decker mine, Montana.

(a) Deviator stress vs. confining pressure

(b) p-q diagram, showing regression lines for peak and residual strengths

Explanation

△ Peak strength values

⊙ Residual strength values

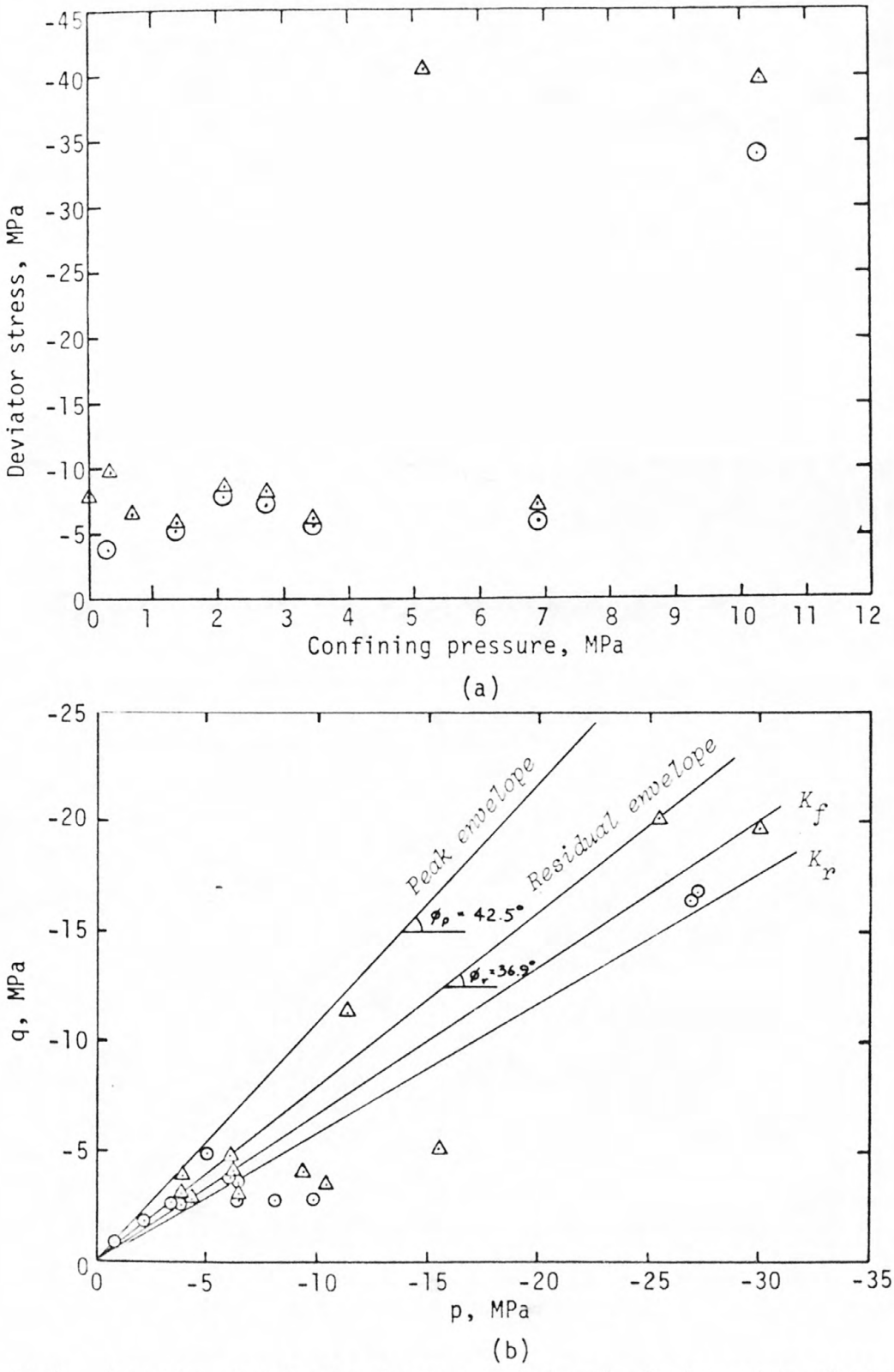

Figure 9. Results of triaxial tests on shale #1, Decker mine, Montana.

Figure 10. Results of triaxial tests on shale #3A, Decker mine, Montana.

(a) Deviator stress vs. confining pressure

(b) p-q diagram, showing regression lines for peak and residual strengths

Explanation

△ Peak strength values

⊙ Residual strength values

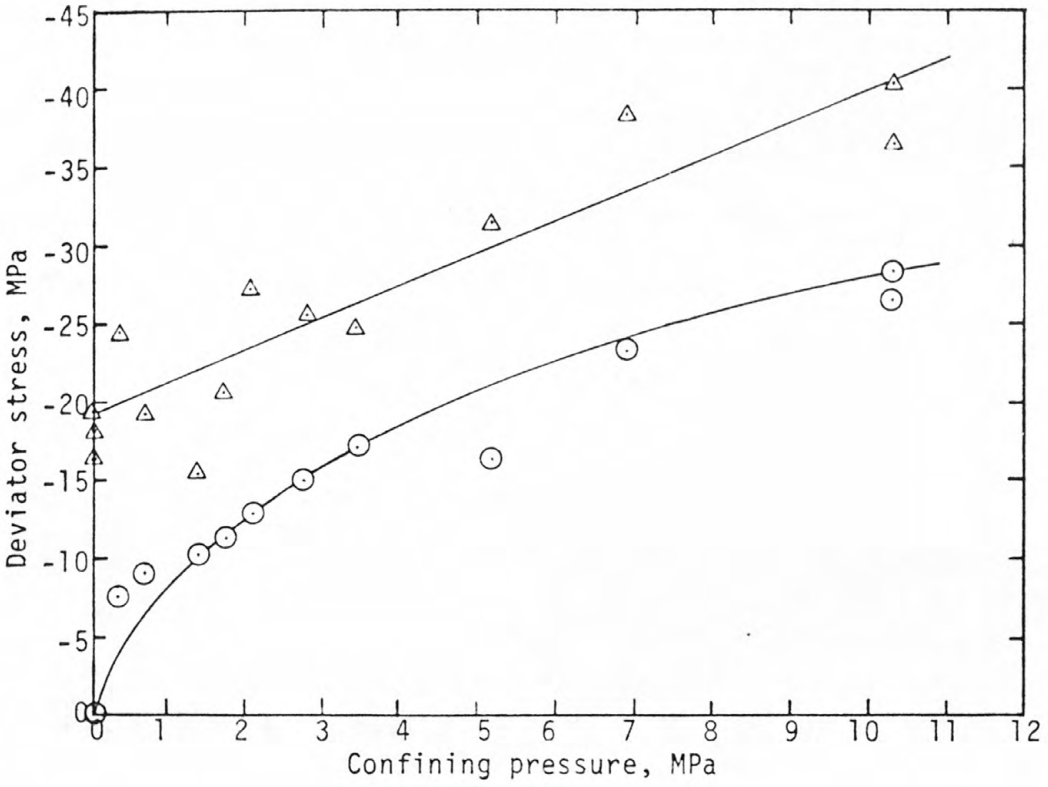

(a)

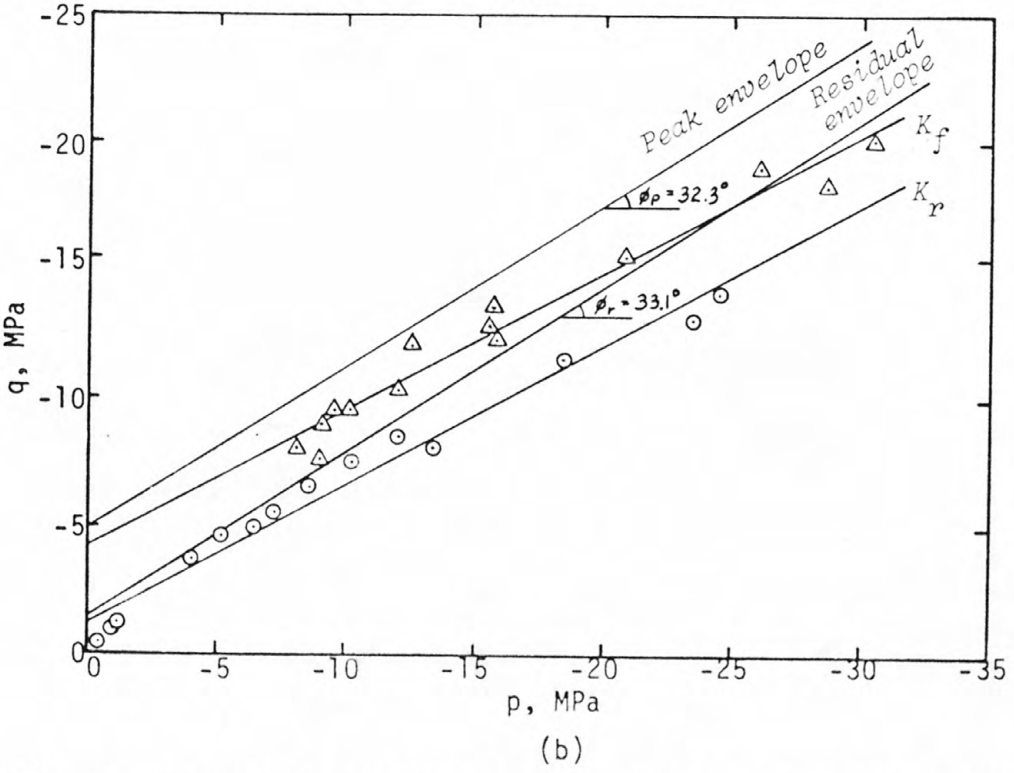

(b)

Figure 10. Results of triaxial tests on shale #3A, Decker mine, Montana.

Figure 11. Results of triaxial tests on siltstone #3B, Decker mine, Montana.

(a) Deviator stress vs. confining pressure

(b) p-q diagram, showing regression lines for peak and residual strengths

Explanation

△ Peak strength values

⊙ Residual strength values

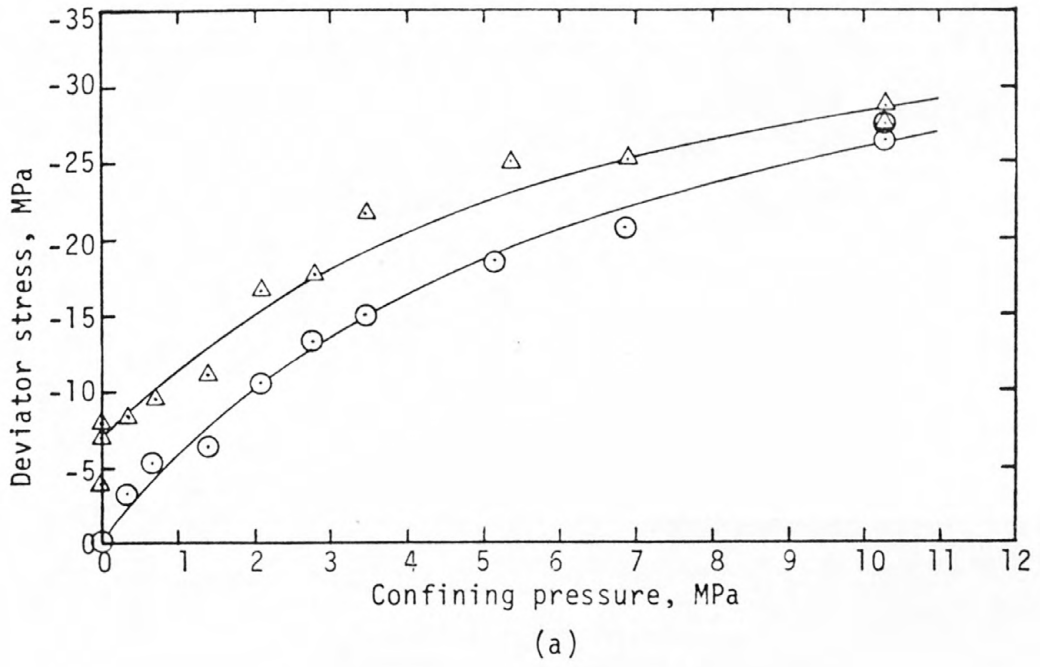

(a)

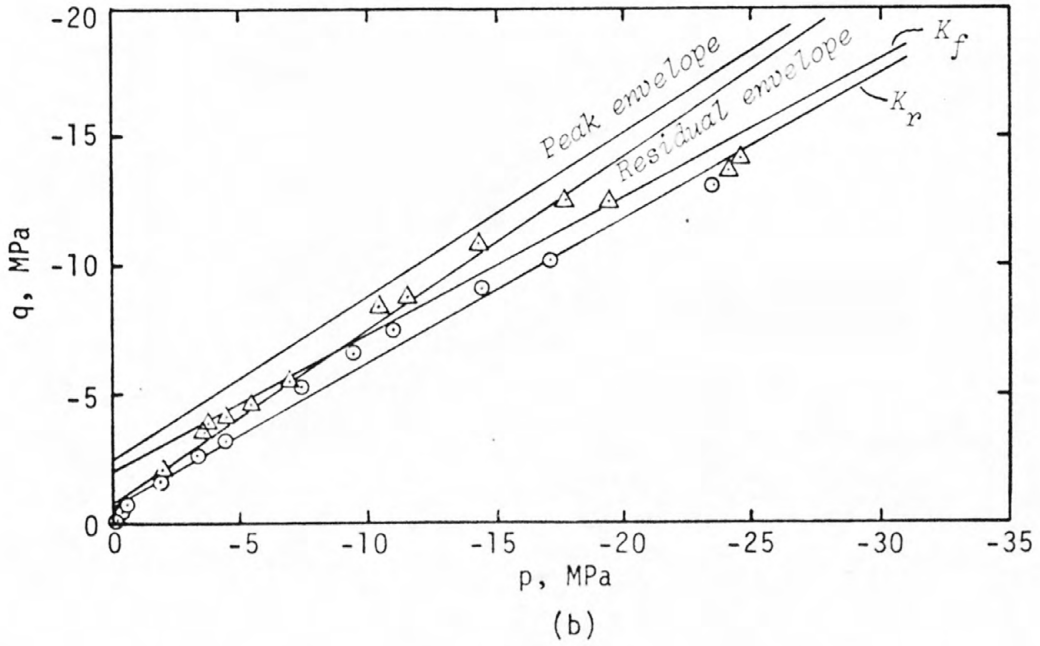

(b)

Figure 11. Results of triaxial tests on siltstone #3B, Decker mine.

Figure 12. Results of triaxial tests on limy siltstone #3D, Decker mine, Montana.

(a) Deviator stress vs. confining pressure

(b) p-q diagram, showing regression lines for peak and residual strengths

Explanation

△ Peak strength values

⊙ Residual strength values

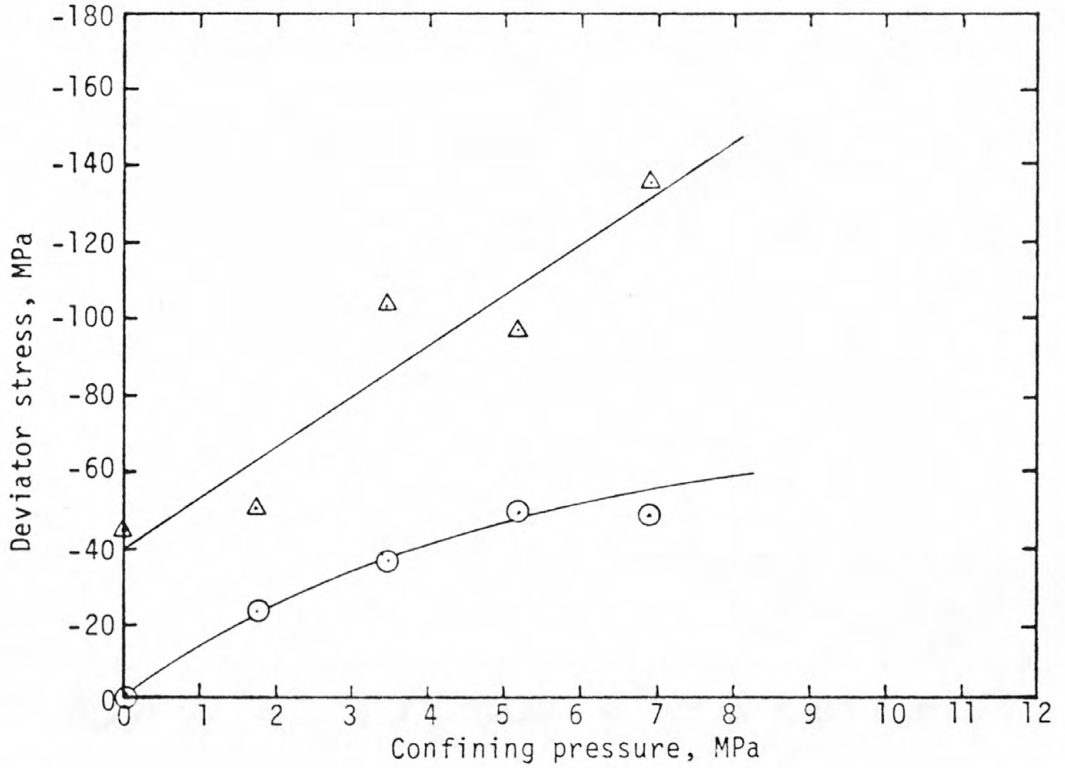

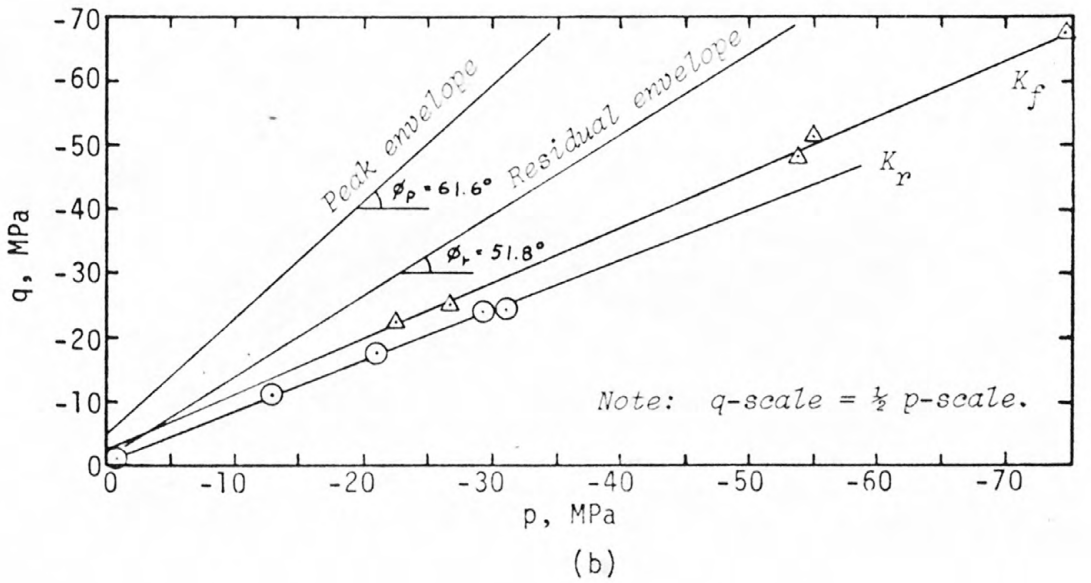

Figure 12. Results of triaxial tests on limy siltstone #3D.

Figure 13. Results of triaxial tests on coal #4 and 4A, Decker mine, Montana.

(a) Deviator stress vs. confining pressure

(b) p-q diagram, showing regression lines for peak and residual strengths

Explanation

△ Peak strength values

⊙ Residual strength values

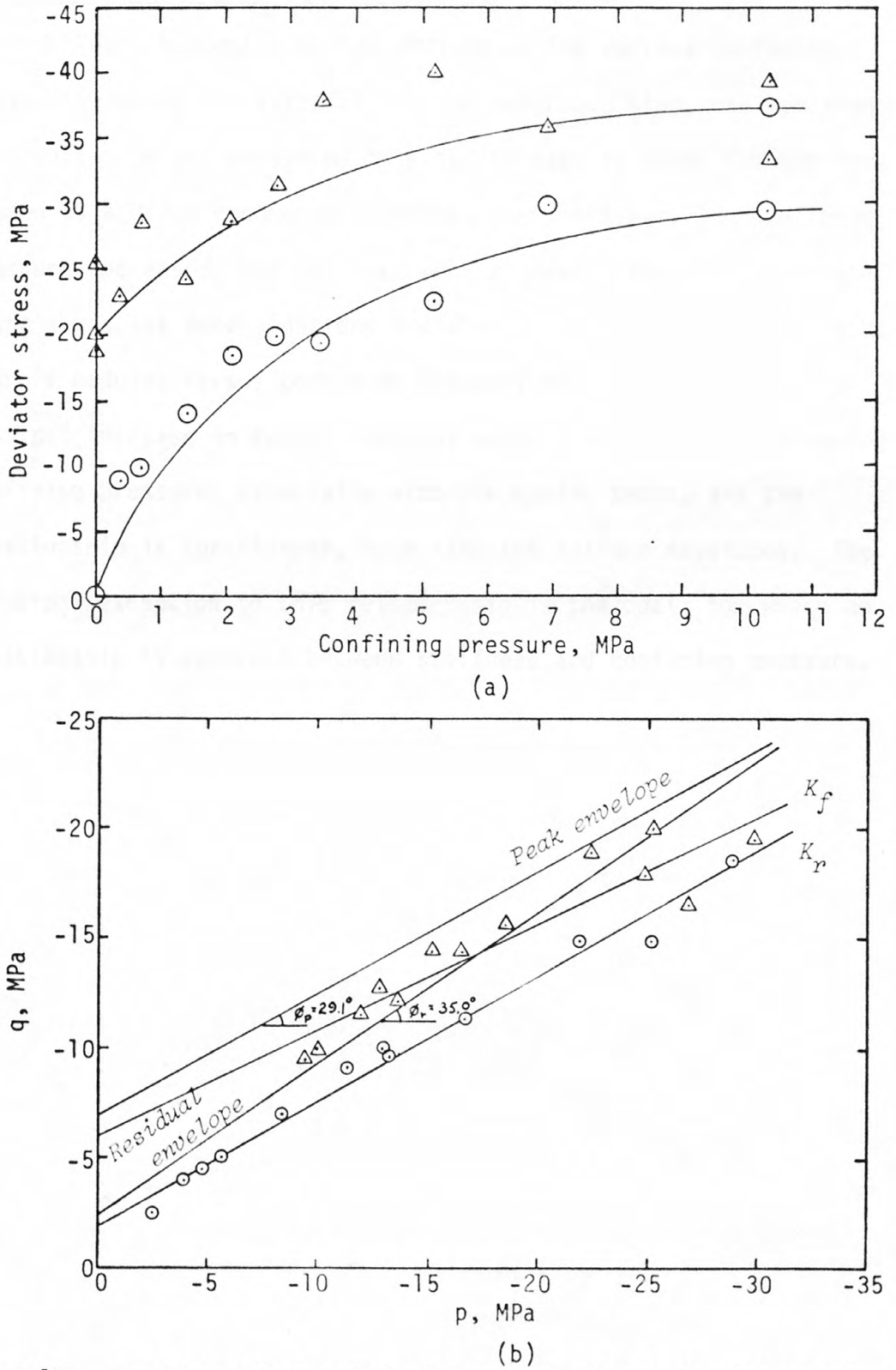

Figure 13. Results of triaxial tests on coal #4 and 4A, Decker mine.

Effect of Confining Pressure on Young's Modulus

Young's modulus was determined at the various confining pressures during the triaxial testing program. Also, one specimen of each rock type was subjected to a cyclic test in which the specimen was loaded at a given confining pressure, then unloaded, the confining pressure increased, and the specimen reloaded. The results of the Young's modulus determinations are also given in Table 3 and graphs of Young's modulus versus confining pressure are shown in Figure 14. A distinct increase in Young's modulus usually occurs with increasing confining pressure, especially with the cyclic tests, and the relationship is curvilinear, much like the failure envelopes. The principal exception to this relationship is the coal, for which no relationship is apparent between stiffness and confining pressure.

Figure 14. Young's modulus as a function of confining pressure for triaxial tests.

(a) Shale #1

(b) Shale #3A

(c) Siltstone #3B

(d) Shale #3C

(e) Limy siltstone #3D

(f) Coal #4 and 4A

Explanation

⊙ Single load test

△ Cyclic loading test

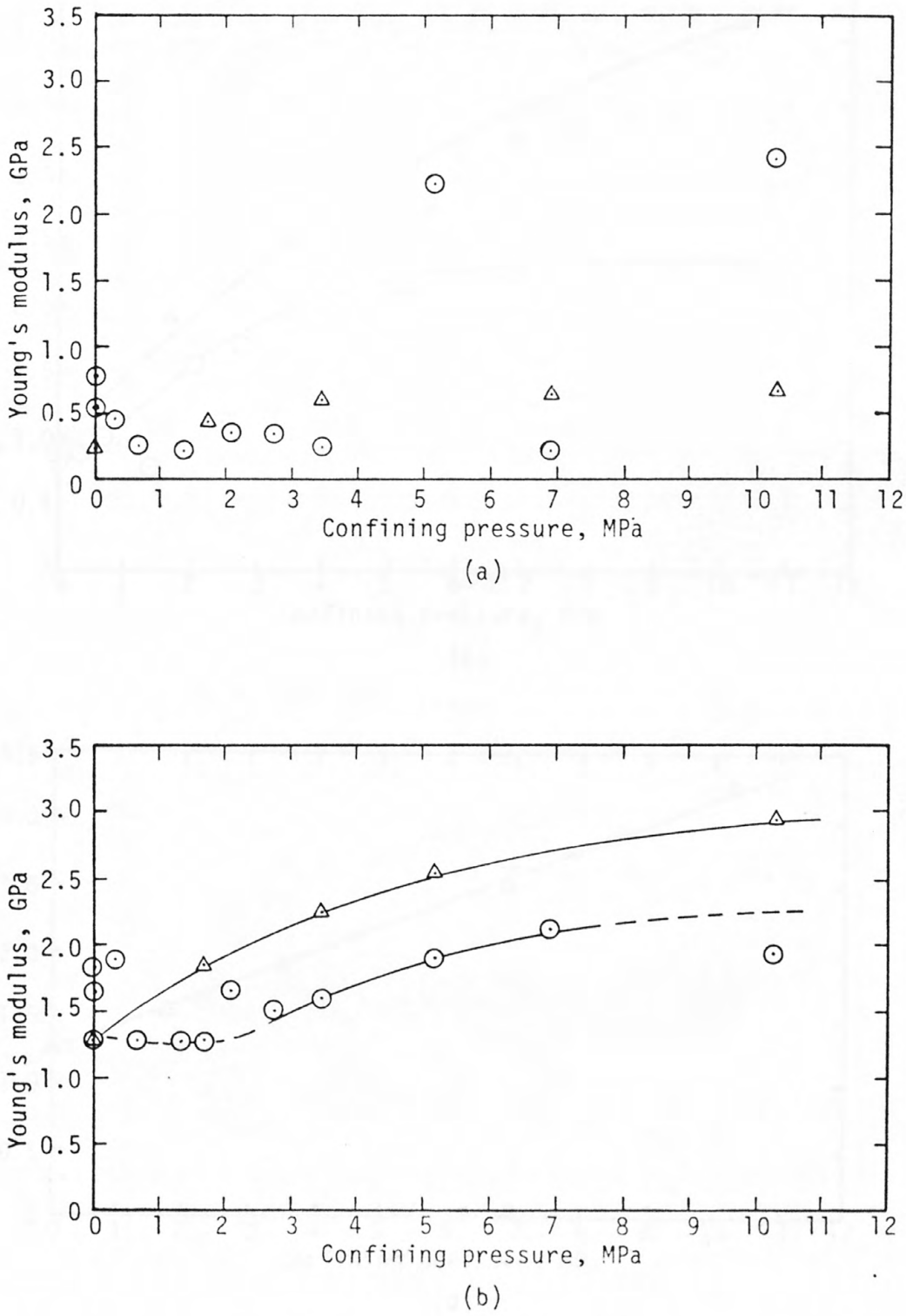

Figure 14. Young's modulus as a function of confining pressure.

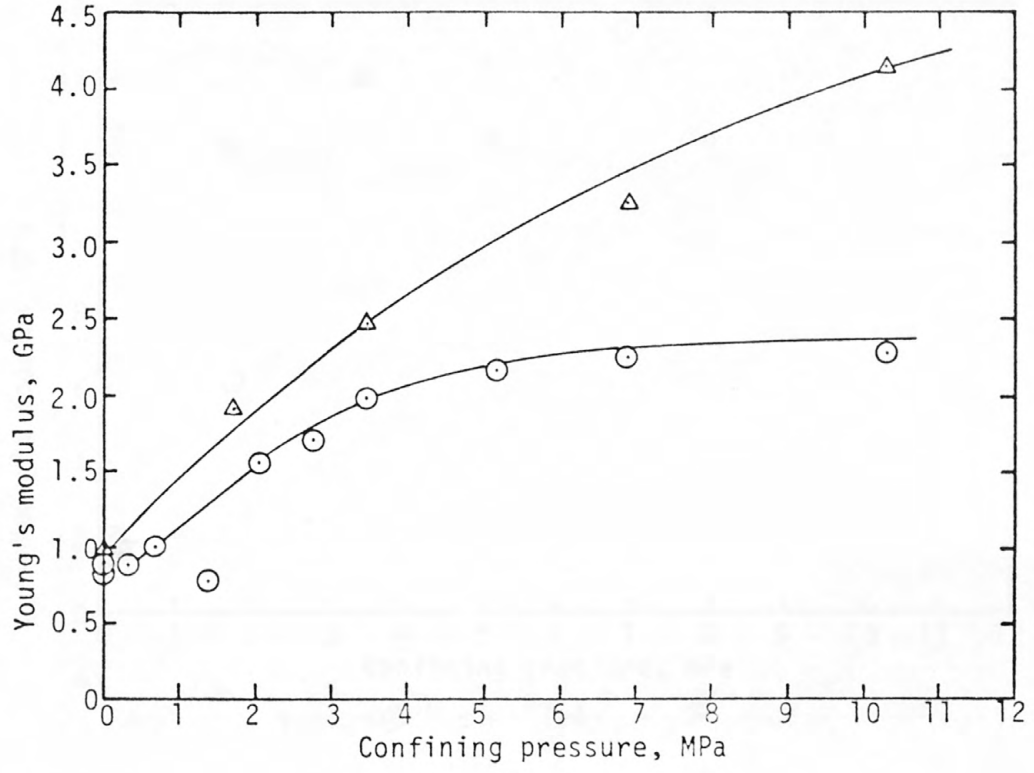

(c)

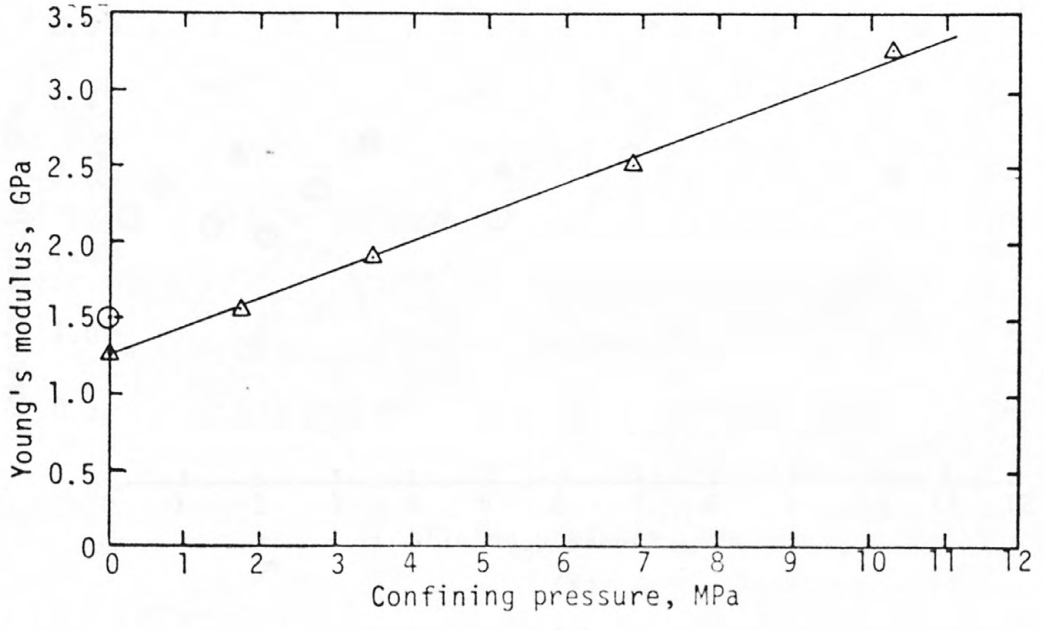

(d)

Figure 14, Continued

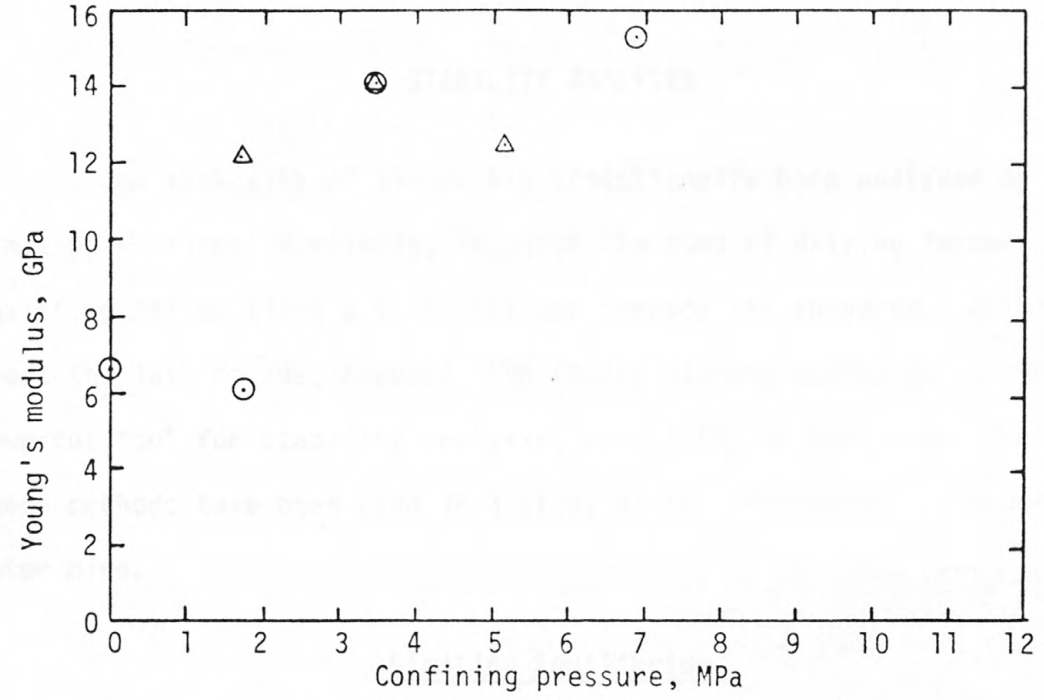

(e)

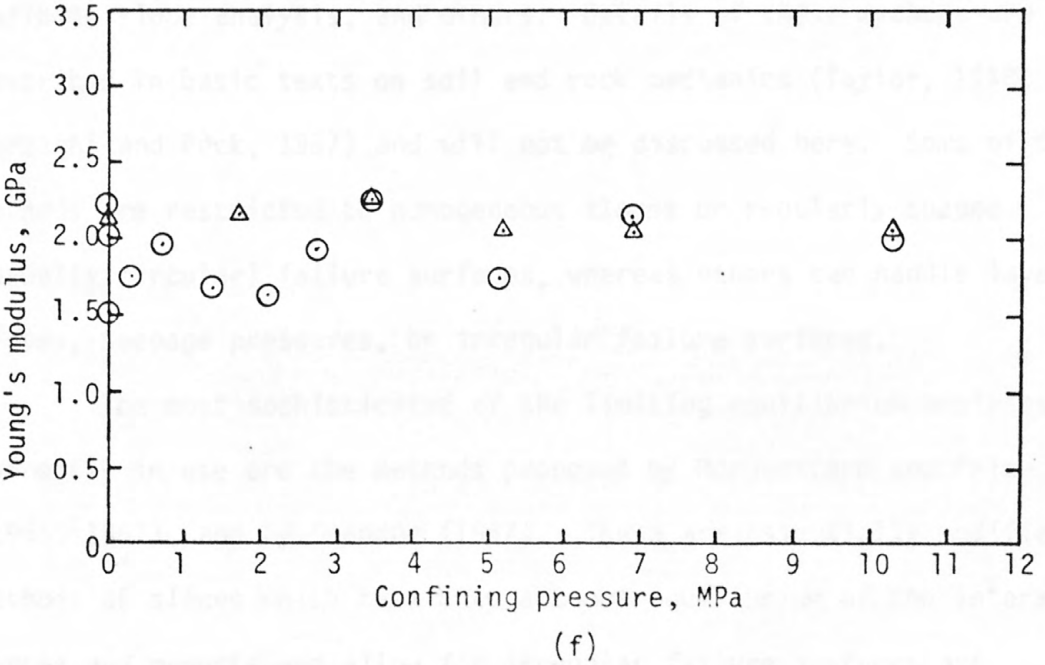

(f)

Figure 14, Continued

STABILITY ANALYSIS

The stability of slopes has traditionally been analyzed by limiting equilibrium methods, in which the sums of driving forces and resisting forces along a trial failure surface are compared. Within about the last decade, however, the finite element method has become a powerful tool for stability analysis, especially in hard rock. Both of these methods have been used in a study of the failure at the Hidden Water mine.

Limiting Equilibrium

Several different limiting equilibrium analyses are available, such as the friction circle method, method of slices, plane sliding, infinite slope analysis, and others. Details of these methods are described in basic texts on soil and rock mechanics (Taylor, 1948; Terzaghi and Peck, 1967) and will not be discussed here. Some of these methods are restricted to homogeneous slopes or regularly shaped (usually circular) failure surfaces, whereas others can handle layered slopes, seepage pressures, or irregular failure surfaces.

The most sophisticated of the limiting equilibrium analyses currently in use are the methods proposed by Morgenstern and Price (1965, 1967), and by Spencer (1967). These are essentially modified methods of slices which take into account equilibrium of the interslice forces and moments and allow for irregular failure surfaces and consideration of pore-water pressures. A digital computer is required

for these analyses. The difference between these two methods lies in the assumptions made to render the problem statically determinant. Spencer's method assumes that the interslice forces are parallel to each other, whereas Morgenstern and Price assumed a variable f(x) distribution (ratio of interslice shear to normal forces) along the failure surface and compute a scaling factor, λ. The problem with a Morgenstern-Price analysis lies in selecting the proper f(x) distribution to produce an "acceptable" solution, that is, one in which the vertical safety factor along the interslice boundaries is everywhere greater than one, and the position of the line of thrust lies within the range 0.15 h to 0.85 h above the base of the slice, where h is the height of the slice (Chowdhury, 1978, p. 347). It is generally difficult to satisfy both of these conditions everywhere within the slope. An analysis of the failure at the Hidden Water mine using Spencer's method is given on page 59.

Finite Element Analysis

The finite element method is a mathematical technique based on the principles of variational calculus and continuum mechanics in which a complex system is subdivided into smaller regions (elements), each with a set of known properties, which are interconnected at a series of points (nodes). The method was developed in the late 1950's and early 1960's for the solution of structural engineering problems. Starting about 1966 the method was applied to problems in slope stability and other areas of rock mechanics, and since then the method has been used by hundreds of authors in this and related fields. Details of the

method are given in several texts (Desai and Abel, 1972; Zienkiewicz, 1971) and will not be dwelt upon here. Advantages of the finite element method over limiting equilibrium analyses include:

1. the capability of analyzing more complicated systems, different materials being irregularly distributed,
2. the ability to analyze stress and strain distributions within the rock mass,
3. the ability to redistribute excess stresses around failed zones (with some codes),
4. the ability to incorporate joints and faults in the rock mass into the analysis,
5. the ability to incorporate initial stresses and displacements, allowing us to model the effects of residual stresses in the rock mass, and
6. the ability to analyze problems in three dimensions, although this is rarely done because of the vast increase in computer time and storage requirements.

The method is not without disadvantages, however. Some of these are:

1. More detailed (and expensive) physical property data are required for the finite element method, including Young's modulus, Poisson's ratio, and yield strengths.
2. Finite element codes are more expensive to run than limit equilibrium programs, requiring more storage and longer running times.

3. Large amounts of input data are required, including coordinates of each nodal point and the nodal point numbers of each element. Although several grid generation programs are available, they are usually restricted to quadrilateral elements and do not always give the best element configurations. The cost of preparing the input data is probably more significant than the increased computer time required.
4. The effects of a water table or seepage in a slope stability problem are included only with great difficulty: their inclusion usually requires running another finite element or finite difference program to compute the seepage or neutral forces at the nodal points; these forces are then used as input data for the structural finite element model.

In a purely elastic analysis, stresses in individual elements are allowed to build to any level dictated by the geometry, stiffness, and loading conditions without regard to possible failure occurring in certain elements. An elastic-plastic analysis, on the other hand, incorporates some yield criterion which limits the amount of stress that is allowed to build up in any single element. Any excess stress in that element indicated by elastic theory must then be redistributed to adjacent elements. Results of finite element analyses performed on the Hidden Water mine slide, using both elastic and elastic-plastic analyses, are discussed starting on page 62.

Convergence of Solutions

In order to arrive at an elastic-plastic solution, a computer program first performs an elastic analysis. It then modifies the stiffness of yielded elements and performs a series of iterations designed to converge to the multi-linear elastic-plastic state. A disadvantage of an elastic-plastic analysis is the amount of computer time required. Each iteration requires about the same amount of time as the initial elastic solution, and 5 to 10 or more iterations are required to achieve satisfactory convergence. If the wrong convergence scheme is selected the number of iterations necessary may be much greater. One measure of convergence is the amount by which the deviatoric stress exceeds the yield stress in any element. Another measure of convergence is how closely the factors of safety for yielded elements approach unity. In practice, computed safety factors considerably less than one may be tolerated. The error in computing the safety factor for a trial failure surface is reduced because a safety factor less than one is compensated for by too high a safety factor in adjacent unyielded elements. For the problem analyzed in this paper, the NONLIN code on the U.S. Geological Survey Honeywell computer required just under 3 minutes of CPU time for each iteration. By contrast, the Morgenstern Price code requires less than 10 seconds to analyze three failure surfaces with four different conditions.

Rheology and Yield Criteria

Numerous rheological models have been proposed to simulate the stress-strain-time relationships of rock and soil masses. Some of these models are discussed in basic texts on rock mechanics (Coates, 1967; Jaeger and Cook, 1969) and consist of various combinations of elastic, plastic, and viscous models. In this study a bilinear elastic-plastic model was used, whose idealized stress-strain curve is shown in Figure 15. To simulate post-yield behavior, a strain-hardening parameter, n, may be used. This parameter is the ratio of post-yield modulus to elastic modulus and ranges from zero for elastic-perfectly plastic materials to 1.0 for perfectly elastic materials.

The location of the yield point in Figure 15 requires the concept of a yield criterion. A yield criterion is a relationship between the principal stresses such that, if the criterion is satisfied, the material becomes ductile (Jaeger and Cook, 1969, p. 216) or ruptures. Examples are the maximum shear stress or Tresca, the familiar Mohr-Coulomb, the von Mises, and Griffith criteria. The von Mises criterion is widely used for metals but has also been applied to rocks (Varnes, 1962), and the Griffith criterion is often used for brittle materials.

Probably the best criterion for soils and soft rocks is the generalized Mohr-Coulomb criterion proposed by Drucker and Prager (1952). The Mohr-Coulomb criterion

$$\tau = c - \sigma \tan \phi \qquad (5)$$

does not account for the effect of the intermediate principal stress.

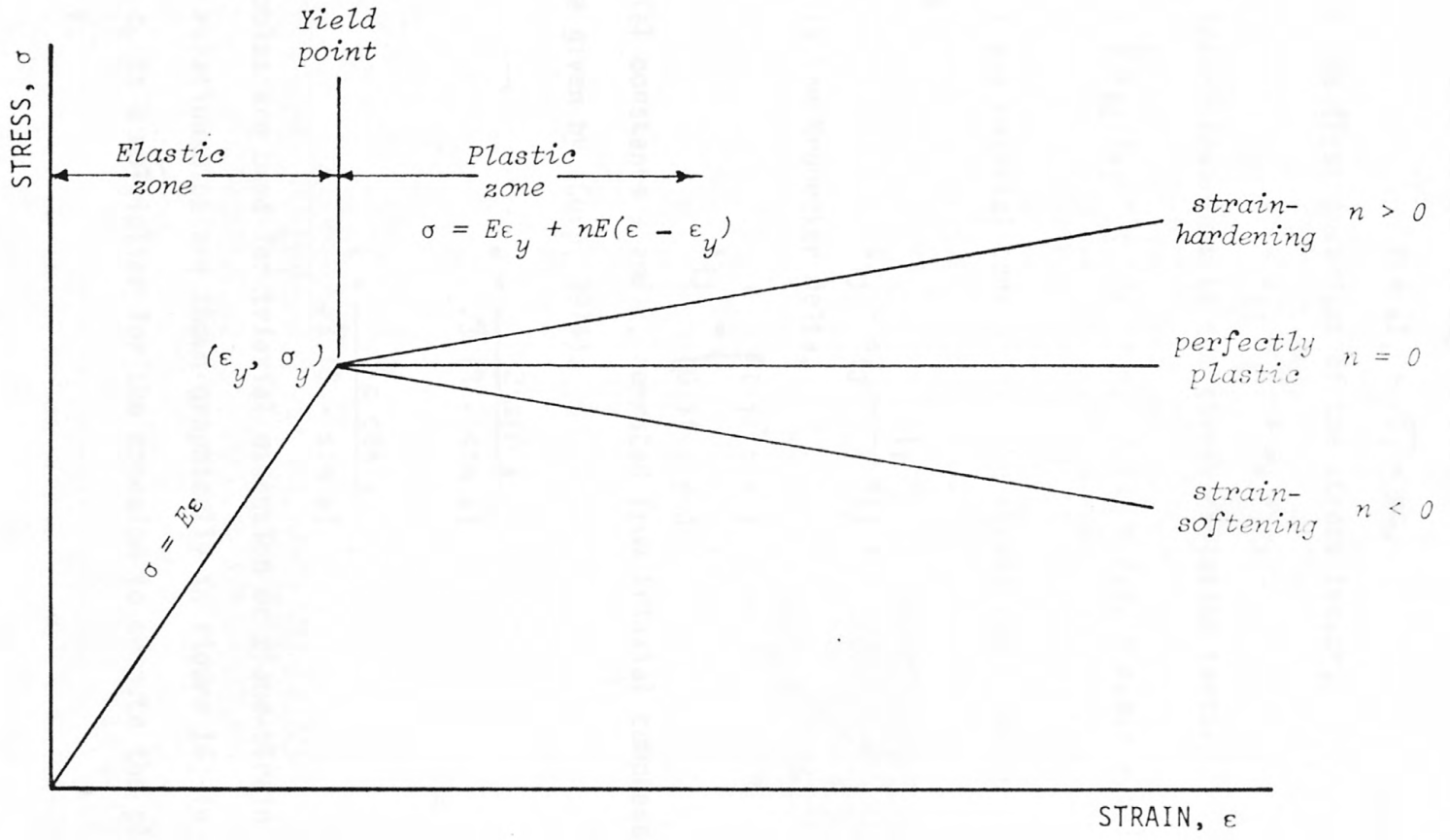

Figure 15. Idealized stress-strain curve for an elastic-plastic material.

The Drucker-Prager criterion may be stated as

$$Y = \alpha I_1 + \sqrt{J_2} = k \ , \tag{8}$$

where I_1 is the first invariant of the stress tensor,

$$I_1 = \sigma_{ii} = \sigma_1 + \sigma_2 + \sigma_3 \ , \tag{9}$$

J_2 is the second invariant of the stress deviation tensor

$$J_2 = \frac{1}{2} s_{ij} s_{ij} = \frac{1}{3} (\sigma_1^2 + \sigma_2^2 + \sigma_3^2 - \sigma_1\sigma_2 - \sigma_2\sigma_3 - \sigma_1\sigma_3) \ , \tag{10}$$

and α and k are material constants. The stress deviation tensor is defined as

$$s_{ij} = \sigma_{ij} - \frac{I_1}{3} \delta_{ij} \ , \tag{11}$$

where δ_{ij} is the Kronecker delta,

$$\delta_{ij} = \begin{cases} 1 \text{ if } i = j \\ 0 \text{ if } i \neq j \end{cases} . \tag{12}$$

The material constants α and k, computed from triaxial compression tests, are given by (Corp, 1974):

$$\alpha = \frac{2 \sin \phi}{\sqrt{3} (3 - \sin \phi)} \tag{13}$$

and

$$k = \frac{6 c \cos \phi}{\sqrt{3} (3 - \sin \phi)} \ . \tag{14}$$

Other formulas are used for triaxial extension or plane-strain tests. The above relationships are shown graphically in Figure 16, in which the parameter c_k is a multiplier for the cohesion to compute the plasticity parameter k.

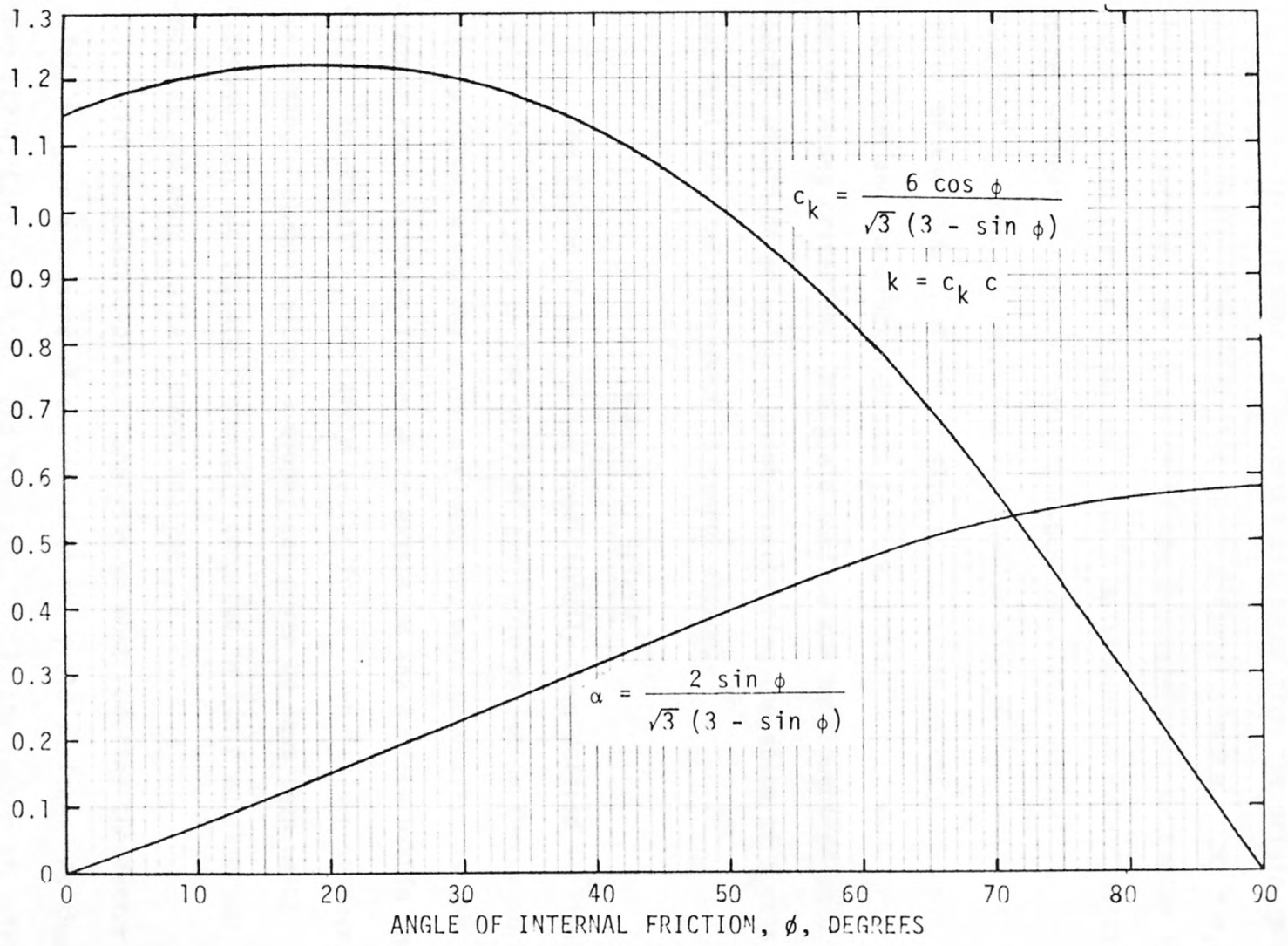

Figure 16. Graph for determining the Drucker-Prager material constants α and k from triaxial tests.

The yield surface for this criterion in principal stress space is a right circular cone, with vertex displaced from the origin, whose axis is the hydrostatic line (the space diagonal where $\sigma_1 = \sigma_2 = \sigma_3$), as shown in Figure 17. An advantage of the Drucker-Prager criterion is that the yield surface is mathematically continuous in principal stress space, whereas the conventional Mohr-Coulomb yield surface (an irregular hexagonal pyramid) is not. For the special case of zero cohesion the vertex of the cone is at the origin; for $\phi = 0$ the yield surface becomes a cylinder and the Drucker-Prager failure criterion becomes identical to the von Mises criterion. The yield surface can be thought of as a "cage," within or on which a point representing the state of stress in a body must lie, and from which it cannot escape.

Factor of Safety

The factor of safety has traditionally been defined in limit equilibrium analyses as the ratio of available resisting forces to the driving forces along any given surface, or, more generally, as the minimum ratio of those forces which exists on any surface within the slope. In actuality, the safety factor for a given failure surface, or for a single element within a slope, can never be less than unity, although such factors are frequently computed in limit equilibrium analyses and many finite element analyses.

For an elastic-plastic analysis we must redefine the factor of safety to give a measure of closeness to the yield surface. As shown by Corp (1974; Corp, Schuster, and McDonald, 1975), the factor of safety using the Drucker-Prager criterion may be expressed as

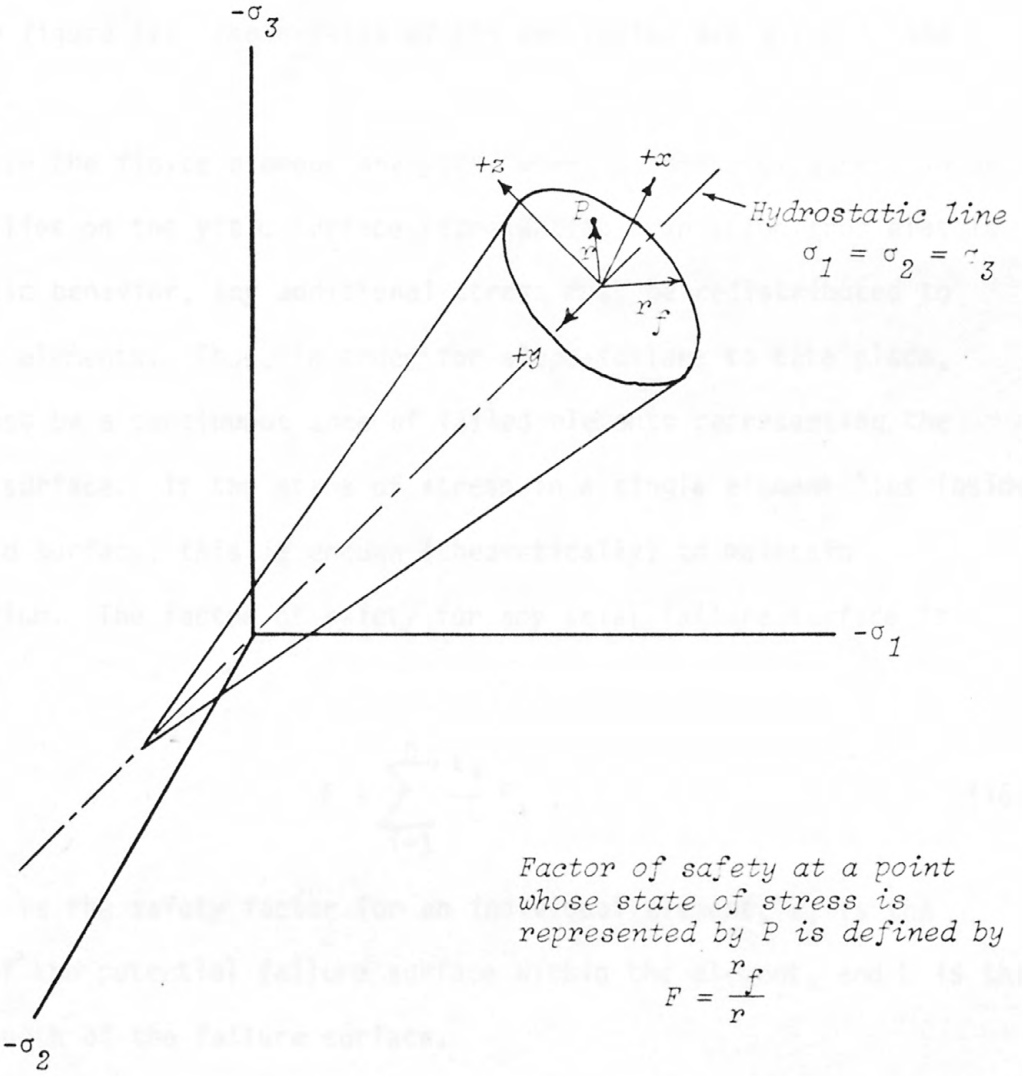

Figure 17. Drucker-Prager yield criterion in principal stress space.

$$F = \frac{r_f}{r} = \frac{k - \alpha I_1}{\sqrt{J_2}} \, . \qquad (15)$$

This expression relates the strength available (the radius of the yield surface cone) to the strength mobilized (the distance of the point representing the actual stress state from the hydrostatic line), as shown in figure 17. The details of the derivation are given in the Appendix.

In the finite element analysis, when the state of stress in an element lies on the yield surface representing transition from elastic to plastic behavior, any additional stress must be redistributed to adjacent elements. Thus, in order for slope failure to take place, there must be a continuous zone of failed elements representing the failure surface. If the state of stress in a single element lies inside the yield surface, this is enough (theoretically) to maintain equilibrium. The factor of safety for any trial failure surface is given by

$$F = \sum_{i=1}^{n} \frac{\ell_i}{L} F_i \, , \qquad (16)$$

where F_i is the safety factor for an individual element, ℓ_i is the length of the potential failure surface within the element, and L is the total length of the failure surface.

This definition differs from that in limit equilibrium analyses, where the safety factor is the average of resisting to driving forces over the entire surface and no provision is made for stress

redistribution once the maximum strength is mobilized in a zone within the slope.

It has been stated that the safety factor in any element cannot be less than unity. As a practical matter of computation, however, safety factors of less than one will frequently be encountered as stress increments are applied to an element. The amount of excess stress (the distance by which the state of stress lies outside the yield surface) that is allowed to exist in an element without being redistributed can be limited by the computer program to any desired value. In selecting this value one must strike a compromise between theoretical accuracy and the amount of computer time required for the solution to converge, keeping in mind the uncertainty in the properties of the materials and the inhomogeneities that exist in any natural system.

HIDDEN WATER MINE SLIDE

Aerial Photographic Interpretation of Slide Area

Although the exact history of the site is not known, the area has been photographed at frequent intervals from 1954 to the present. The area of the slide is in the last section of the mine to be excavated, as is seen by comparison of the photographs taken in 1954 and 1967 (Figs. 18 and 19). From the 1954 photographs we can estimate that the mine was abandoned in late 1955. The 1954 photographs also show that the spoil pile was dumped on ground sloping toward the excavation.

Two small slope failures (debris flows?) at the head of the valley can be seen on the 1967 photographs (Fig. 19) and do not appear to have changed much through April of 1978. The date of the major slide is determined to be between October 2, 1974 and June 20, 1975 by interpreting air photographs (Figs. 20 and 21). It is most likely that the slide occurred about April 1975, following the spring thaw.

Slide Monitoring

In June 1977 a survey network consisting of a 32-m baseline and 10 movement-monitoring targets was established at the Hidden Water slide. The baseline was established on the top of the section of highwall opposite the slide. Survey targets consisted of 76-mm-diameter red plastic highway-type reflectors bolted to 0.75-m lengths of steel tomato stakes. A white cross of 3-mm-wide automobile decorating tape served as the sighting point for theodolite measurements. These

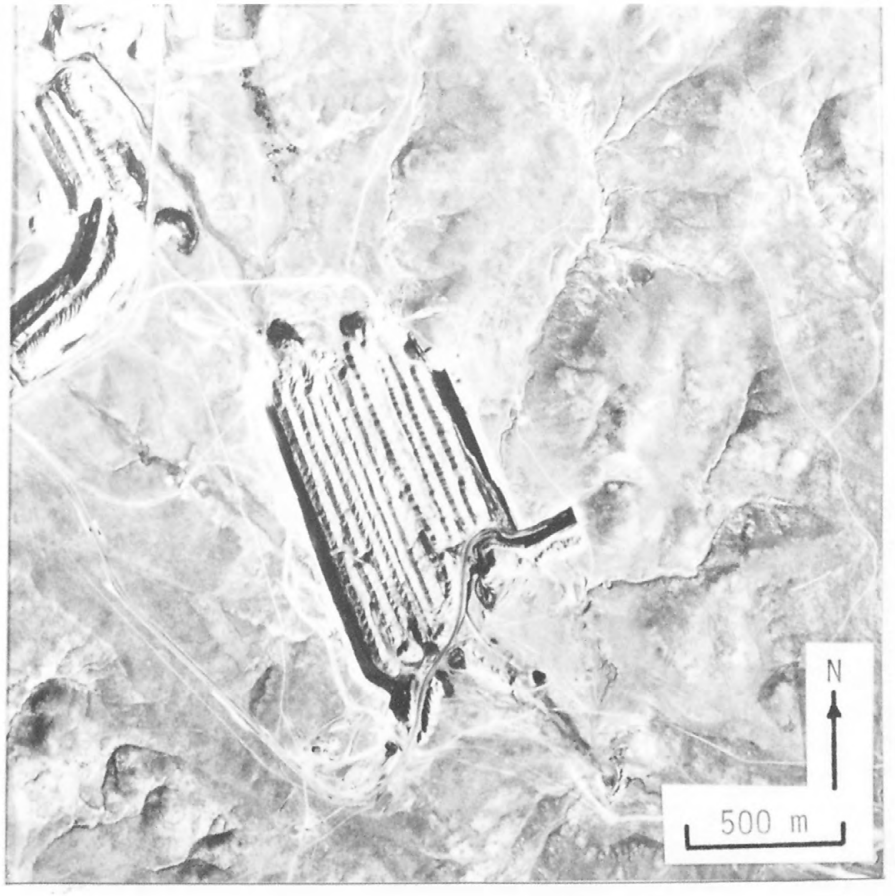

Figure 18. Air photograph of Hidden Water mine taken in 1954.

Soil Conservation Service photograph BBP-10N-147, August 24, 1954.

Figure 19. Air photograph of Hidden Water mine taken in 1967.

Soil Conservation Service photograph BBP-2HH-65, September 8, 1967. < points to location of present slide.

Figure 20. Air photograph of Hidden Water mine taken in 1974.

U. S. Geological Survey photograph by R. D. Miller, October 2, 1974. < points to location of present slide.

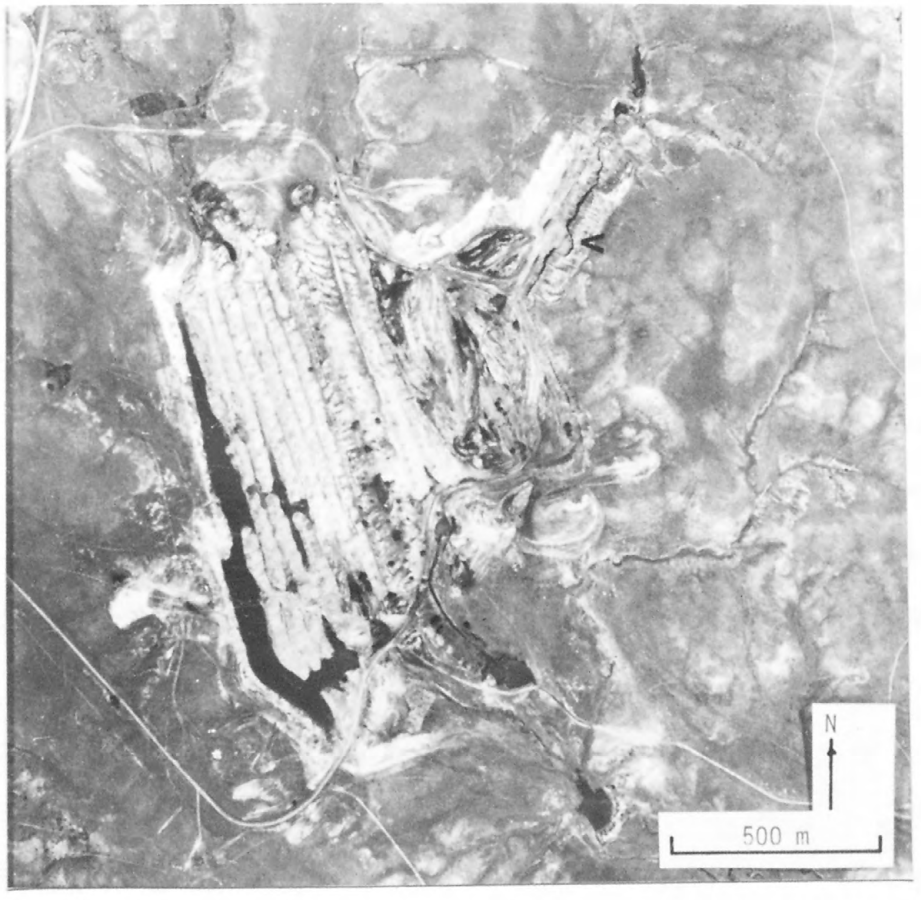

Figure 21. Air photograph of Hidden Water mine taken in 1975.

Photograph by IntraSearch, Inc., Denver, Colo., 2813-60, June 20, 1975. < points to location of slide.

movement targets were located on and around the slide, as shown in Figure 22.

Coordinates of the targets were determined by measuring both horizontal and vertical angles with a Wild T-2 one-second theodolite from each end of the baseline. An arbitrary coordinate system was established with origin at $\Delta 2$, the x-axis in the direction from $\Delta 2$ to $\Delta 1$, the y-axis toward the slide, and with an assumed elevation for $\Delta 1$ of 1000.000 m (the actual elevation is about 1230 m). On the initial survey and the first resurvey an electronic distance measuring (EDM) device was also used to determine the coordinates of the survey points. However, there was poor agreement between the lengths of the sides reduced from the EDM measurements and those computed from the triangulation. The differences (about 30 to 50 mm) may have been due to the inherent error of the instrument at close range, the quality of the reflectors, and the fact that the reflectors were not pointed directly at the instrument. Because vertical angle measurements were required for elevation determination anyway, and because it was felt that the triangulation was more accurate than the EDM measurements, it was decided to abandon the use of the EDM in favor of the triangulation in order to save field time and the inconvenience and hazard of shipping the EDM back and forth by air.

Movement of the slide was monitored from June 1977 to May 1978. The record of movement of the survey points is given in Table 4. The maximum y-movement of any surveyed point between June and September 1977 was 126 mm. Between September 1977 and April 1978, the winter snowfall and spring thaw produced additional movements of up to 372 mm.

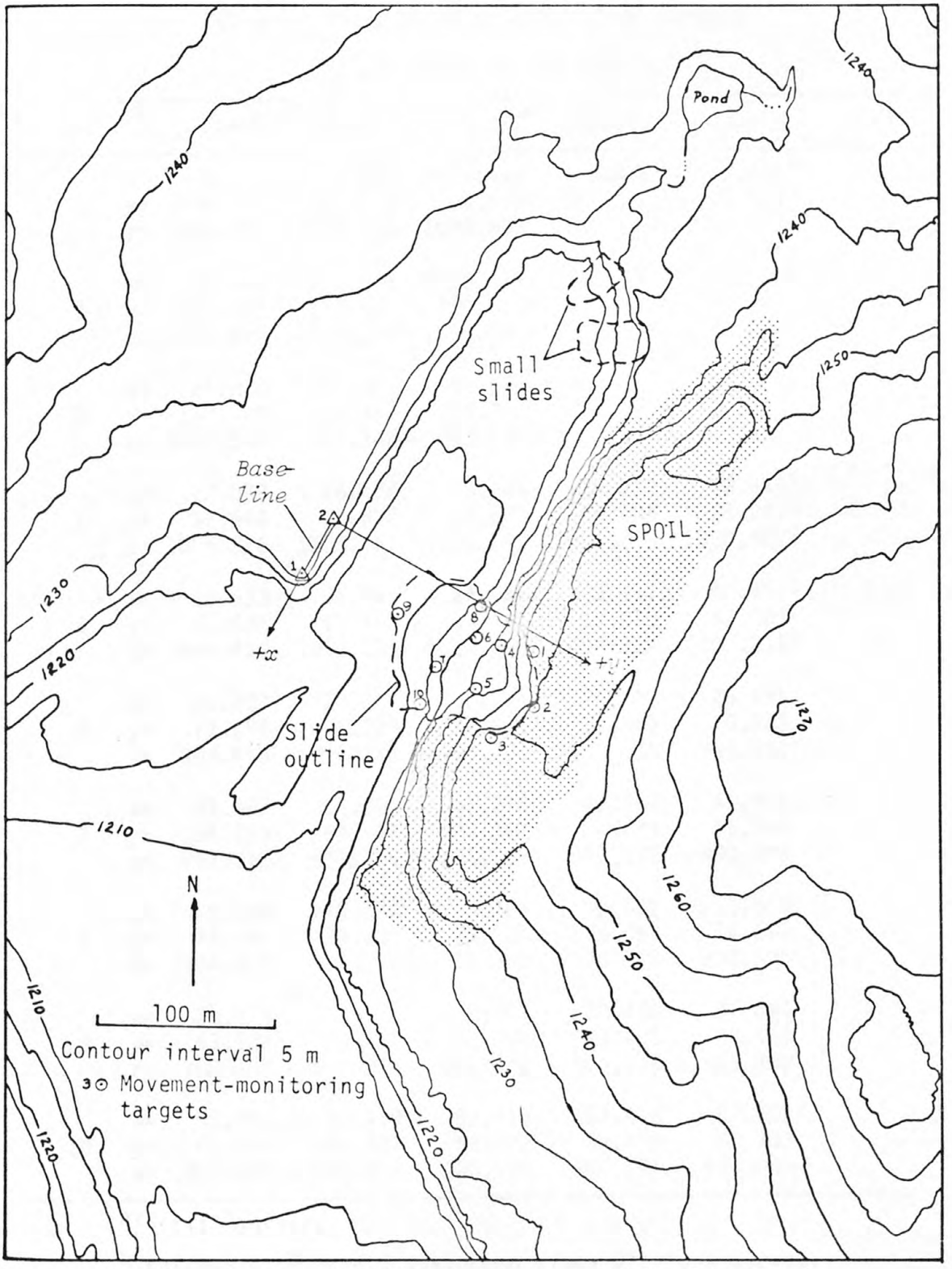

Figure 22. Map of part of Hidden Water mine showing layout of survey net. Compiled from air photographs taken in 1975.

Table 4. Results of triangulation surveys

[Coordinates in meters]

Sta.		9Jun77[a]	10Aug77	19Sep77	25Apr78	26May78
1	x=	6.446	6.448	6.436	6.406[b]	6.431[b]
	y=	104.623	104.630	104.619	104.542[b]	104.503[b]
	z=	1018.707	1018.702	1018.693	1018.673[b]	1018.651[b]
2	x=	33.640	33.643	33.629	33.662[b]	33.630[b]
	y=	120.493	120.500	120.511	120.501[b]	120.581[b]
	z=	1020.270	1020.270	1020.268	1020.272[b]	1020.249[b]
3	x=	61.878	61.883	61.874	61.863[b]	61.921[b]
	y=	110.328	110.347	110.361	110.306[b]	110.313[b]
	z=	1018.347	1018.342	1018.336	1018.334[b]	1018.328[b]
4	x=	18.072	18.106	18.101	18.113	18.542[c]
	y=	92.644	92.633	92.627	92.404	86.247[c]
	z=	1005.226	1005.161	1005.141	1004.975	1000.602[c]
5	x=	38.933	38.955	38.947	39.021	40.485[c]
	y=	91.538	91.460	91.447	91.075	84.003[c]
	z=	1004.430	1004.390	1004.380	1004.254	1000.218[c]
6	x=	26.309	26.315	26.299	26.283	25.651
	y=	77.296	77.223	77.170	76.888	70.406
	z=	998.275	998.222	998.202	998.086	994.631
7	x=	41.387	41.385	41.378	41.369	41.496
	y=	64.825	64.747	64.747	64.629	61.295
	z=	992.212	992.194	992.188	992.172	990.998
8	x=	0.769	0.777	0.766	0.751	0.663
	y=	75.144	75.135	75.131	75.063	74.591
	z=	994.924	994.906	994.900	994.898	994.695
9	x=	30.474	30.476	30.472	30.498	31.695
	y=	43.502	43.488	43.494	43.405	39.493
	z=	988.956	988.954	988.952	988.974	989.308
10	x=	57.418	57.419	57.416	57.418	57.607
	y=	62.503	62.507	62.522	62.499	62.303
	z=	990.208	990.199	990.196	990.201	990.038

[a]Initial survey.

[b]Stations 1, 2, and 3 disturbed since previous survey.

[c]Stations obviously displaced and disoriented as a result of slide activity.

On May 16-18, 1978, 96 mm of rain fell at Sheridan, Wyoming, bringing the total rainfall for the month to 153 mm and making it the wettest May since records began in 1935. The average monthly precipitation for May is 64 mm (data from National Oceanic and Atmospheric Administration records). These heavy rains caused widespread flooding and reactivated several landslides, including the one at the Hidden Water mine. One survey point (#6) had a y-movement of 6.9 m since the previous survey a month earlier. The point near the center of the toe (#9) experienced an outward movement of 3.9 m and an upward movement of 0.33 mm. This upward component of movement at the toe and the formation of a pressure ridge ahead of the toe are evidence that the failure surface involves the valley floor, a result predicted by the Spencer stability analysis.

Stability Analysis of the Hidden Water Mine Slide

Stability analyses of the Hidden Water mine slide were made utilizing two methods: the Spencer limiting equilibrium analysis and an elastic-plastic finite element analysis. The principles of both of these methods have been discussed earlier. Both methods involve idealizing the slope geometry into zones of uniform material properties, subject to certain geometrical restrictions. A cross section through the slide is shown in Figure 23. As a first approximation to the material properties of the Hidden Water site, properties of fresh, similar materials from the Decker mine, as described in the chapter on physical properties, will be used. The properties used in these analyses are given in Table 5. Because of the high degree of fracturing

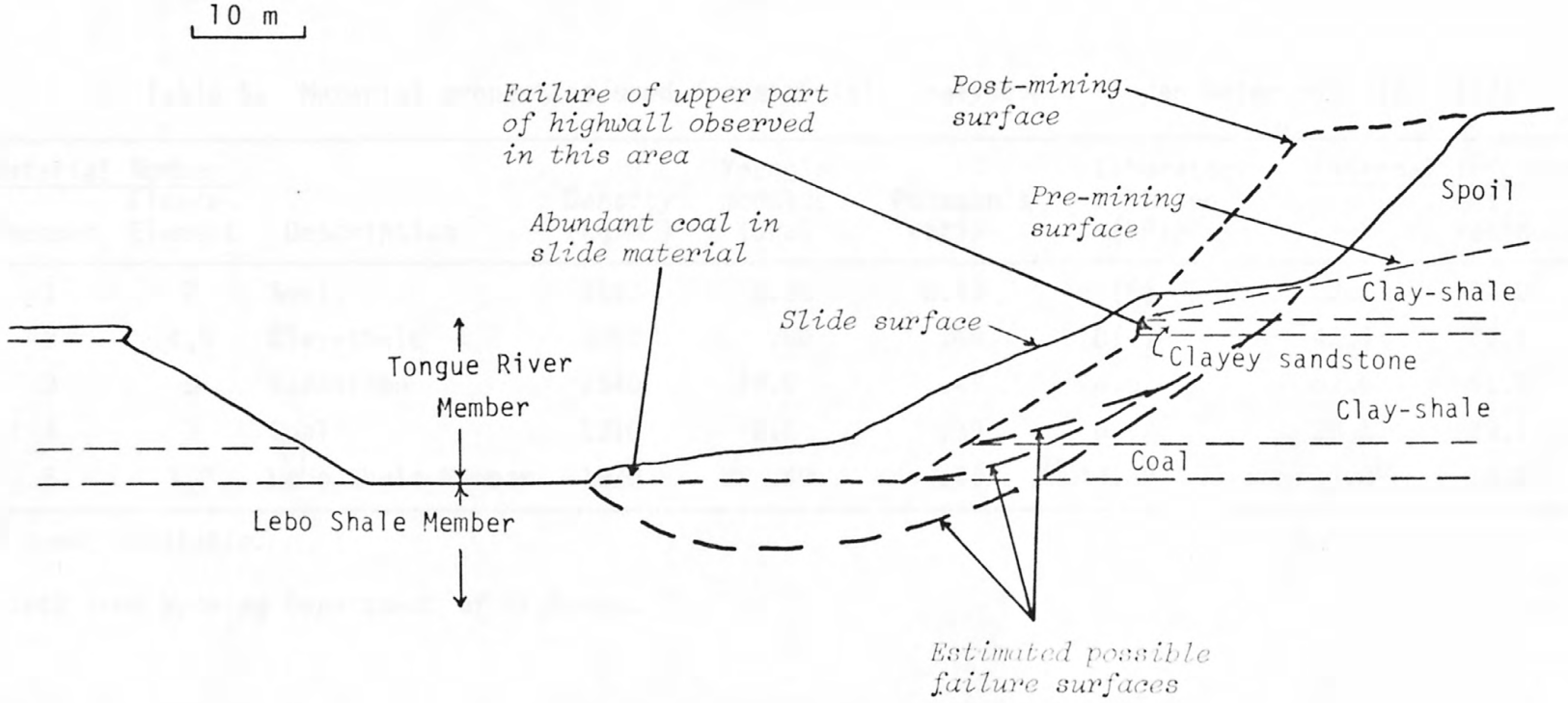

Figure 23. Cross section through Hidden Water mine landslide.

Table 5. Material properties used for stability analyses of Hidden Water mine landslide.

Material Number							Internal friction (degrees)	
Spencer	Finite Element	Description	Density (kg/m^3)	Young's modulus (GPa)	Poisson's ratio	Laboratory cohesion (kPa)	peak	residual
1	7	Spoil	1840	0.35	0.40	([a])	22.0	22.0
2	4,6	Clay-shale	2350	.50	.49	0(-)	42.5	36.9
3	5	Sandstone	2640	10.0	.49	4.5	61.6	51.8
4	3	Coal	1310	2.0	.39	6.9	29.1	29.1
5	1,2	Lebo Shale Member	1920	.40	.49	13.8[b]	14.0[b]	14.0

[a] - not available.

[b]Data from Wyoming Department of Highways.

in the rock mass, the rock mass cohesion is assumed to be zero in all analyses.

Spencer Analysis

The idealized slope for the Spencer analysis is shown in Figure 24. Three potential failure surfaces were selected for analysis by extrapolating the visible scarp to the top of the coal bed, to the toe of the slope (the base of the coal bed), and through the mine floor to the toe of the slide material. Twelve analyses were run, representing the various combinations of failure surfaces with the water table at the bottom boundary of the problem and at the mine floor, and the peak and residual material properties. The results of these analyses are summarized in Table 6.

An attempt was made to analyze the slope at the Hidden Water mine by the Morgenstern-Price method, but seven different assumptions of the f(x) distribution failed to produce an acceptable solution according to the criteria mentioned earlier. A computer program for Spencer's analysis (SLOPE8R, Univ of Calif., Berkeley) was obtained, and while it had the advantage of being able to use any consistent set of units (metric or English), this particular program was limited to two layers of different materials. However, as shown by Wright (1969, p.56), the Morgenstern-Price and Spencer methods are equivalent if the f(x) distribution is constant. It was therefore decided to analyze the slope by Spencer's method using the available Morgenstern-Price computer program with f(x) = 1 throughout. The program used for the analyses presented here was written by N. R. Morgenstern of the University of

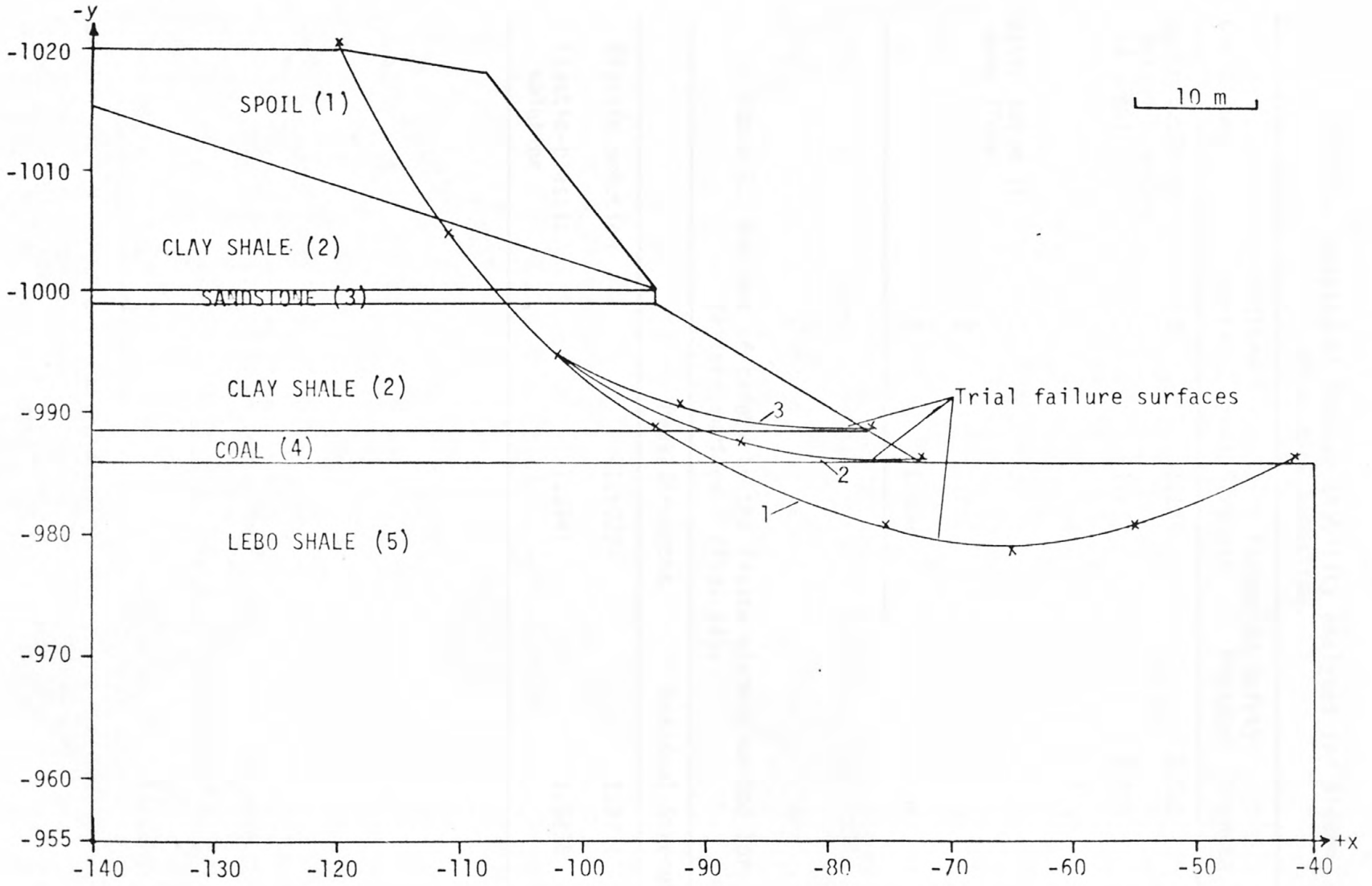

Figure 24. Idealized slope at Hidden Water mine used for Spencer stability analyses.

Table 6. Results of Spencer stability analyses for Hidden Water mine landslide.

Condition	Failure Surface	Factor of Safety Peak Strength	Residual Strength
Water table at bottom boundary of problem	1	1.189	1.061
	2	1.262	1.089
	3	1.506	1.234
Water table at mine floor	1	1.082	.954
	2	1.262	1.089
	3	1.506	1.234

Table 7. Factors of safety by the finite element method for failure surface 1 (Fig. 24).

	Peak Strengths	Residual Strengths
Elastic solution	1.5027	1.3931
Elastic-plastic solution	1.0941	1.0238

Alberta, modified at the U.S. Army Waterways Experiment Station, Vicksburg, Miss., further modified for the University of Arizona CDC 6400, and finally converted for use on the U.S. Geological Survey Honeywell Multics computers. This program requires units to be in pounds and feet and combinations thereof.

After running an elastic finite element analysis, new values of f(x) were computed by taking the ratio of the vertical shear stress to the horizontal stress for the elements in which the points defining the failure surfaces were located. The Morgenstern-Price program was re-run using this new f(x) distribution. This resulted in an acceptable position for the line of thrust in every case, but many of the interslice factors of safety were still less than one. In no case, however, did the safety factor computed with the revised f(x) distribution differ from that given by the Spencer method (f(x) = 1) by as much as 0.02, and for the critical failure surface with water table at the mine floor the differences were 0.006 for peak strengths and 0.002 for residual strengths. The conclusion is that the Spencer analysis gives factors of safety as good as those given by the Morgenstern-Price analysis, and with much less effort.

Finite Element Analysis

The highwall at the Hidden Water mine was also analyzed by the finite element method. The idealized slope and finite element grid showing the boundary conditions used in these analyses is shown in Figure 25. The grid was generated by a modified version of MESHGEN (Egeberg, 1969). The finite element program used is a version of the

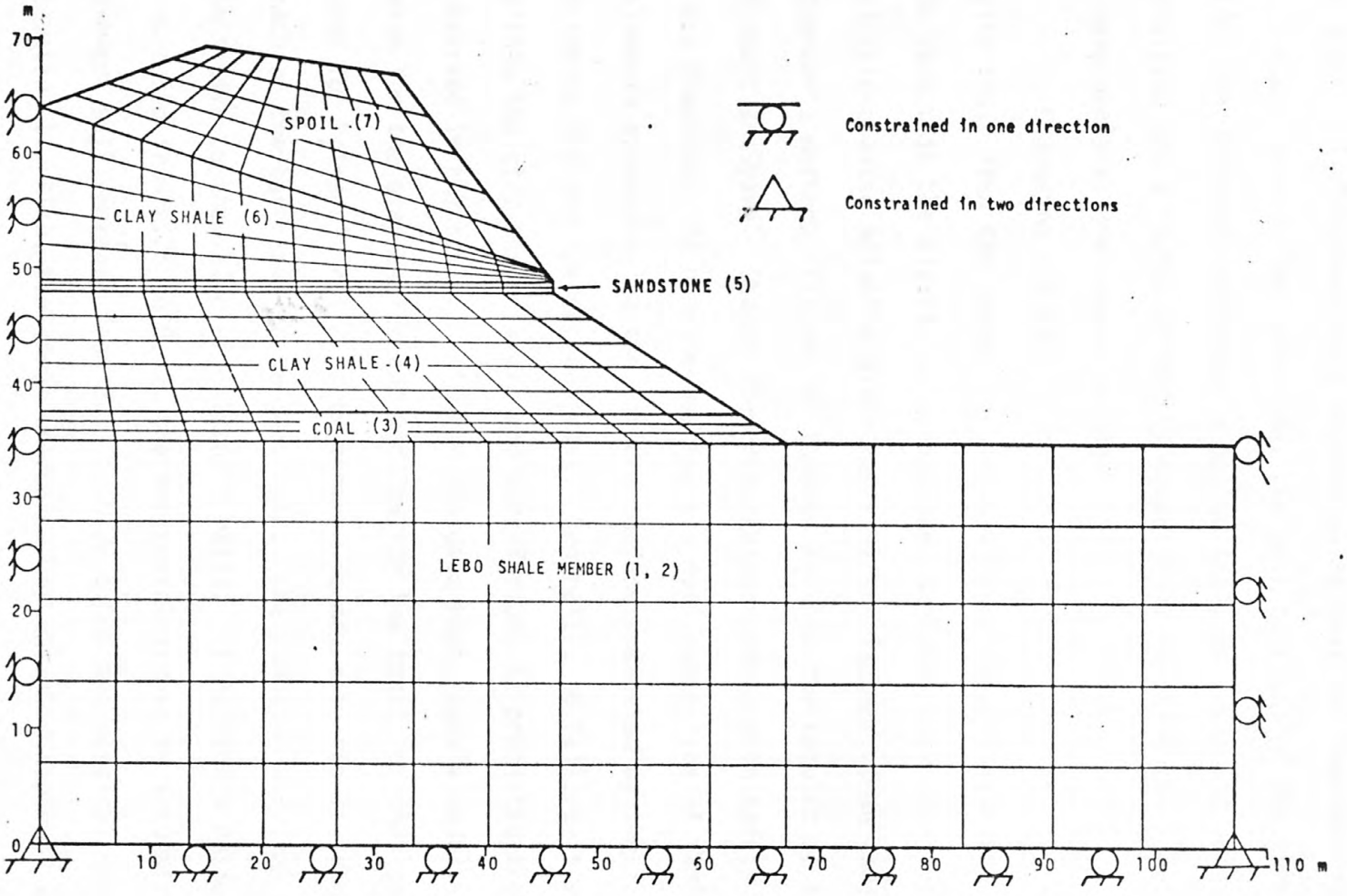

Figure 25. Finite element grid used in stability analysis of Hidden Water mine landslide, showing boundary conditions.

elastic-plastic code NONLIN (Baligh, 1973). The slope was analyzed by elastic and elastic-plastic methods using peak and residual strengths for each method. For each case, the most critical of the three failure surfaces analyzed by Spencer's method (failure surface 1, Fig. 24) was analyzed and a factor of safety computed by equation 16. The results of these analyses are summarized in Table 7.

Comparing the factors of safety from the finite element analysis with those from the Spencer analysis without seepage (Table 6), it can be seen that the elastic solution gives higher safety factors, and the elastic-plastic solution gives lower safety factors, than those given by Spencer's method. Figures 26 through 29 show the results of the finite element analyses. Shaded elements indicate those with safety factors less than one. In no case was there a continuous line of failed elements approximating the failure surface indicated by the field evidence and the Spencer analysis. Generally, no failure is predicted within the clay shale layers and more failure is predicted than is observed in the spoil. This may indicate that Young's modulus is too high for the clay shales and too low for the spoil, or that the value used for Poisson's ratio is in error. It may also result from assuming each of the materials to be isotropic. The computed stresses are quite sensitive to the value of Poisson's ratio. If Poisson's ratio is increased from 0.25 to 0.49, the horizontal stress in a constrained element will increase from 0.33 to 0.96 times the vertical stress, by equation 1. Also, the error introduced by assuming isotropy would be greater for thin-bedded sedimentary rocks than for more massive rocks such as granite.

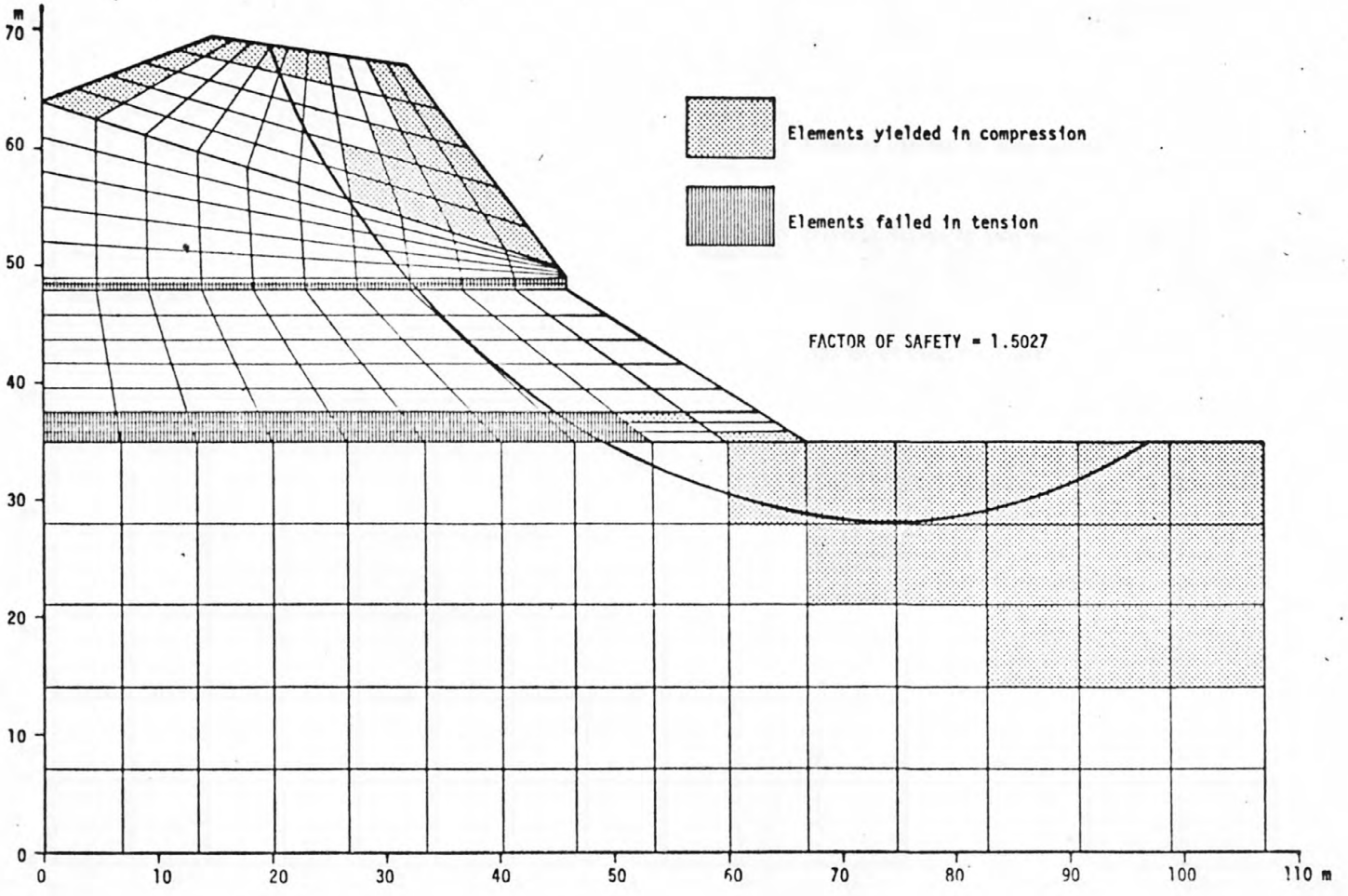

Figure 26. Results of linear elastic finite element analysis of Hidden Water mine landslide, peak strengths.

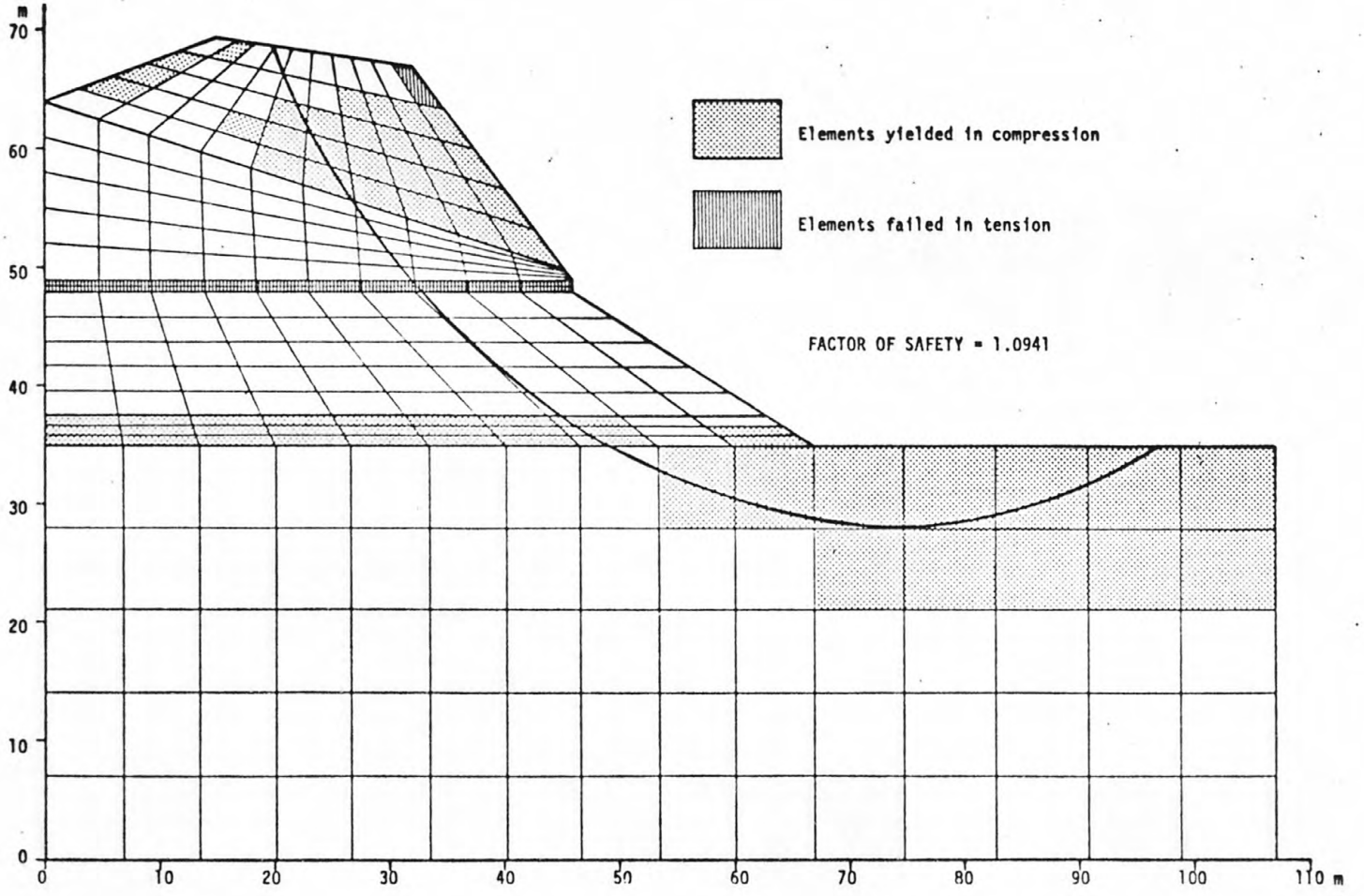

Figure 27. Results of elastic-plastic finite element analysis of Hidden Water mine landslide, peak strengths.

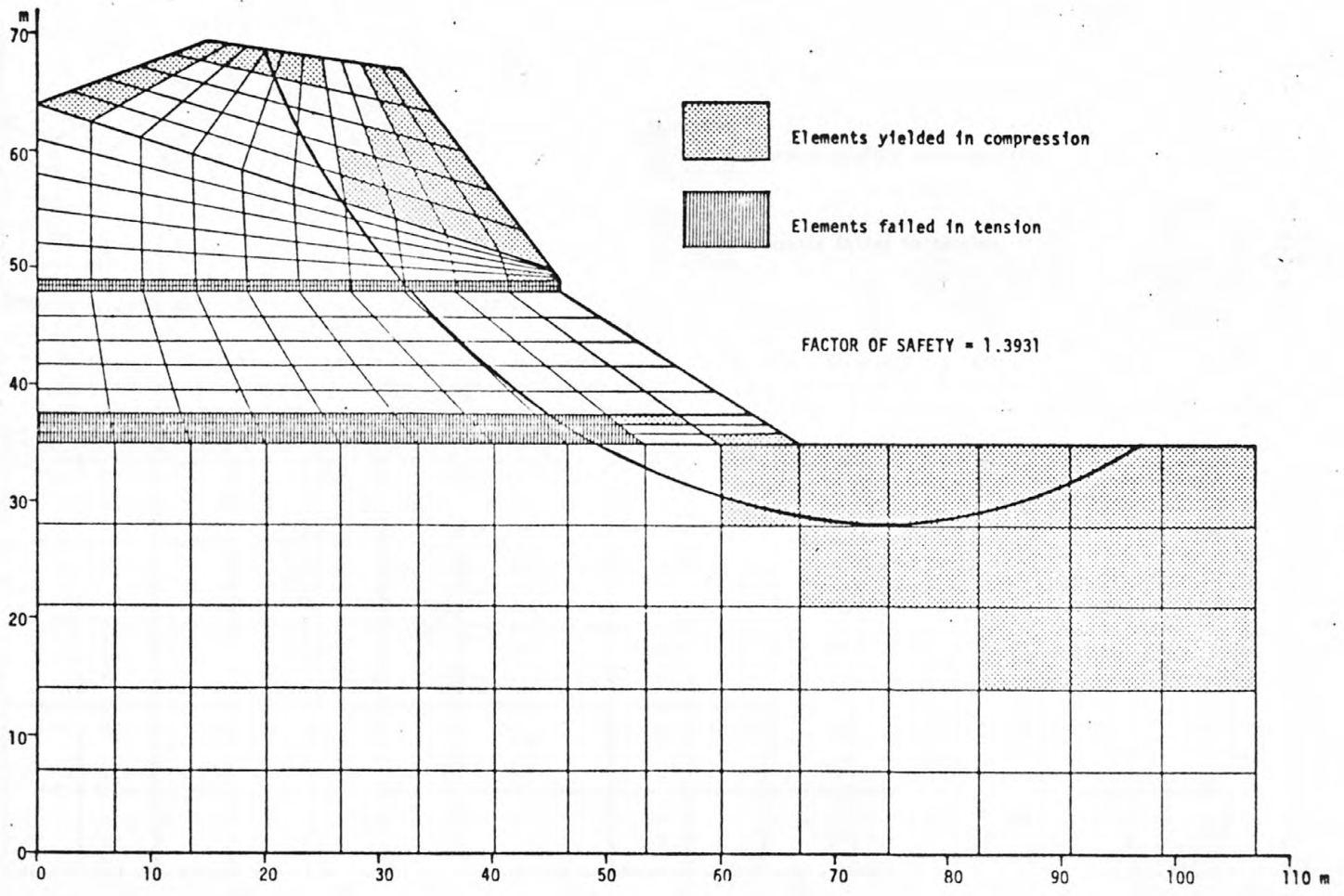

Figure 28. Results of linear elastic finite element analysis of Hidden Water mine landslide, residual strengths.

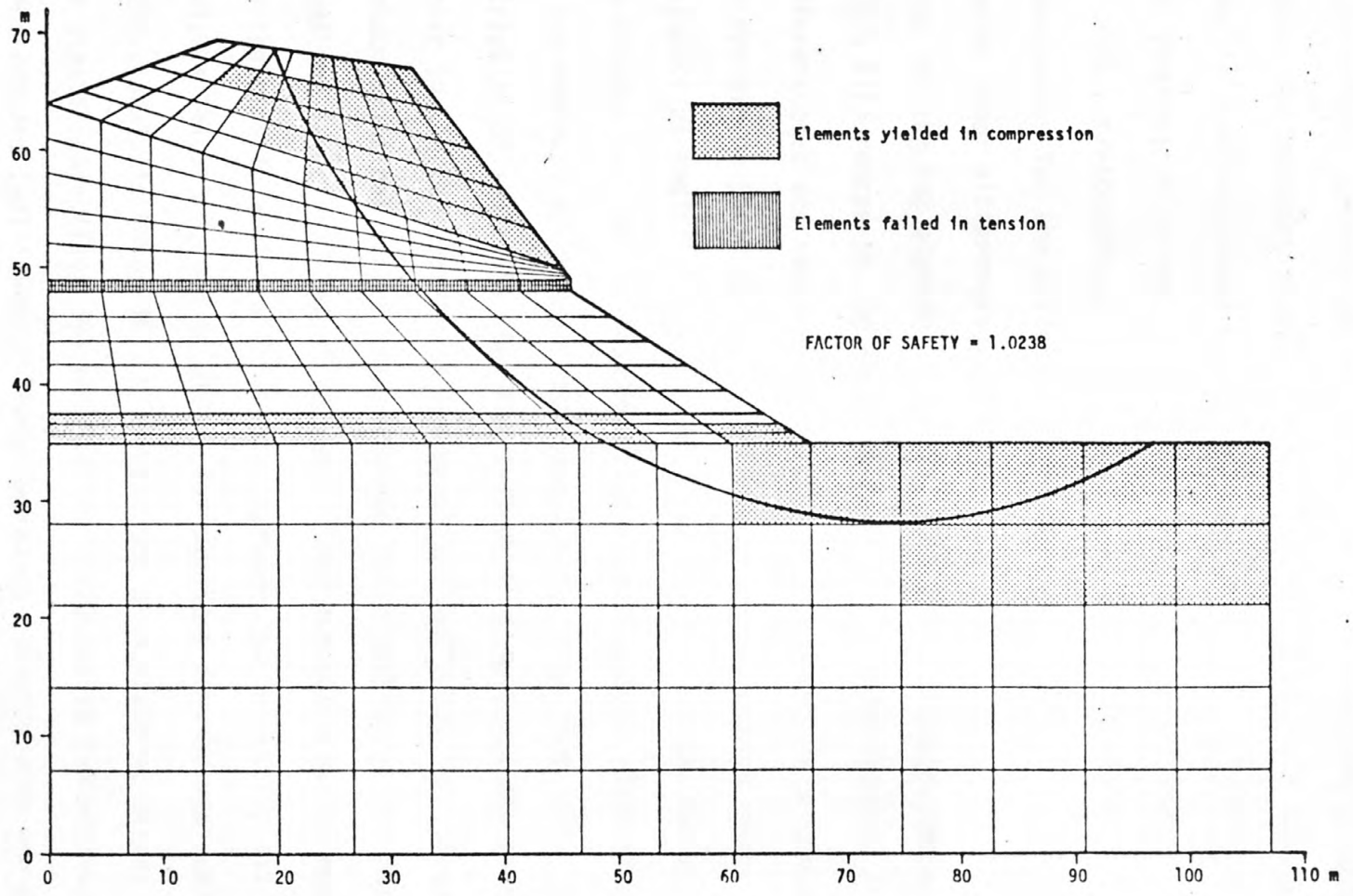

Figure 29. Results of elastic-plastic finite element analysis of Hidden Water mine landslide, residual strengths.

In addition, for each of the four cases analyzed, plots were made of the principal stress trajectories, expected shear failure trajectories, contours of the minimum (most compressive) principal stress, and contours of $\sqrt{J_2}$, a measure of the deviatoric stress. The shear failure trajectories were computed at angles of $(45°-\phi/2)$ to the most compressive stress. These plots are shown in Figures 30 through 41. The corresponding plots of principal stress and shear failure trajectories for the different cases appear very similar to each other, showing minor differences mainly near the boundaries. Corresponding plots for the two elastic cases are identical. Although there should be slight differences in the shear failure trajectories because of the different peak and residual ϕ angles, these are not large enough to be discernible on these plots. Examination of the expected shear failure trajectories indicates a failure surface similar to the one assumed, if the visible part of the failure surface is extended. This is best shown by the residual elastic-plastic case (dotted line, Fig. 35). This extrapolation indicates that the failure surface exits the base somewhat closer to the toe than the failure surface analyzed. The plots of minimum principal stress show a stress concentration at the base of the sandstone layer near the slope face. This concentration is much greater for the elastic analysis (Fig. 36) than the peak elastic-plastic analysis (Fig. 37), and is almost non-existent for the residual elastic-plastic analysis (Fig. 38). The contours of deviatoric stress ($\sqrt{J_2}$) for the elastic case (Fig. 39) show stress decreases in the vicinity of the sandstone and coal layers. These decreases coincide with the occurrence

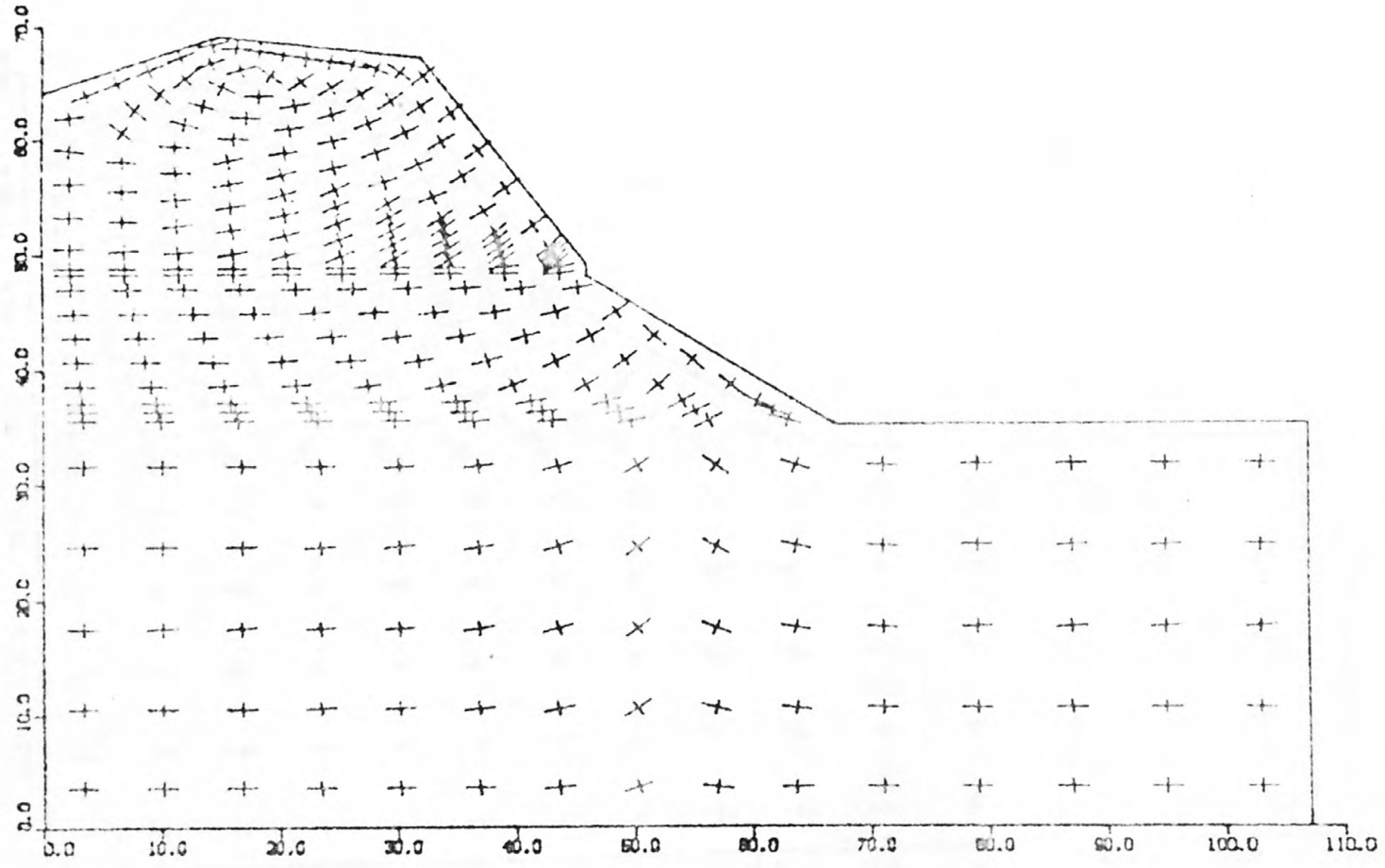

Figure 30. Principal stress trajectories, elastic analysis.

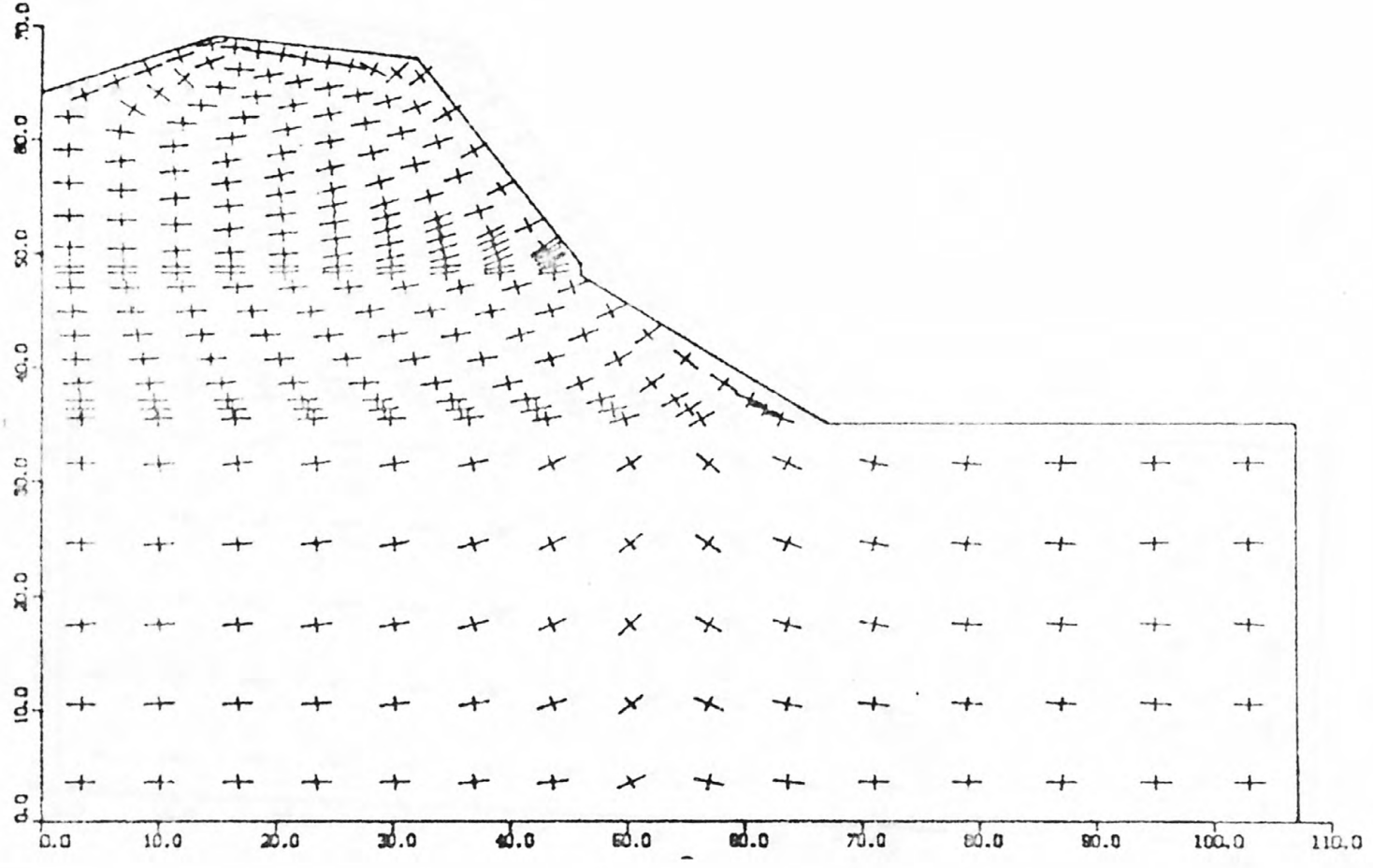

Figure 31. Principal stress trajectories, elastic-plastic analysis, peak strengths.

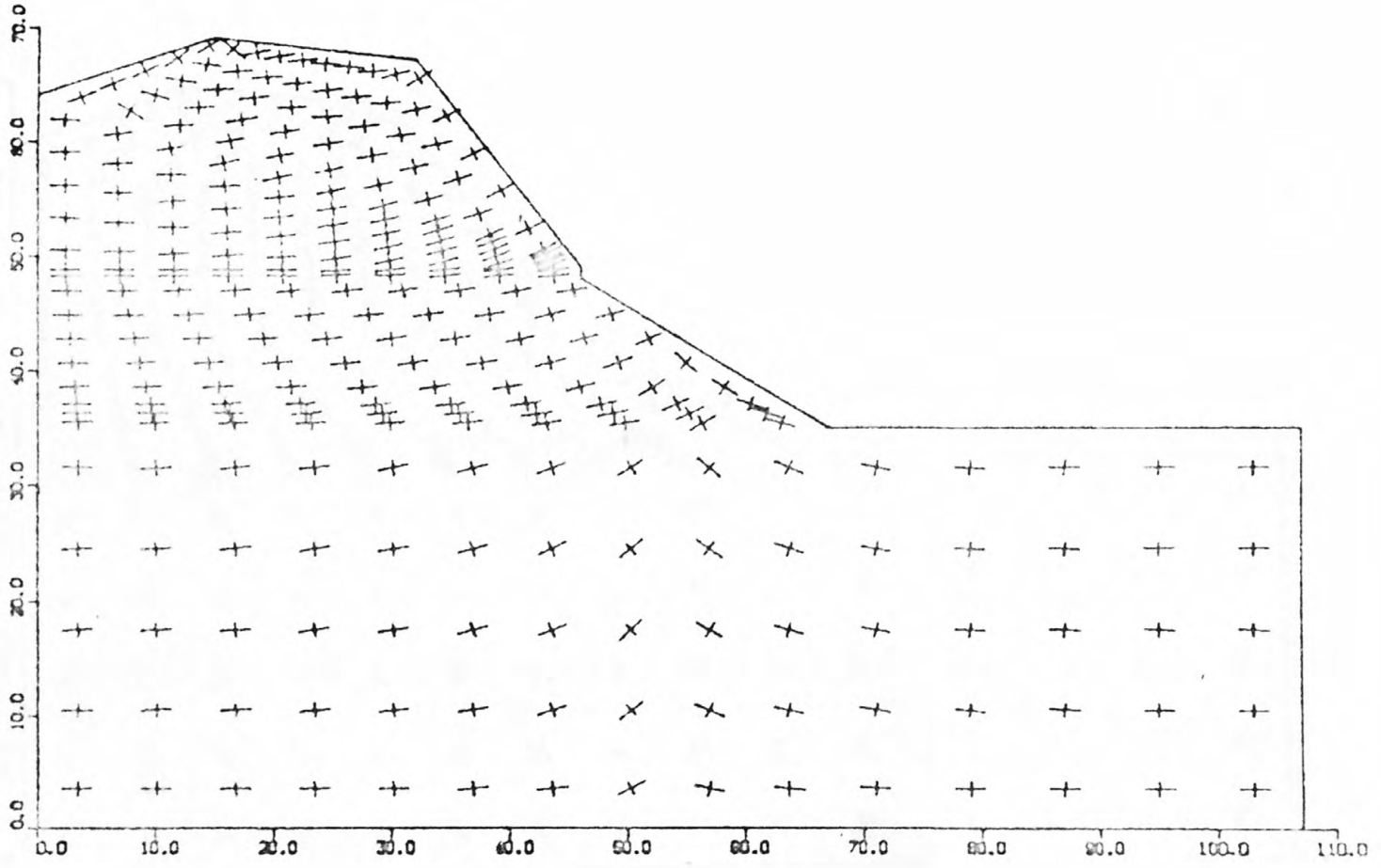

Figure 32. Principal stress trajectories, elastic-plastic analysis, residual strengths.

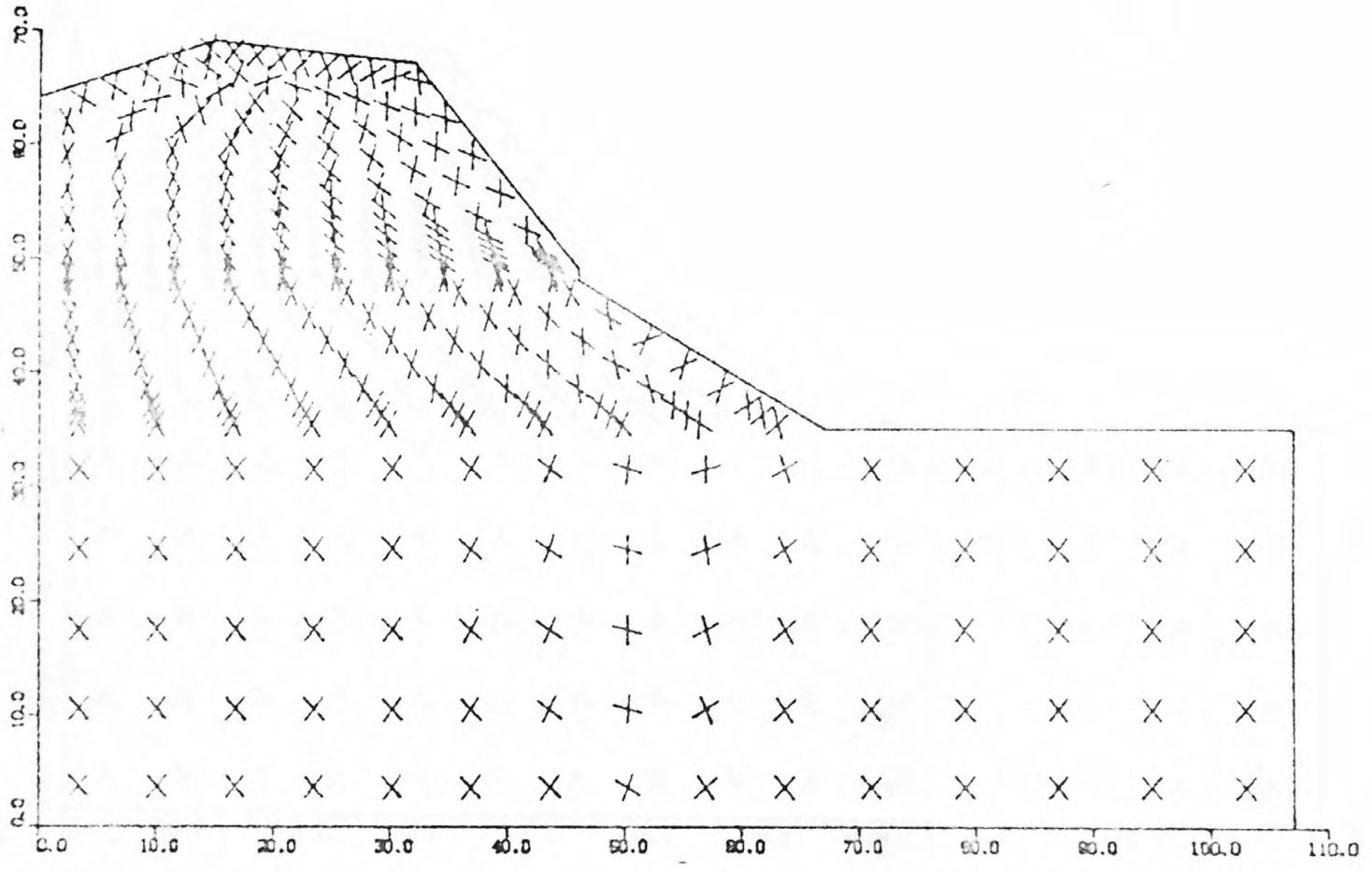

Figure 33. Expected shear failure trajectories, elastic analysis.

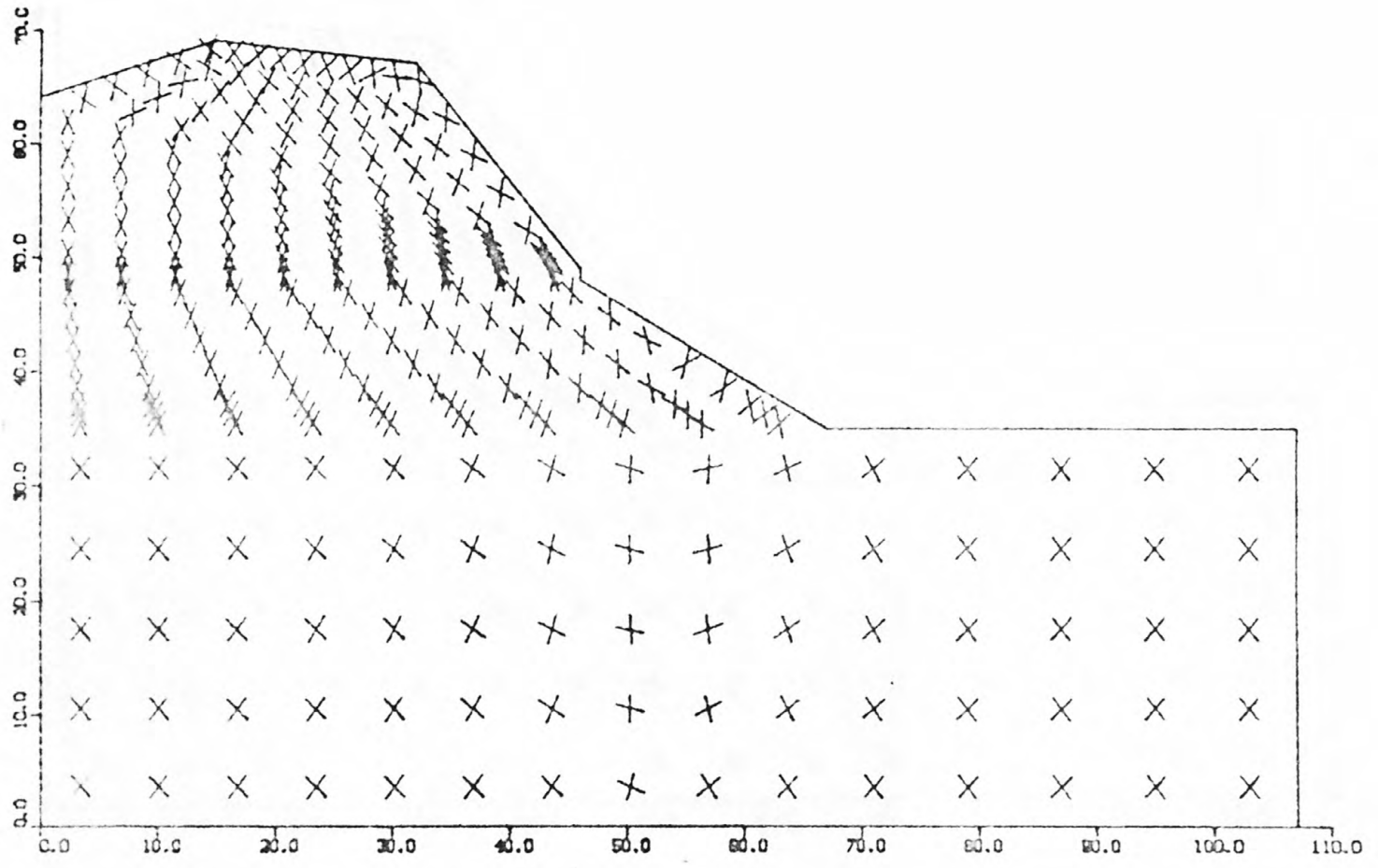

Figure 34. Expected shear failure trajectories, elastic-plastic analysis, peak strengths.

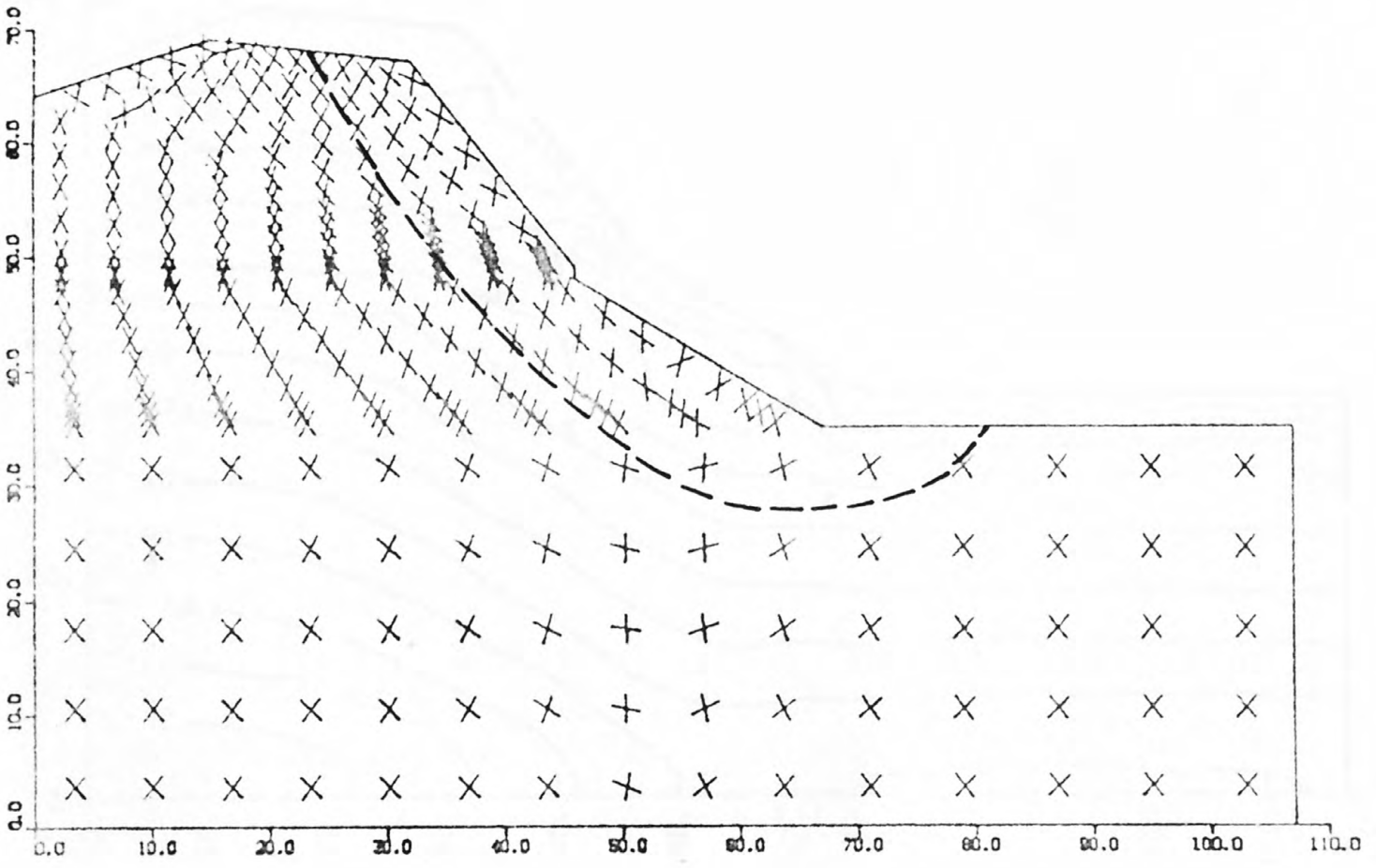

Figure 35. Expected shear failure trajectories, elastic-plastic analysis, residual strengths. Dashed line is extrapolation of visible part of failure surface.

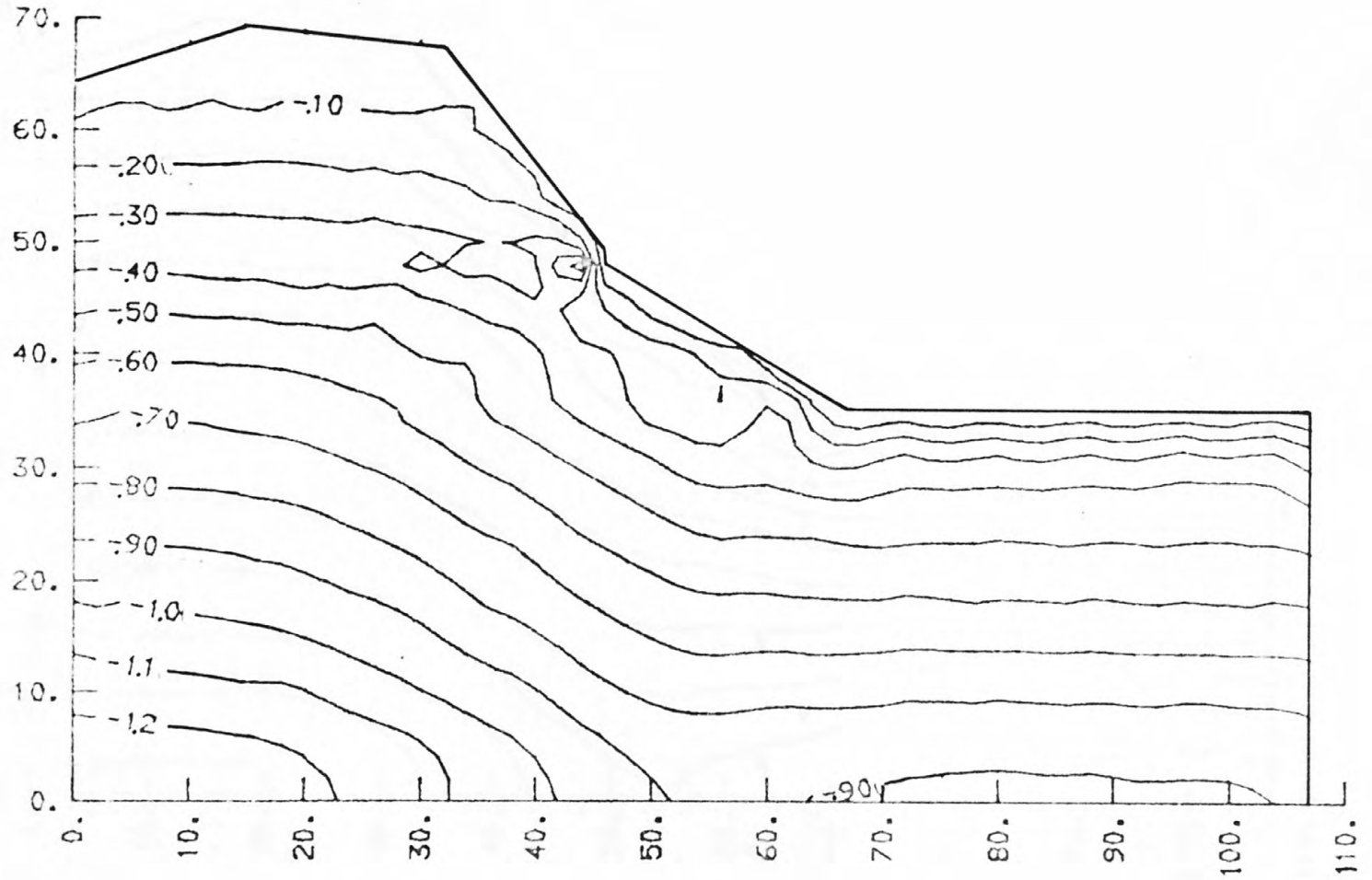

Figure 36. Contours of minimum principal stress, elastic analysis. Contour values are in MPa.

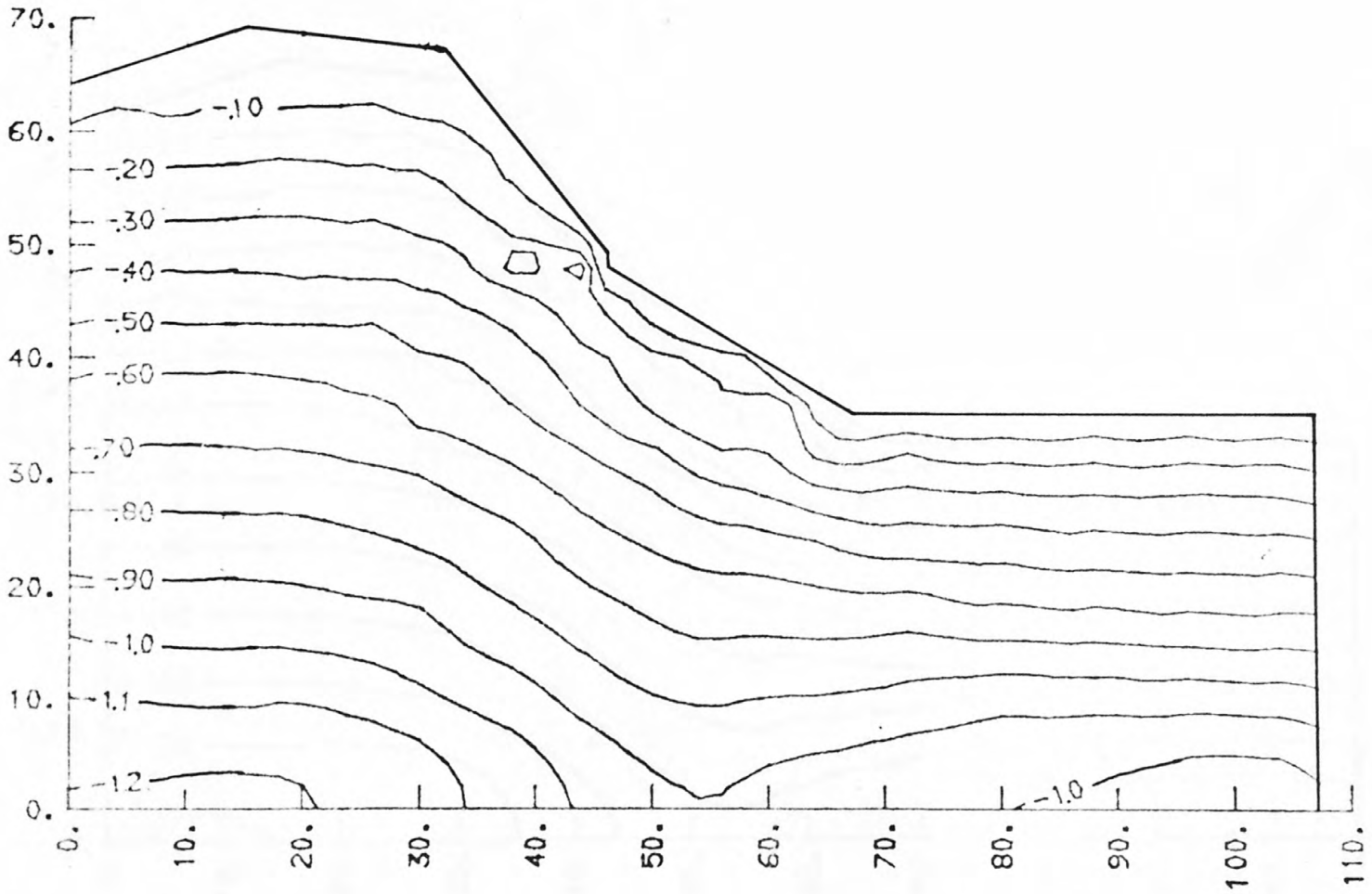

Figure 37. Contours of minimum principal stress, elastic-plastic analysis, peak strengths. Contour values are in MPa.

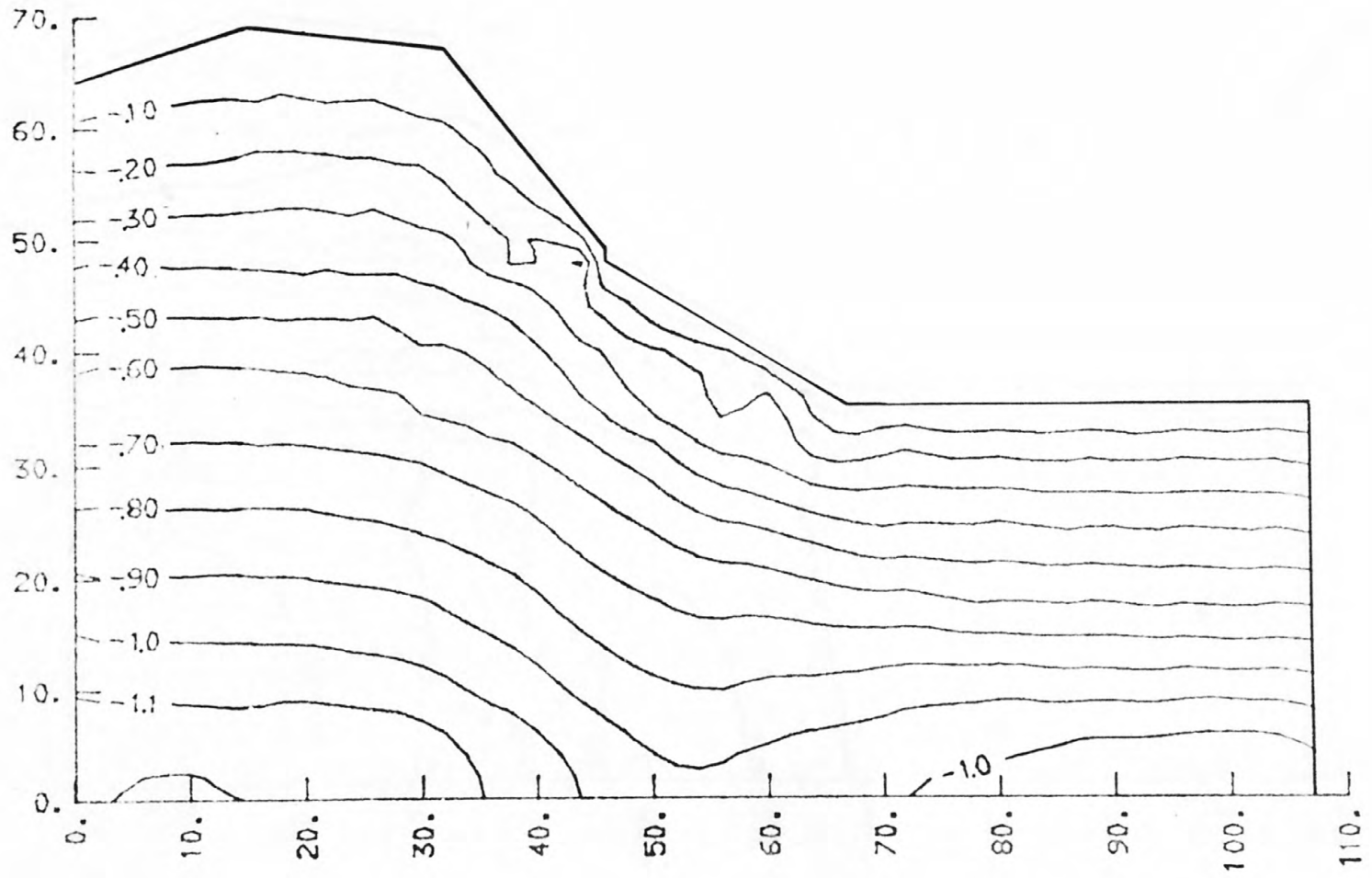

Figure 38. Contours of minimum principal stress, elastic-plastic analysis, residual strengths. Contour values are in MPa.

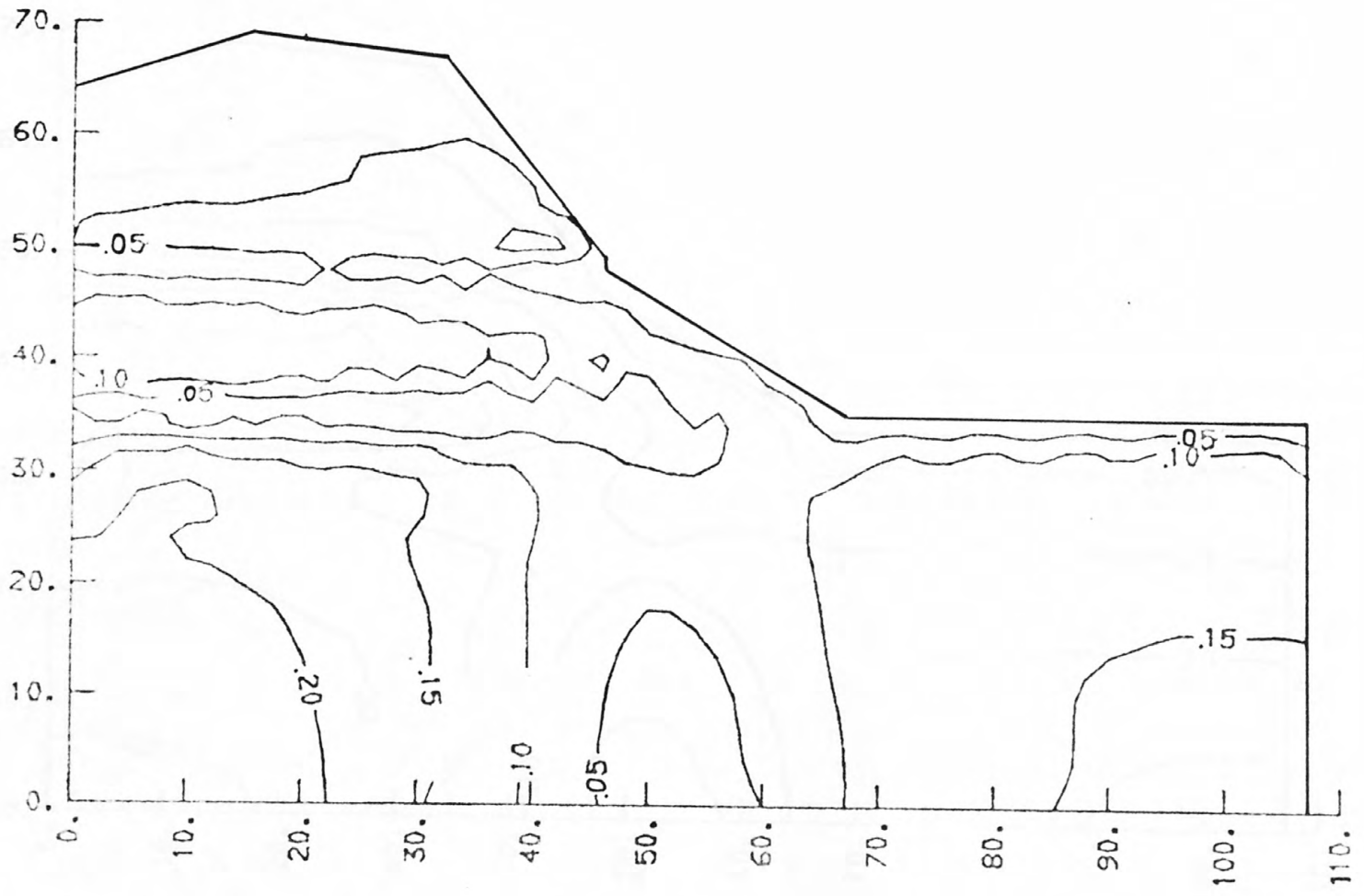

Figure 39. Contours of $\sqrt{J_2}$, elastic analysis. Contour values are in MPa.

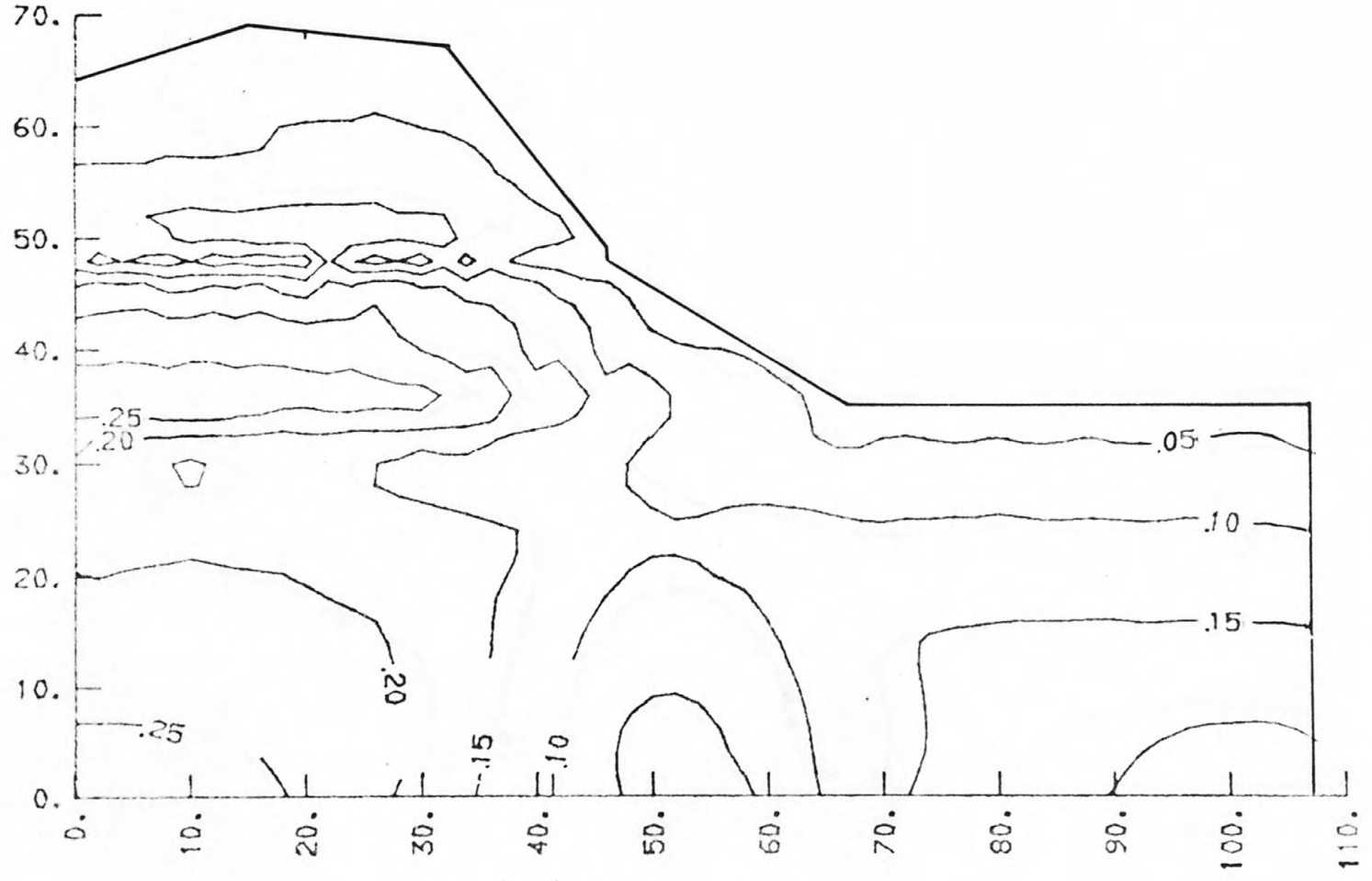

Figure 40. Contour values of $\sqrt{J_2}$, elastic-plastic analysis, peak strengths. Contour values are in MPa.

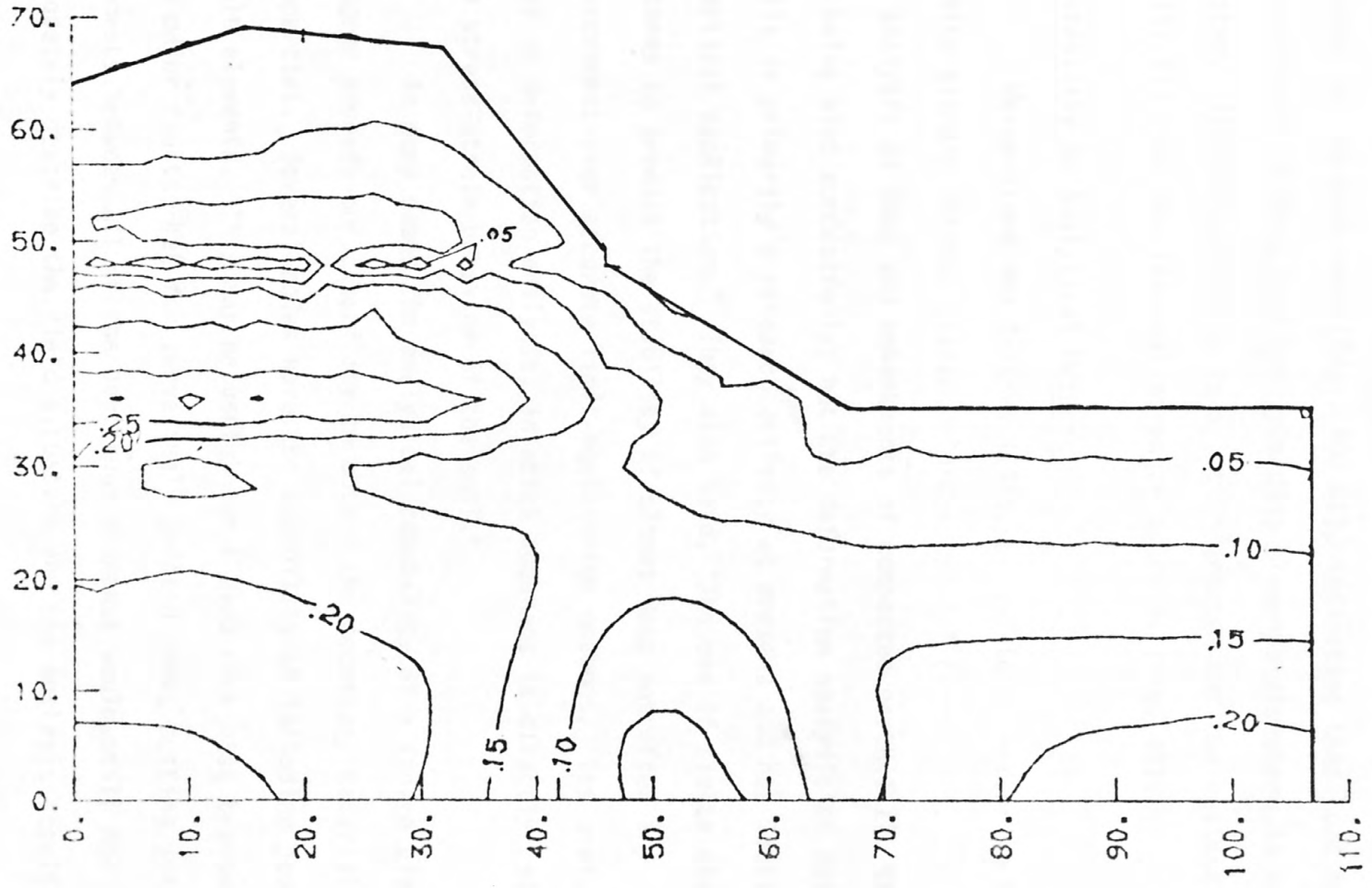

Figure 41. Contours of $\sqrt{J_2}$, elastic-plastic analysis, residual strengths. Contour values are in MPa.

of tensile major principal stresses in the two layers (Fig. 26). For the elastic-plastic analyses the contours of $\sqrt{J_2}$ show a concentration of stress in the coal seam (Figs. 40, 41), indicating that load is transferred to this zone from yielding elements elsewhere in the system. The concentration is a little greater for the residual strength (fig. 41) than for the peak strength analysis (Fig. 40).

Suitability of Analytical Methods

Morgenstern and Sangrey (1978, p. 168-169), referring to the finite element method, stated: "Under special conditions, particularly in analysis of dams and embankments of compacted earth fill, the method is being used successfully; but the deformation analysis of natural soils is primarily a research activity at present and has little practical application." They also said, "The use of finite element methods to predict the stability of slopes does not offer any improvement over accurate limit-equilibrium methods. Its usefulness lies in deformation analysis, in which accuracy is directly related to the stress-strain behavior of the soil."

In many cases the analytical capability of a finite element program exceeds our capability to obtain the necessary material properties. Several codes have the capability of including joint or fault elements. This may be useful for a hard rock mass transected by a few major faults; but for pervasively jointed rock, putting joint elements between all of the continuum elements would still not adequately describe the field situation and the analysis itself would be

totally impractical if not impossible. What is needed is a practical method of determining the effective rock mass properties for use in a continuum analysis. Another drawback of nonlinear finite element codes is that the methods used to arrive at a convergent solution generally do not follow the actual stress-strain path undergone by the material in the field.

Limit equilibrium methods have the advantage of speed and simplicity. A large number of feasible failure surfaces can be analyzed to determine which is the most critical. Finite element analysis might be used in conjunction with limit equilibrium to provide more detailed information if necessary.

TIME-DEPENDENT BEHAVIOR

The problem of time-dependent behavior has long plagued soil and rock engineers; however, the present state of knowledge of time-dependent material properties remains poor. Some problems caused by time-dependent rock behavior include long-term settlement of buildings, deterioration of natural and excavated slopes, creep closure of mines and tunnels, and continuing rebound of foundations in overconsolidated materials.

The phenomenon of rebound has caused engineering problems at several areas, notably at damsites on the upper Missouri River at Fort Peck Dam, Montana; Garrison Dam, North Dakota; and Oahe Dam, South Dakota. At the Garrison damsite saw cuts 7.6 cm wide and 2.1 m deep in the powerhouse area closed in 24 hours (Smith and Redlinger, 1953, p. 65); and as much as 0.9 m of rebound was measured in the deepest excavation at this site (Underwood, 1967, p. 109). Smith and Redlinger (1953) inferred that the magnitude of rebound is dependent on the rate of unloading. The deformations have an initial abrupt phase followed by long-term relaxation (Underwood, Thorfinson, and Black, 1964). Magnitudes and rates of rebound are complicated; they are controlled by time, geologic history, material properties, and excavation methods.

Wawersik (1973, p.85) cited four major reasons why time effects generally are not considered in engineering design:

1. Time-dependent deformations measured in the laboratory are generally small.

2. It is difficult to tell time-dependent deformations from those due to external changes.
3. Available descriptions of time-dependent rock properties are fragmentary and inadequate for design calculations.
4. Field monitoring programs and laboratory experiments necessary to furnish adequate descriptions are complex, time-consuming, and expensive.

Previous Work

At the First International Conference on Soil Mechanics and Foundation Engineering, Terzaghi (1936) proposed a mechanism for time-dependent decrease in soil strength due to increasing water content along cracks and fissures.

Skempton (1964), in the Fourth Rankine Lecture, analyzed several slopes in London Clay that failed between 19 and 49 years after excavation. He introduced a parameter called the "residual factor", defined as

$$R = \frac{s_p - s}{s_p - s_r}, \qquad (17)$$

where s is the actual shear stress at failure and s_p and s_r are the peak and residual shear strengths, respectively. Thus R is the fraction of the total slip surface along which the soil strength has fallen to its residual value.

Bjerrum (1967), in the Third Terzaghi Lecture, proposed a strain-energy hypothesis to explain time-dependent failure of slopes in overconsolidated clays and clay shales. According to this hypothesis,

the ability of a clay or clay shale to store strain energy during consolidation is enhanced by the development of diagenetic bonds between the clay particles. This stored strain energy is released as the diagenetic bonds are broken down by weathering processes. This release of energy results in deformation (expansion) of the material mass accompanied by an increase in stress. When the shear stress exceeds the peak shear strength at some point within the mass, a failure surface is initiated. This failure surface is propagated as the weathering process continues and as stresses build up in areas adjacent to the failed zone.

Matheson (1972), in his study of valley rebound in the northern Great Plains of the United States and the southern Prairie Provinces of Canada, identified two components of rebound:

1. initial elastic rebound due to decreased loads and elimination of horizontal constraints, and
2. time-dependent rebound due to absorption of water by swelling clays.

The primary conclusions of these workers seem to be that time-dependent behavior or creep is caused by weathering and absorption of water by swelling clays, and that for failure to be initiated the stress must exceed the peak strength at some point within the mass.

In a more recent paper Nelson and Thompson (1977) presented a theory wherein creep failure was due to a gradual breaking of the diagenetic bonds when the shear stresses are greater than the residual shear strength. According to their theory, the stresses do not have to exceed the original peak strength at any point in order for failure to occur, and weathering, while it would accelerate the process, is not

essential to time-dependent deformation and failure. This concept and the concept of Skempton's residual factor are illustrated in Figure 42.

Extension of the Nelson-Thompson Hypothesis

The Nelson-Thompson hypothesis can easily be extended to the three-dimensional Drucker-Prager yield criterion if one visualizes two coaxial yield surface cones (Fig. 43). If the residual cohesion is assumed to be zero, the residual strength yield surface will have its vertex at the origin of stresses.

Skempton's residual factor may now be redefined for the Drucker-Prager criterion, in a manner analogous to that for defining the safety factor, as

$$R = \frac{r_p - r}{r_p - r_r}, \tag{18}$$

where the r's represent radii from the axis of the cones (the hydrostatic line) and the subscripts p and r refer to peak and residual values, respectively (Fig. 43). Expressing the residual factor in terms of the peak and residual Drucker-Prager constants α and k and the stress invariants I_1 and J_2, we have the relationship

$$R = \frac{k_p - \alpha_p I_1 - \sqrt{J_2}}{k_p - k_r + I_1 (\alpha_r - \alpha_p)}. \tag{19}$$

Using these definitions of the residual factor (equations 17, 18, and 19) one is in practicality limited to analysis of uniform slopes. We may also express the residual factor in terms of the factors of safety with respect to peak and residual strengths by the relationship

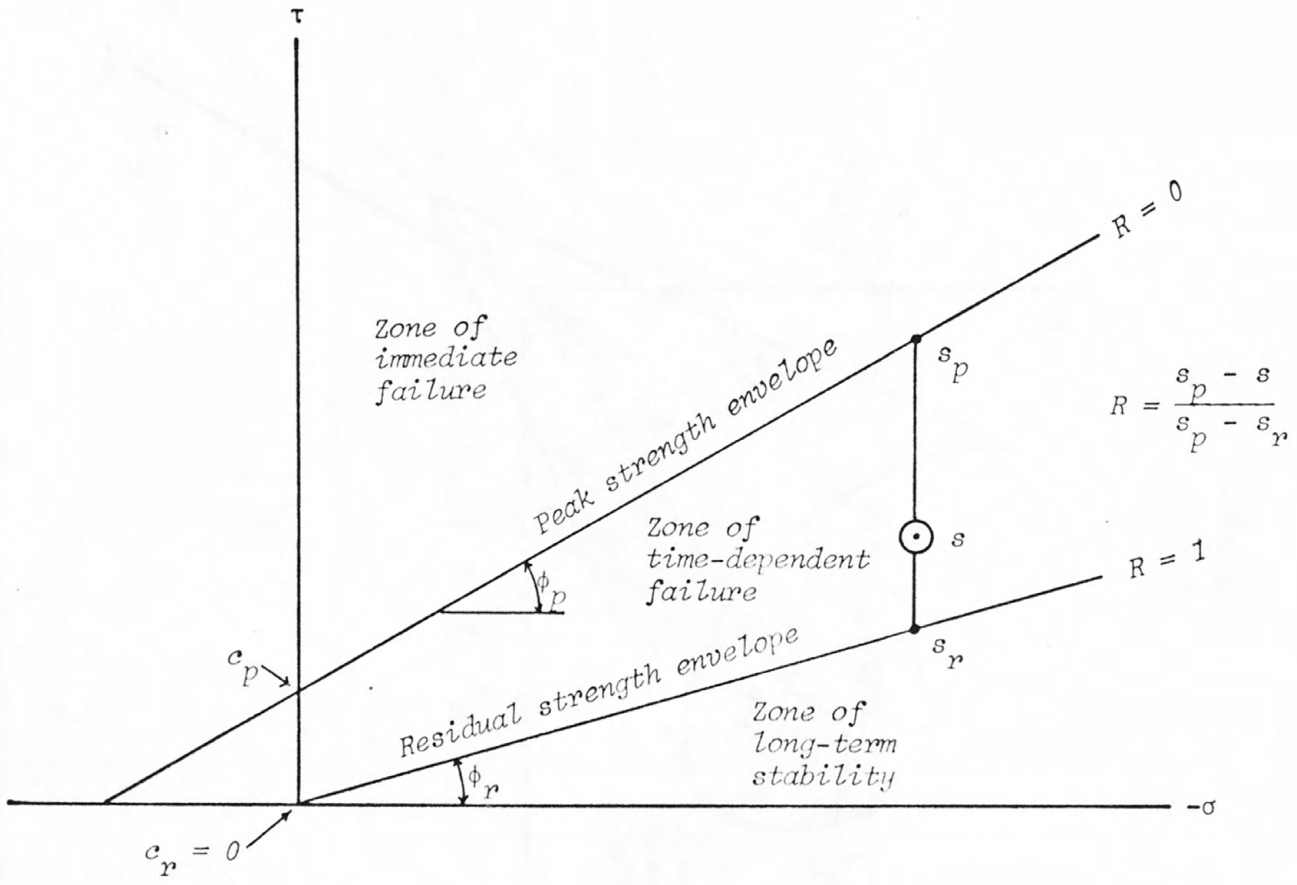

Figure 42. Idealized Mohr diagram illustrating the Nelson-Thompson hypothesis and Skempton's residual factor (R).

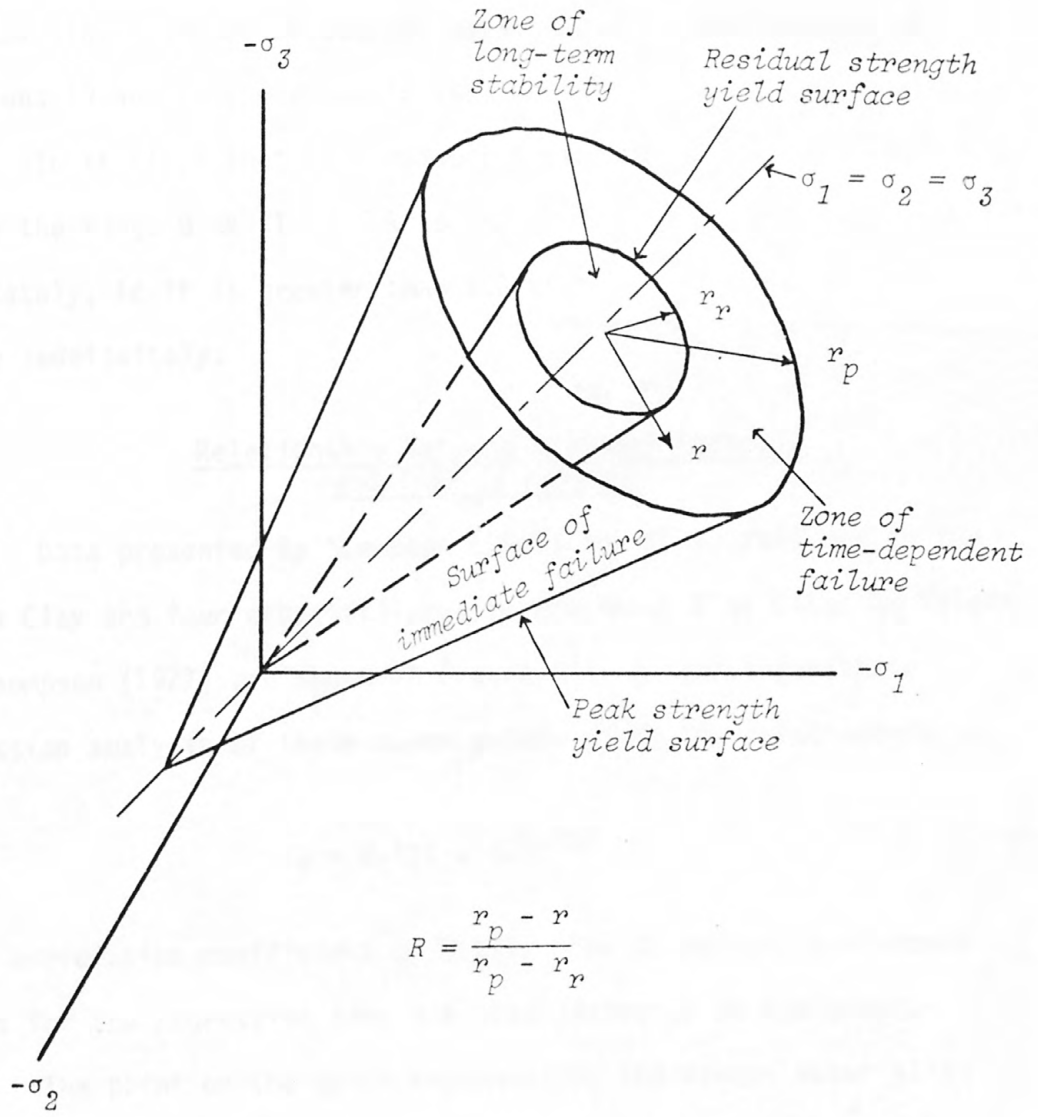

Figure 43. Nelson-Thompson hypothesis and Skempton's residual factor using the Drucker-Prager yield criterion.

$$R = \frac{F_p - 1}{F_p - F_r} . \qquad (20)$$

Equation 20 can be used with either finite element or limit equilibrium analyses to estimate the average residual factor of an existing or proposed slope made up of several materials. The derivations of equations 19 and 20 are shown in the Appendix.

It is clear that the residual factor has meaning only if it is within the range $0 < R < 1$. If R is negative ($F_p < 1$), the slope will fail immediately; if it is greater than 1.0 ($F_r > 1$), the slope should be stable indefinitely.

Relationship Between Residual Factor and Time to Failure

Data presented by Skempton (1964) for three failures in the London Clay and four other failures in the Amuay Clay cited by Nelson and Thompson (1977) are shown in Figure 44. A semi-logarithmic regression analysis of these seven points gives the relationship

$$t_f = 0.424 \times 10^{2.76R} \qquad (21)$$

and a correlation coefficient of 0.981. The 90-percent confidence limits for the regression line are also indicated on the graph.

The point on the graph representing the Hidden Water slide ($R = 0.641$, $t_f = 20$ yr) is seen to fall within the 90-percent band computed from the other seven points. This point was determined from Spencer analyses using peak and residual strengths, each with the water table at the valley floor and assuming zero cohesion. If the point

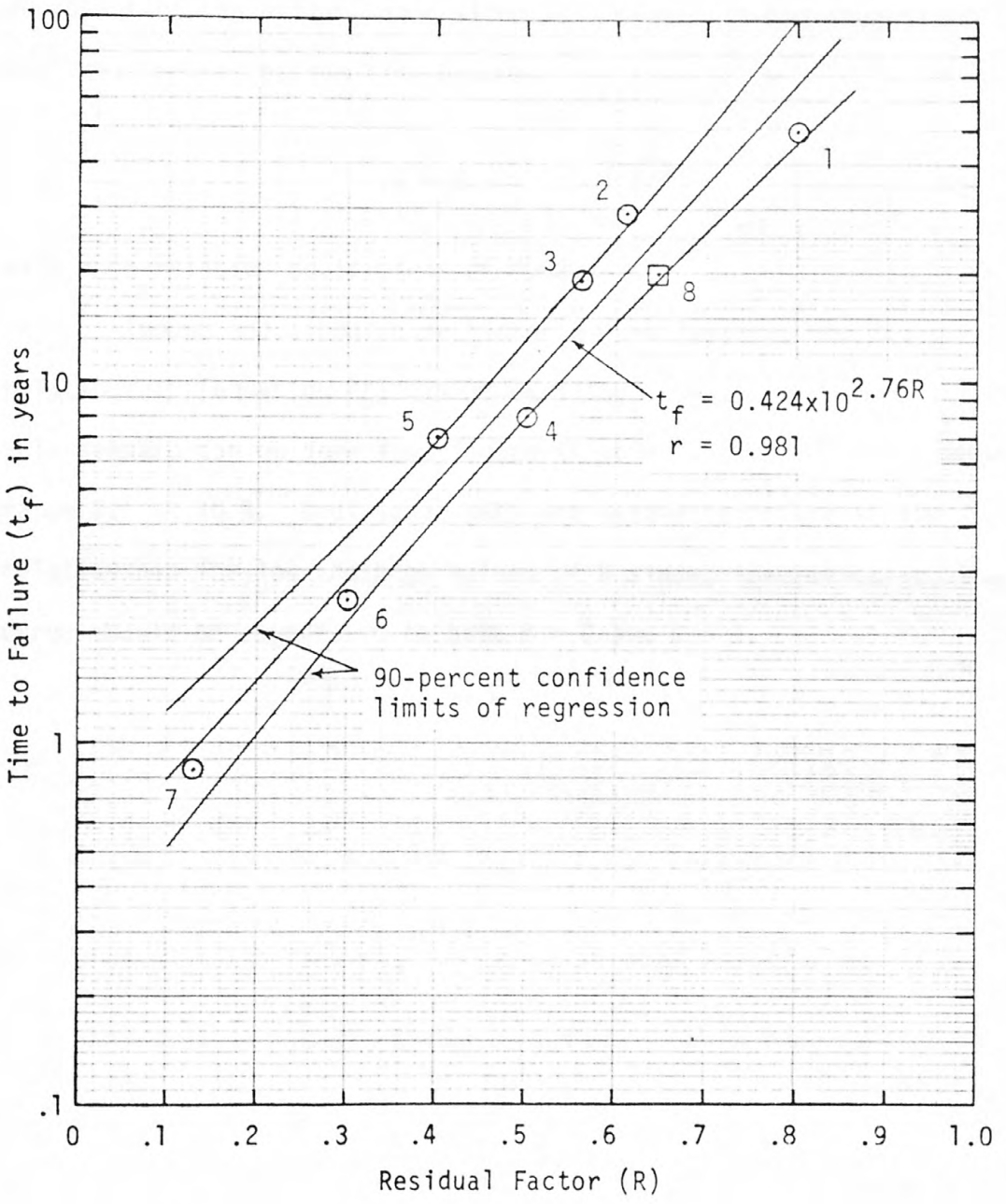

Figure 44. Relationship between residual factor and time to failure for excavations in overconsolidated clays.

1. Northolt
2. Kensal Green } London Clay (Skempton, 1964)
3. Sudbury Hill
4-7. Amuay Clay (cited by Nelson and Thompson, 1977)
8. Hidden Water mine slide, Sheridan Co., Wyoming

representing the Hidden Water slide is included in the regression analysis the regression line becomes

$$t_f = 0.435 \times 10^{2.71R} \qquad (22)$$

with a correlation coefficient of 0.980.

Though additional case histories are lacking, the above relationship (equation 22) can be used for a predictive model. This relationship can be seen from figure 44 to hold for the approximate range $0.1 < R < 0.8$. Additional data are needed to determine the relationship for low and high values of R since, theoretically, the curve should be asymptotic to both $R = 0$ and $R = 1$.

CONCLUSIONS AND RECOMMENDATIONS FOR FURTHER RESEARCH

The landslide at the Hidden Water mine is an instructive example of long-term slope behavior in the Powder River Basin. Although this area was not reclaimed, and the practice of leaving a spoil pile on top of the highwall would not be permitted under current laws and regulations, this study is still applicable to current mining practices. The spoil pile in this case merely provides additional load on the highwall; the same total land would be produced with a higher highwall, as is the current practice.

Time to failure seems to be predictable in these materials using the residual factor and the Nelson-Thompson hypothesis with the regression equation (22). More case histories are needed to refine this equation, especially for short-term failures (less than 1 year), which could aid in the design of working slopes in active mines. The residual factor can be computed from the safety factors with respect to peak and residual strengths using equation (2). The factors of safety used to determine the residual factor can theoretically be from either limit equilibrium or finite element analyses. However, at the present time the Spencer limit equilibrium method seems to give safety factors more in agreement with the observed field conditions than does the finite element method. The finite element analysis can still be useful in a semi-quantitative way if the trajectories of expected shear failure are

used to extrapolate known or inferred positions of the failure surface, and if stress contour diagrams are to identify zones of stress buildup.

An implication of the Nelson-Thompson hypothesis is that to insure long-term stability, slopes must be designed on the basis of their residual strength.

An important topic that needs additional research before long-term slope behavior can be fully understood is the physics and mechanics of bonding in clays and shales. I am hopeful that research in this area will result in a useable rheological model that incorporates the decrease of strength with time.

A question regarding the use of the Drucker-Prager yield criterion concerns the determination of the material constants α and k. As stated earlier, the formulas used to determine α and k from ϕ and c depend on the type of test used to determine ϕ and c. Corp (1974) gave formulas for use with triaxial compression, triaxial extension, and plane strain tests; and compared the values of α and k thus obtained from assumed values of ϕ and c. The values of ϕ and c, however, will themselves vary with the type of test. Thus, the question is: if samples of the same material are subjected to various types of tests to determine the parameters ϕ and c, and the values thus obtained are used in the formulas for the respective test, do they result in the same or nearly the same values for the material "constants" α and k? If not, then there is a serious question as to the validity of using ϕ and c from a triaxial test to determine α and k, and then of using those values in a plane-strain analysis. Also, is it possible to determine α and k from tests other than those mentioned above?

A useful contribution to the mining industry, and to those charged with regulating mining operations, would be a comprehensive study of the geotechnical properties of major energy-bearing (coal, uranium, and oil shale) units throughout the northern Great Plains and Rocky Mountain regions. Such a study should include properties of the in-situ rock masses and of the reworked spoil materials resulting from mining of these units. Other studies should be made of the stress changes and deformations in the area of a proposed mine from before the start of mining until after reclamation; such studies should include the long-term, post-reclamation behavior of the site.

Finally, a well-documented finite element code should be developed especially for slope design. Ideally, this program should incorporate several material models (elastic, elastic-plastic, brittle), be able to simulate the effects of pre-mining geologic history and mining excavation, and be able to include the effects of a groundwater system described as part of the input data. Especially desirable, if a time-dependent rheology can be developed, would be a code capable of simulating the behavior of the slope over a period of time.

APPENDIX

Derivation of the Factor of Safety for the Drucker-Prager Yield Criterion

This derivation basically follows that of Corp (1974), Corp, Schuster, and McDonald (1975) but is somewhat more detailed. The axis of the yield surface cone is the hydrostatic line $\sigma_1 = \sigma_2 = \sigma_3$ in principal stress space. It is convenient to have this axis coincide with one of the principal axes of the coordinate system, so we shall define a new coordinate system x, y, z as shown in Figure 45 and perform the necessary transformations to express the coordinates in the new system in terms of the principal stresses.

First consider a rotation of 45° clockwise about the $-\sigma_3$ axis (Fig. 45). The transformation equation is

$$\sigma_j' = c_{ij}\, \sigma_i \,, \tag{23}$$

where c_{ij} is the cosine of the angle between the positive σ_i and σ_j' directions:

$$c_{ij} = \begin{bmatrix} \frac{1}{\sqrt{2}} & \frac{-1}{\sqrt{2}} & 0 \\ \frac{1}{\sqrt{2}} & \frac{1}{\sqrt{2}} & 0 \\ 0 & 0 & 1 \end{bmatrix}. \tag{24}$$

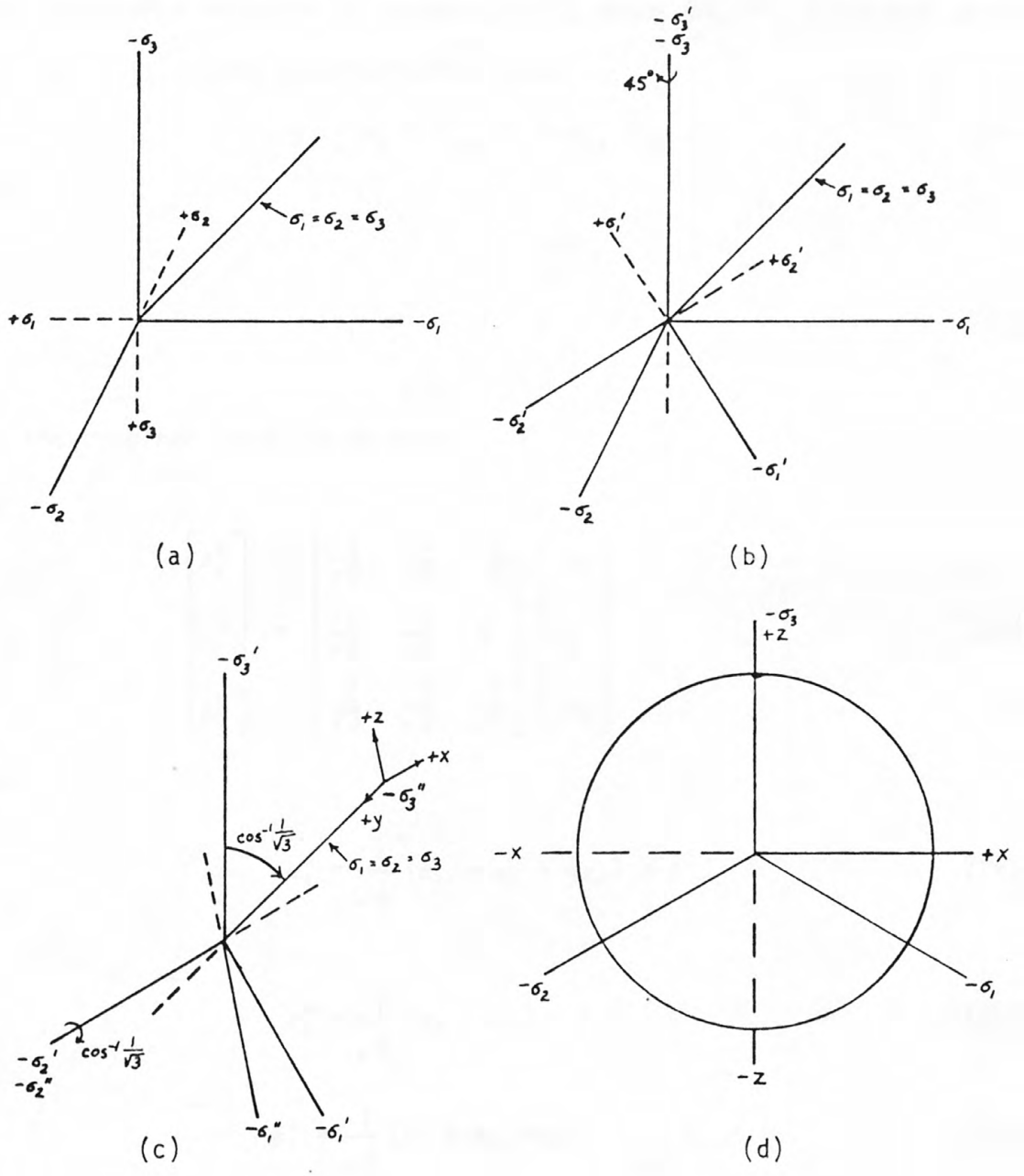

Figure 45. Transformation of axes for derivation of safety factor using Drucker-Prager criterion.

(a) Initial coordinate system showing hydrostatic line
(b) First rotation
(c) Second rotation and new coordinate system
(d) Looking down the -y axis toward the origin, showing relationships of the two coordinate systems.

Next consider a rotation of arccos $(1/\sqrt{3})$, about 54.74°, clockwise about the $-\sigma_2'$ axis. This transformation gives

$$\sigma_\ell'' = c'_{k\ell}\ \sigma_k' = c'_{k\ell}\ c_{ik}\ \sigma_i \tag{25}$$

with

$$c'_{k\ell} = \begin{bmatrix} \frac{1}{\sqrt{3}} & 0 & \frac{2}{\sqrt{6}} \\ 0 & 1 & 0 \\ \frac{-2}{\sqrt{6}} & 0 & \frac{1}{\sqrt{3}} \end{bmatrix}. \tag{26}$$

For the combined rotation we have

$$\begin{bmatrix} \sigma_1'' \\ \sigma_2'' \\ \sigma_3'' \end{bmatrix} = \begin{bmatrix} \frac{1}{\sqrt{6}} & \frac{1}{\sqrt{6}} & \frac{-2}{\sqrt{6}} \\ \frac{-1}{\sqrt{2}} & \frac{1}{\sqrt{2}} & 0 \\ \frac{1}{\sqrt{3}} & \frac{1}{\sqrt{3}} & \frac{1}{\sqrt{3}} \end{bmatrix} \begin{bmatrix} \sigma_1 \\ \sigma_2 \\ \sigma_3 \end{bmatrix} \tag{27}$$

and

$$\sigma_1'' = \frac{1}{\sqrt{6}} (\sigma_1 + \sigma_2 - 2\sigma_3) = z\ , \tag{28}$$

$$\sigma_2'' = \frac{1}{\sqrt{2}} (\sigma_2 - \sigma_1) = x\ , \tag{29}$$

$$\sigma_3'' = \frac{1}{\sqrt{3}} (\sigma_1 + \sigma_2 + \sigma_3) = \frac{1}{\sqrt{3}} I_1 = y\ . \tag{30}$$

In the Drucker-Prager yield criterion

$$\alpha I_1 + \sqrt{J_2} = k \ , \tag{8}$$

$$I_1 = \sigma_1 + \sigma_2 + \sigma_3 = \sqrt{3}\, y \ , \tag{31}$$

and

$$J_2 = \frac{1}{3} (\sigma_1^2 + \sigma_2^2 + \sigma_3^2 - \sigma_1\sigma_2 - \sigma_2\sigma_3 - \sigma_1\sigma_3) \ . \tag{10}$$

Now

$$x^2 = \left[\frac{1}{\sqrt{2}} (\sigma_2 - \sigma_1)\right]^2 = \frac{1}{2} (\sigma_2 - \sigma_1)^2$$

$$= \frac{1}{2} (\sigma_2^2 - 2\sigma_1\sigma_2 + \sigma_1^2) = \frac{\sigma_2^2}{2} + \frac{\sigma_1^2}{2} - \sigma_1\sigma_2 \ , \tag{32}$$

$$z^2 = \left[\frac{1}{\sqrt{6}} (\sigma_1+\sigma_2-2\sigma_3)\right]^2 = \frac{1}{6} (\sigma_1^2+\sigma_2^2+4\sigma_3^2+2\sigma_1\sigma_2-4\sigma_1\sigma_3-4\sigma_2\sigma_3)$$

$$= \frac{\sigma_1^2}{6} + \frac{\sigma_2^2}{6} + \frac{2\sigma_3^2}{3} + \frac{\sigma_1\sigma_2}{3} - \frac{2\sigma_1\sigma_3}{3} - \frac{2\sigma_2\sigma_3}{3} \ , \tag{33}$$

and

$$x^2 + z^2 = \frac{\sigma_1^2}{2} + \frac{\sigma_1^2}{6} + \frac{\sigma_2^2}{2} + \frac{\sigma_2^2}{6} + \frac{2\sigma_3^2}{3} - \sigma_1\sigma_2 + \frac{\sigma_1\sigma_2}{3} - \frac{2\sigma_1\sigma_3}{3} - \frac{2\sigma_2\sigma_3}{3}$$

$$= \frac{2}{3} (\sigma_1^2+\sigma_2^2+\sigma_3^2-\sigma_1\sigma_2-\sigma_1\sigma_3-\sigma_2\sigma_3) = 2J_2 \quad \text{(from (10))} \ . \tag{34}$$

Thus

$$x^2 + z^2 = 2J_2 = r^2 \ , \tag{35}$$

and

$$\sqrt{2J_2} = r \ . \tag{36}$$

For the yield condition

$$\alpha I_1 + \sqrt{J_2} = k \tag{8}$$

$$\sqrt{J_2} = k - \alpha I_1$$

$$J_2 = (k - \alpha I_1)^2$$

$$2J_2 = 2\,(k - \alpha I_1)^2 = x^2 + z^2 = r_f^2$$

Thus

$$r_f = \sqrt{2}\,(k - \alpha I_1) \tag{37}$$

$$2J_2 = 2(k-\alpha I_1)^2 = x^2 + z^2 = r_f^2$$

and the factor of safety is

$$F = \frac{r_f}{r} = \frac{\sqrt{2}\,(k - \alpha I_1)}{\sqrt{2J_2}} = \frac{k - \alpha I_1}{\sqrt{J_2}}\,. \tag{15}$$

Derivation of the Residual Factor for the Drucker-Prager Yield Criterion

From the definition given by equation (18)

$$R = \frac{r_p - r}{r_p - r_r} .$$

For the peak and residual yield surfaces the radii are

$$r_p = \sqrt{2}\,(k_p - \alpha_p I_1) , \tag{38}$$

$$r_r = \sqrt{2}\,(k_r - \alpha_r I_1) , \tag{39}$$

and for the actual stress state

$$r = \sqrt{2J_2} . \tag{36}$$

Substituting,

$$R = \frac{\sqrt{2}\,(k_p - \alpha_p I_1) - \sqrt{2J_2}}{\sqrt{2}\,(k_p - \alpha_p I_1) - \sqrt{2}\,(k_r - \alpha_r I_1)}$$

$$= \frac{(k_p - \alpha_p I_1) - \sqrt{J_2}}{(k_p - \alpha_p I_1) - (k_r - \alpha_r I_1)}$$

$$= \frac{k_p - \alpha_p I_1 - \sqrt{J_2}}{k_p - k_r + I_1\,(\alpha_r - \alpha_p)} . \tag{19}$$

Derivation of the Residual Factor in Terms of the Factors of Safety

Let s_p and s_r represent the peak and residual shear strengths, respectively, and let s represent the actual shear stress, all for a given normal stress using a Mohr-Coulomb criterion. The factor of safety with respect to peak strength is

$$F_p = \frac{s_p}{s} \tag{37}$$

and with respect to residual strength

$$F_r = \frac{s_r}{s} \tag{38}$$

or
$$s_p = sF_p \tag{39}$$

and
$$s_r = sF_r \ . \tag{40}$$

By Skempton's definition the residual factor is

$$R = \frac{s_p - s}{s_p - s_r} \tag{17}$$

$$= \frac{sF_p - s}{sF_p - sF_r}$$

$$R = \frac{F_p - 1}{F_p - F_r} \ . \tag{20}$$

This relationship can also be derived in a similar manner for the Drucker-Prager criterion using radii from the hydrostatic line.

REFERENCES

Baligh, M. M., 1973, Numerical study of uniaxial and triaxial rock compression tests: La Jolla, California, Systems, Science, and Software, Inc., 159 p. (Available through NTIS, SSS-R-73-1658.)

Beikman, H. M., 1962, Geology of the Powder River Basin, Wyoming and Montana, with reference to subsurface disposal of radioactive waste: U.S. Geological Survey Trace Elements Investigations Report 823, 85 p.

Bjerrum, Laurits, 1967, Progressive failure in slopes of overconsolidated clay and clay-shales [Third Terzaghi Lecture]: American Society of Civil Engineers, Journal of Soil Mechanics and Foundations Division, v. 93, no. SM5, paper 5456, p. 1-49.

Chowdhury, R. N., 1978, Slope analysis: Amsterdam, Elsevier (Developments in Geotechnical Engineering, v. 22), 423 p.

Coates, D. F., 1967, Rock mechanics principles: Canada Department of Energy, Mines, and Resources, Mines Branch Monograph 874 (rev. 1967), 363 p.

Corp, E. L., 1974, A finite-element model for stability analysis of mine-waste embankments subjected to seepage: Moscow, University of Idaho, Ph. D. thesis, 203 p.

Corp, E. L., Schuster, R. L., and McDonald, M. M., 1975, Elastic-plastic stability analysis of mine-waste embankments: U.S. Bureau of Mines Report of Investigations 8069, 98 p.

Desai, C. S., and Abel, J. F., Jr., 1972, Introduction to the finite-element method: New York, Van Nostrand Reinhold, 477 p.

Drucker, D. C., and Prager, W., 1952, Soil mechanics and plastic analysis or limit design: Quarterly of Applied Mathematics, v. 10, no. 2, p. 157-165.

Ebaugh, W. F., 1977, Landslide factor mapping and slope stability analysis of the Big Horn quadrangle, Sheridan County, Wyoming: Boulder, University of Colorado Ph. D. thesis, 194 p.

Egeberg, J. L., 1969, MESHGEN--A computer code for automatic finite-element mesh generation: Livermore, California, Sandia Laboratories, 41 p.; available through NTIS, SCL-DR-69-49.

Fahy, M. P., and Smith, W. K., 1976, Geotechnical properties of some upper Fort Union rocks from the Decker area, Big Horn County, Montana: U.S. Geological Survey Open-File Report 76-596, 110 p.

Fenneman, N. M., 1931, Physiography of Western United States: New York, McGraw-Hill, 534 p.

Jaeger, J. C., and Cook, N. G. W., 1969, Fundamentals of rock mechanics: London, Methuen, 513 p.

Keefer, W. R., 1974, Regional topography, physiography, and geology of the northern Great Plains: U.S. Geological Survey Open-File Report 74-50, 17 p., 4 pl.

Lambe, T. W., and Whitman, R. V., 1969, Soil mechanics: New York, John Wiley, 553 p.

Lee, F. T., Smith, W. K., and Savage, W. Z., 1976, Stability of highwalls in surface coal mines, western Powder River Basin, Wyoming and Montana: U.S. Geological Survey Open-File Report 76-846, 52 p.

Matheson, D. S., 1972, Geotechnical implications of valley rebound: Edmonton, University of Alberta, Ph. D. thesis, 550 p.

McKenna, M. C., and Love, J. D., 1972, High-level strata containing early Miocene mammals on the Bighorn Mountains, Wyoming: American Museum Novitates, no. 2490, 30 p.

Morgenstern, N. R., and Price, V. E., 1965, The analysis of the stability of general slip surfaces: Geotechnique, v. 15, no. 1, p. 79-93.

_____1967, A numerical method for solving the equations of stability of general slip surfaces: Computer Journal, v. 9, no. 4, p. 388-393.

Morgenstern, N. R., and Sangrey, D. A., 1978, Methods of stability analysis, in Schuster, R. L., and Krizek, R. J., eds., Landslides--Analysis and control: National Academy of Sciences, Transportation Research Board Special Report 176, p. 155-171.

Nelson, J. D., and Thompson, E. G., 1977, A theory of creep failure in overconsolidated clay: American Society of Civil Engineers, Journal of Geotechnical Engineering Division, v. 103, no. GT 11, paper 13342, p. 1281-1294.

Rocky Mountain Association of Geologists, 1972, Geologic atlas of the Rocky Mountain region: Denver, Rocky Mountain Association of Geologists, 331 p.

Singh, R., Henkel, D. J., and Sangrey, D. A., 1973, Shear and K_o swelling of overconsolidated clay: International Conference on Soil Mechanics and Foundation Engineering, 8th, Moscow, 1973, Proceedings, v. 1, p. 367-376.

Skempton, A. W., 1964, Long-term stability of clay slopes [4th Rankine Lecture]: Geotechnique, v. 14, no. 2, p. 77-101.

Smith, C. K., and Redlinger, J. F., 1953, Soil properties of Fort Union clay shale [North Dakota]: International Conference on Soil Mechanics and Foundation Engineering, 3d, Switzerland, Proceedings, v. 1, p. 62-66.

Spencer, E., 1967, A method of analysis of embankments assuming parallel inter-slice forces: Geotechnique, v. 17, no. 1, p. 11-26.

Taylor, D. W., 1948, Fundamentals of soil mechanics: New York, John Wiley, 700 p.

Terzaghi, Karl, 1936, Stability of slopes in natural clay: International Conference on Soil Mechanics and Foundation Engineering, 1st, Cambridge, Massachusetts, Proceddings, v. 1, p. 161-165.

Terzaghi, Karl, and Peck, R. B., 1967, Soil mechanics in engineering practice [2d ed.]: New York, John Wiley, 729 p.

Underwood, L. B., 1967, Classification and identification of shales: American Society of Civil Engineers, Journal of Soil Mechanics and Foundations Division, v. 93, no. SM6, paper 5560, p. 97-116.

Underwood, L. B., Thorfinson, S. T., and Black, W. T., 1964, Rebound in redesign of Oahe Dam hydraulic structures: American Society of Civil Engineers, Journal of Soil Mechanics and Foundations Division, v. 90, no. SM2, paper 3830, p. 65-86.

U.S. Geological Survey and Montana Department of State Lands, 1977, Final environmental impact statement, proposed plan of mining and reclamation, East Decker and North Extension mines, Decker Coal Company, Big Horn County, Montana: U.S. Geological Survey, 2 v., 1517 p.

Varnes, D. J., 1962, Analysis of plastic deformation according to Von Mises' theory, with application to the South Silverton area, San Juan County, Colorado: U.S. Geological Survey Professional Paper 378-B, 49 p.

Wawersik, W. R., 1973, Time dependent rock behavior in uniaxial compression, in Hardy, H. R., Jr., and Stefanko, Robert, eds., New horizons in rock mechanics, 14th symposium on rock mechanics: New York, American Society of Civil Engineers, p. 85-106.

Wright, S. G., 1969, A study of slope stability and the undrained shear strength of clay shales: Berkeley, University of California, Ph. D. dissertation, 687 p.

Zienkiewicz, O. C., 1971, The finite element method in engineering science: London, McGraw-Hill, 521 p.

USGS LIBRARY-RESTON
3 1818 00074267 4